https://lib.uliege.be https://matheo.uliege.be

Calibration and validation of a full-scale experimental model for the study of drowning victims

Auteur : Degrève, Camille
Promoteur(s) : Dewals, Benjamin
Faculté : Faculté des Sciences appliquées
Diplôme : Master en ingénieur civil des mines et géologue, à finalité spécialisée en géologie de l'ingénieur et de l'environnement
Année académique : 2021-2022
URI/URL : http://hdl.handle.net/2268.2/16357

Avertissement à l'attention des usagers :

Tous les documents placés en accès ouvert sur le site le site MatheO sont protégés par le droit d'auteur. Conformément aux principes énoncés par la "Budapest Open Access Initiative"(BOAI, 2002), l'utilisateur du site peut lire, télécharger, copier, transmettre, imprimer, chercher ou faire un lien vers le texte intégral de ces documents, les disséquer pour les indexer, s'en servir de données pour un logiciel, ou s'en servir à toute autre fin légale (ou prévue par la réglementation relative au droit d'auteur). Toute utilisation du document à des fins commerciales est strictement interdite.

Par ailleurs, l'utilisateur s'engage à respecter les droits moraux de l'auteur, principalement le droit à l'intégrité de l'oeuvre et le droit de paternité et ce dans toute utilisation que l'utilisateur entreprend. Ainsi, à titre d'exemple, lorsqu'il reproduira un document par extrait ou dans son intégralité, l'utilisateur citera de manière complète les sources telles que mentionnées ci-dessus. Toute utilisation non explicitement autorisée ci-avant (telle que par exemple, la modification du document ou son résumé) nécessite l'autorisation préalable et expresse des auteurs ou de leurs ayants droit.

University of Liege – Faculty of applied sciences

Calibration and validation of a full-scale experimental model for the study of drowning victims

ATFE0011-1 Master Thesis

Advisor
B. Dewals (ULiege)

Jury
S. Erpicum (ULiege)
T. Andrianne (ULiège)
N. Riviere (INSA, Lyon)

Dissertation submitted as part requirement for the degree of Master in Civil Engineer of Mines and Geologist, by DEGREVE Camille

ACADEMIC YEAR 2021 - 2022

Remerciements

Je voudrais remercier toutes les personnes qui ont contribué au bon déroulement de ce travail de fin d'étude :

Et tout particulièrement Clément Delhez qui a su se montrer extrêmement disponible et ce tout au long du quadrimestre, qui a su me conseiller et m'aiguiller, répondre à mes nombreuses questions, m'aider à comprendre certains concepts et qui a pris le temps de relire mon travail et de m'aider à le mettre en valeur.

M. Dewals, mon promoteur académique, de m'avoir permis de réaliser ce travail de fin d'étude sur un thème qui s'éloigne un peu de ce que je connais ou de ce que j'ai appris lors de mon cursus mais qui était extrêmement intéressant et enrichissant.

Gregory Thonard et Maxime Mathieu, pour leur accueil chaleureux lors de mes quelques passages au Laboratoire d'Hydraulique.

M. Hallot sans qui les acquisitions laser et photogrammétriques n'auraient pas pu être réalisés et qui m'a aiguillé sur le choix des logiciels de modélisation 3D ainsi que Pierre Jouan qui a su me donner de bons conseils dans leurs utilisations.

Toute l'équipe du Laboratoire de Soufflerie (Thomas Andrianne, Antoine, Mathieu et Raphael) que ce soit pour la mise en place des essais sur Ken ou juste pour leurs disponibilités et leurs aides.

Finalement, je remercie tous mes proches de m'avoir supporté que ce soit sur la durée de réalisation de ce travail mais aussi sur la durée de mes études.

Abstract:

There is currently no accurate and comprehensive model for the search of drowning victims in urban areas. Therefore, this thesis aims to contribute to the creation of such a model, by focusing on the calibration and validation of a wind tunnel experimental setup performed on a full-scale model.

To achieve this, existing search for drowning persons models and their equations are analysed, fluid dynamics models applied to the human body are also reviewed, as well as papers on the position of a drowning person's body. This led to the identification of two essential parameters for such a model, which are the projected area and drag coefficient of a drifting body, and some ranges of values in which they should lie.

To obtain results for the projected surface area parameter, several data acquisitions are made on a full-size dummy, using a laser scanning method and photogrammetry. Once these data collected, they allow the creation of a 3D digital model that can be adjusted according to the desired configuration in order to be adaptable to the experiments that will be carried out later. The projected surface of the dummy is calculated for a series of rotations along different axes in order to establish an initial database that can be used later.

Then, the experimental setup for obtaining the drag coefficient values is establish in the wind tunnel on the full-scale model. This is carried out on the full-scale model after it was modified so that it can be placed as desired in the wind tunnel. The speed range is between 3.1 and 9.4 m/s with Reynolds numbers in a range between $9.3*10^5$ and $3*10^6$.

This wind tunnel experiment provides a first estimation of the drag coefficient values of the full-scale model and these values are compared with other literature results obtained in wind tunnels in various fields such as cycling, skiing or skating.

Finally, the prospects for improving the experimental set-up and the results obtained during the 3D digitisation will be discussed.

Résumé

Il n’existe actuellement pas de modèle précis et complet pour la recherche de victimes de noyade en zone urbaine. Cette thèse a donc pour but de contribuer à la création d’un tel modèle, en se concentrant sur la calibration et la validation d’un dispositif expérimental en soufflerie effectué sur un modèle à échelle réelle.

Pour se faire, les modèles de recherche de noyés existants et leurs équations ont été analysés, des modèles de dynamique des fluides appliqués au corps humains seront aussi révisés, ainsi que des articles sur la position du corps d’une personne qui se noie. Cela a permis d’en ressortir deux paramètres essentiels à un modèle de ce genre, qui sont la surface projetée et le coefficient de trainée d’un corps à la dérive, ainsi que certaines gammes de valeurs dans lesquels ils devraient se trouver.

Pour obtenir des résultats concernant le paramètre de surface projetée, plusieurs acquisitions de données vont être effectuées sur un mannequin à taille réelle, à l’aide d’une méthode de scan laser et de la photogrammétrie. Une fois ces données récoltées, elles vont permettre la création d’un modèle numérique 3D qui pourra être ajusté suivant la configuration voulue pour pouvoir s’adapter aux expérimentations qui seront réalisées par la suite. La surface projetée du mannequin sera calculée pour toute une série de rotation selon différents axes afin d’établir une première base de données utilisables par la suite.

Ensuite, le dispositif expérimental permettant d’obtenir les valeurs de coefficient de trainée sera mis en place en soufflerie sur le modèle à taille réelle. Il sera effectué sur le mannequin à taille réel après que ce dernier ait subi des modifications pour permettre de le placer comme désiré dans la soufflerie. La plage de vitesse sera comprise entre 3.1 et 9.4 m/s avec des nombres de Reynolds compris entre $9.3*10^5$ et $3*10^6$.

Cette expérience en soufflerie va permettre une première estimation des valeurs de coefficient de trainée du modèle taille réelle et ces valeurs seront comparés avec d’autres résultats de la littérature obtenus en soufflerie dans divers domaines tels que le cyclisme, le ski ou le patinage.

Enfin, les perspectives d’amélioration du dispositif expérimental et des résultats obtenues lors de la numérisation 3D seront discutées.

Contents

List of tables and figures

1. Introduction

In 2021, the Centre for Research on the Epidemiology of Disasters (CRED) recorded in its emergency events database (EM-DAT) a total of 432 disastrous events due to natural hazards worldwide (CRED, 2021). A number that is higher than the average 357 disastrous events per year from 2001 to 2020 (CRED, 2021). A disastrous event is report by the CRED when at least one of the following criteria is fulfill: a minimum of 10 people report as killed, a minimum of 100 evacuated people, declaration of a state of emergency or a call for international assistance. The mortality for 2021 years for flood (Figure 1) was of 4143 persons (persons missing considered as allegedly death).

The flood is dominant in those events with 223 occurrences, once again higher than the average 163 flood events for 2001 to 2020. From June to September, flood due to the monsoon season cost 1282 lives in India. Two other fatal flooding events occur in China and Afghanistan in 2021 (Figure 1). Floods are therefore increasing in 2021 compared to its average over the last 20 years and this number will continue to increase in the further years as a result of the impact of the global warming.

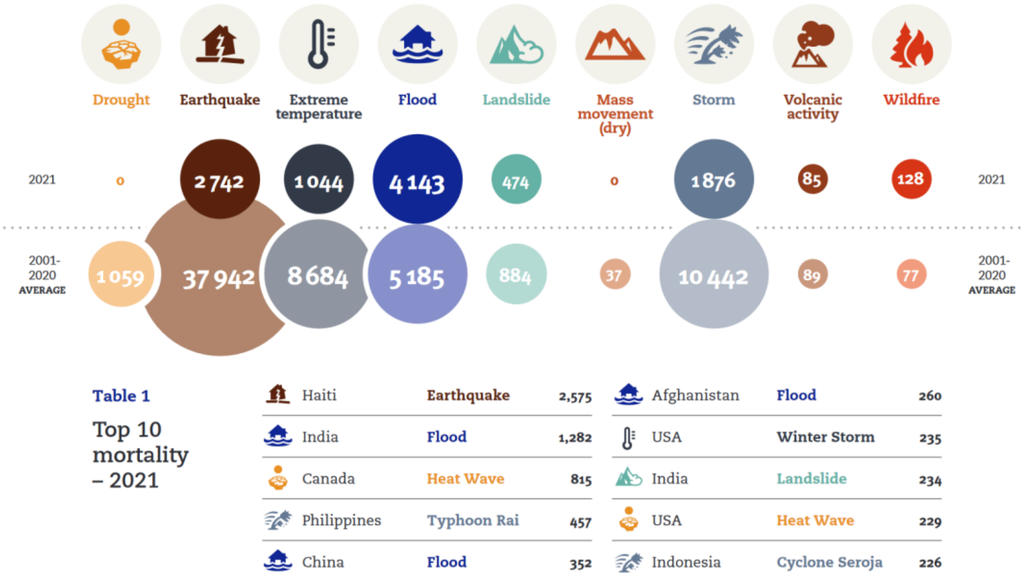

Table 1

Top 10 mortality – 2021

Haiti	Earthquake	2,575	Afghanistan	Flood	260
India	Flood	1,282	USA	Winter Storm	235
Canada	Heat Wave	815	India	Landslide	234
Philippines	Typhoon Rai	457	USA	Heat Wave	229
China	Flood	352	Indonesia	Cyclone Seroja	226

Figure 1 - Mortality by type of disastrous event for 2021 compared to the average value for 2001 to 2020, and the top 10 mortality event for 2021 (CRED, 2021)

The risk of flood is a worldwide problem that can be address to all countries. Indeed, a significant number of floods occur every year. On the week from 1 to 7 August 2022, 13 floods were report by the Emergency International Disaster Database in Honduras, Indonesia, Sri Lanka, Gambia, Nepal, Nigeria, Japan, Senegal, Mexico, Yemen, Philippines, California and Chad (CRED,2022).

The floods of July 2021 in Central Europe -resulting in high human (over 200 persons killed) and material loss- are a striking proof of the risks that Belgium or other European countries may face in the future. This was a major flood, especially for Germany for whom this disaster is rank 11th for the more economically costly event from 2001 to 2021. Although the number of death person by disastrous incident in Europe is lower than for other countries (Figure 2), it is still of 2.9% share with other countries in 2021 (and 12.2% from 2001 to 2020) which is not negligible (CRED,2021). Moreover, 41 percent of the weather related disasters are floods in Europe from 2001 to 2020.

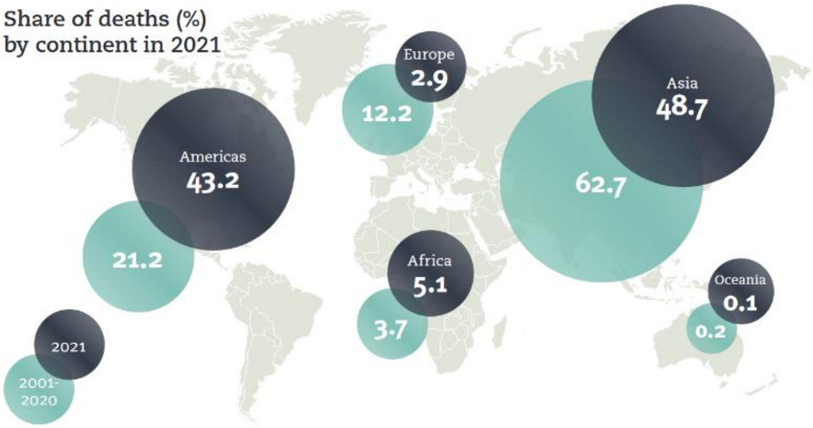

Figure 2 - Share of deaths (%) by continent in 2021 and comparison with the share of deaths from 2001 to 2020 (CRED, 2021)

But in addition to the drownings due to the flood, other type of drownings can occur and must be taken into account. The World Health Organization estimates that the annual worldwide incidence of death by drowning is around approximately 400,000 victims (WHO, 2002).

Research for missing persons will vary according to the equipment available and the location where it will take place. The investigation is not always easy to be carried on, resulting in low chances to find the drowning body of a person or at least increasing the economic cost of the incident.

The objective of this dissertation is therefore to help in the improvement of a tool for the search of victims by drowning in urban area, by the calibration and validation of an experimental setup on a real-scale model. This will permit a better overview of the range of values of the drag coefficient occurring when a person is drowning in a chosen physical posture. These data will be useful for the realization of a model developed to improve the casualty search, which requires the use of the drag equations as a driving force.

In Section 2, firstly existing drowning models will be review with their drag equations, then projected surface and drag coefficient available in the literature will also be overlooked and an explanation of the position of the drowning body will be discussed. In Section 3, we will focus on the projected surface area and thus in the development of numerical tools to obtain this value from a real-scale model. In Section 4, the experimental setup to obtain values of drag coefficients will be detailed along with the resulting experimental data. Finally, in Section 5 the perspective of improvements will be discussed.

2. Background

First of all, different relevant literatures in link with the subject studied will be summarized. These articles will address the following two main topics: the position of a drowning body and the Computational Fluids Dynamics (CFD) applied to the human body. It will help to specify the objectives of this master thesis and the way in which they can be achieved.

2.1. Available numerical model

Only few numerical models have been conducted in the search for missing persons by drowning, notably Carniel et al. (2002) and Ebbesmeyer et al. (1994). The two articles simplify the shape of the drowning model by using a sphere shape instead. Indeed, the paper of Carniel et al. (2002) is more concerned with oceanic circulation and dynamic than with the shape of the human model used to obtain its numerical model. The model does not take into account the vertical aspect of the body, considering that it was a floating object. Furthermore, these studies are carried out in rather marine environments, which differs from the urban environment.

Some other models have been worked on based on the simulation of the transport of a cylinder in a two-dimensional stream (Ghaffarian et al., 2020; Persi et al., 2019) and permit to determine some important parameters needed to solve the calculation of the motion of such an object through equation (1).

$$\left(m_b + \frac{1}{2} C_{AM} m_f\right) \frac{d\overrightarrow{U_b}}{dt} = \frac{1}{2} p_w A (C_D + C_s)(\overrightarrow{U_w} - \overrightarrow{U_b})^2 + m_f \left(1 + \frac{1}{2} C_{AM}\right) \frac{D\overrightarrow{U_w}}{Dt} \qquad (1)$$

With m_b the mass of the body, C_{AM} the added mass coefficient, m_f the mass of surrounding fluid, $\overrightarrow{U_b}$ the velocity of the body, p_w the water density, A the frontal area, C_D the drag coefficient, C_s the side coefficient and $\overrightarrow{U_w}$ the water velocity.

Thus, to improve the accuracy of the Carniel et al. (2002) and Ebbesmeyer et al. (1994) papers, it would be interesting to know the position of a drowning body and then to look at other articles where the shape of the human body is used even if their applications and positions are not the same. This will give an idea of the frontal area A and drag coefficient C_D of a human body.

2.2. Position of a drowning body

Drowning is defined as “suffocation by submersion, especially in water” by Modell (1981).

Initially, the drowning victim will panic and have disordered movements. Generally, the victim alternates between two phases: sinking into water and then rising out of the water. These two phases are known as the corking effect. This effect is due to the weight of the displaced water volume being equal to the thrust from the bottom upward. During this phase, the limbs usually tend to make shaky movements due to an attempt to emerge. As the movements become slower over time, the body will be completely submerged and the limb movement will continue to decrease until it stops (Marrone et al., 2021).

From a pathophysiological point of view, the phases of the drowning process are: a breath-holding phase, then an involuntary inspiration phase, then the victim will gasp for air and finally lose consciousness. These phases vary according to the victim. The brain will undergo a cerebral hypoxia which means that the brain is no longer oxygenated and this hypoxia leads to brain damage. The death is secondary to the development of this hypoxia (Farrugia et al., 2011).

The effects of immersion on the cardiovascular system are an increase in venous return and a central shift in blood volume. This leads to an increase in blood volume (except in some case in salt water which may lead to a decrease in blood volume). The change in blood pressure during drowning is due to the hypoxia (North, 2002).

A human body is under the action of two opposite forces: the force of buoyancy and its weight. The first is upward and is due to the weight of water and the second is downward. Seawater has a gravity of 1020-1030 kg/m^3 and freshwater has a gravity that is 2-3% lower. The human body floats as long as the gravity of the corpse is lower than that of the liquid (Lunetta et al., 2014).

The buoyancy of a human body is very close to the buoyancy of seawater (Table 1). But the clothes affect this floatability and is one of the main factors of uncertainties when trying to predict the body weight. In comparison, the human body has a higher gravity than freshwater and corpse will then be more likely to drown in fluvial environment.

Table 1 - Gravity of different items (Lunetta et al., 2014)

Item	Density (g/m^3)
Seawater	1.020-1.030
Freshwater	1.000-1.009
Adult without clothes	1.035-1.110
Most internal organs	1.01-1.09
Skeleton	1.97
Adipose tissue	0.94

The respiratory cycle changes the density of the body, with air reducing the density of a body. Indeed, in a study realized by Donoghue et al. (1977), of 98 male volunteers, with functional residual capacity, 69% of them could float on seawater and 7% on freshwater. Due to the low specific density of the air-filled trunk, the body will be in a head-down position although in some cases, the body may float with the face upward.

Once death, the victim will experience livor mortis, which is the accumulation of blood in several parts of the corpse due to gravity (Sampson et al., 2022). This blood will therefore cause the victims upper and lower limbs to point downwards.

The human body once death, will then go through different phases. First, it will sink, due to an increase in hydrostatic pressure caused by the compression of gases in the body. Movements on the bottom can lead to injuries, mainly due to abrasion. Then the post-mortem gases develop in the body and cause the specific gravity to decrease. Part of the victim's back will resurface, with the limbs still pointing to the bottom, below the surface of the water. The interval between these two phases is variable, depending on the environment. The body will continue to float until the gases are released during the decomposition (Lunetta et al., 2014).

In light of the literature on the position of a drowning body, a reference position (Figure 3) can be chosen - with the trunk at about 30° to the horizontal axes and the limbs pointing downwards. Moreover, the head of the rescue brigade interviewed by Delhez (2021) confirmed the recurrence of this position. Other positions will support drowning phases that do not correspond to this reference position.

Figure 3 - Picture of the reference position of a model: front and profile view

2.3. Computational Fluid Dynamics model results of drag coefficient

CFD stands for Computational Fluid Dynamics. It is a part of fluid mechanics that uses numerical analysis to solve problems related to fluid flow. Here the focus will be on a very small part of CFD, which can be applied to the search for missing persons by drowning – using for example articles that will focus on the CFD of swimmers. This will give an idea of the drag coefficient values that should be obtained.

Indeed, swimming is a major athletic sport and to optimize the thrust and drag of a swimmer many efforts are made. CFD is a method observing and understanding the movement of water around the human body. The CFD for the swimmer addresses two main topics of interest which are the propulsive force of the propelling segments and the drag forces resisting forward motion. This propulsion will be of less interest in the case of a drowned body but some differences between CFD and experimental data can be highlighted as they are likely to be the same in the case of a dead body (Marinho et al., 2009c).

Bixler et al. (2007) found that the difference between the value obtained with a CFD and that obtained with an experimental approach was around 4% and therefore proved that CFD was accurate and could be used in swimming research. Especially as the model used for the CFD and the experimental results may differ, which leads to difference in the results and explains part of the percentage difference between the two methods. If this percentage is the same for a drowned body, then CFD could be a very good way to obtain results in the search for missing persons by drowning. The study also shows that the drag coefficient of a real swimmer is higher than the coefficient of a model due to the movement of the body. The difference between the skin of the swimmer which is flexible and that of a model could also have an effect on the results (Figure 4).

Gardano et al. (2006) compared the results between CFD trend and data measured in a wind tunnel for a human arm. The human arm was represented as a standard geometric solid, which is not as accurate as a true three-dimensional model of an arm. The results were obtained at low wind speeds under quasi-static conditions resulting in a Reynolds number between $7*10^6$ and $2*10^7$. The comparison between the two confirms the relevance of the low-speed wind tunnel for obtaining drag and lift coefficients in quasi static conditions.

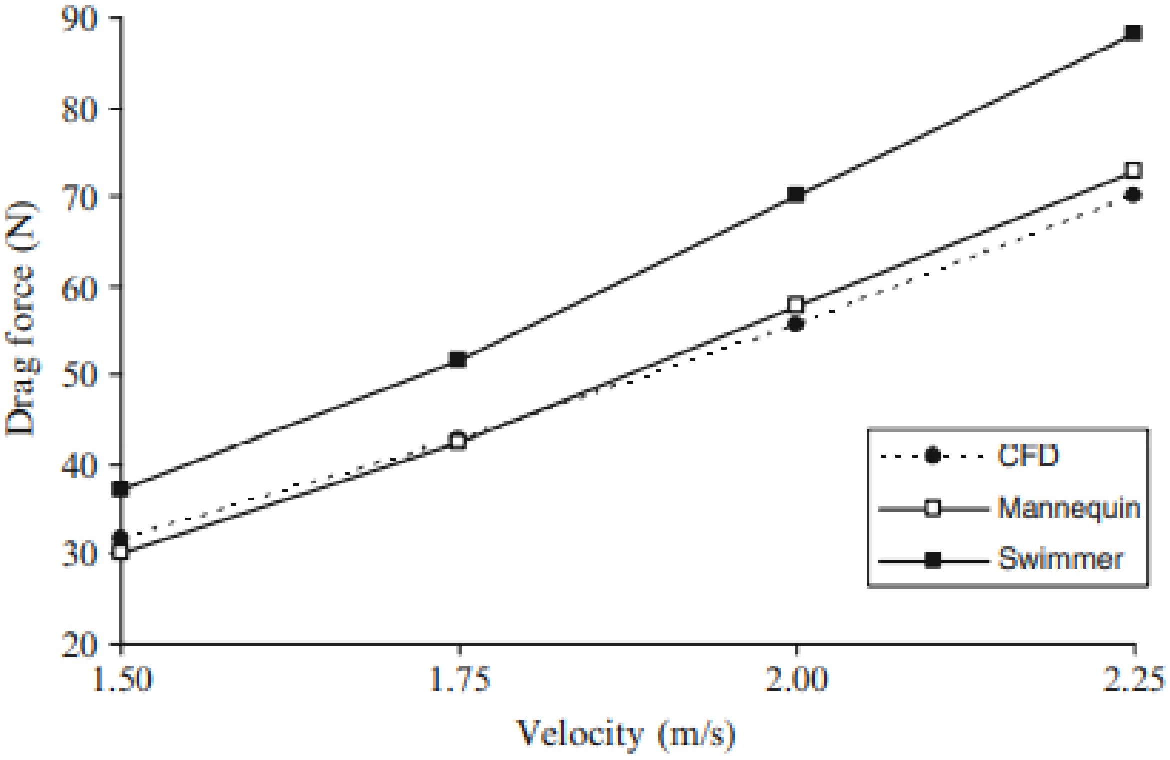

Figure 4 - Hydrodynamic drag force of the swimmer, CFD and the model (Bixler et al., 2007)

Although a lot of CFD work for human swimming has been carried out, in most cases the models are 2D or very simple 3D and these simplifications can conduct to misinterpretation. To avoid this problem, the reverse engineering process is used to build a virtual model. This process involves the use of a laser scanner to perform a three-dimensional mapping of the model. This process will capture a point cloud of a real object, edit this point cloud, then create a mesh with smooth surfaces to finally create a solid 3D model (Marinho et al., 2009c).

Some papers (Marinho et al., 2008 and Zaidi et al., 2008) focus on the gliding position of a swimmer. Marinho et al. (2008) investigated the gliding position with the arms alongside the trunk and with the arms extended forward (Figure 5 and Figure 6). These two positions have some similarities with the position of a body that could be found lying on the bottom of a river, with an upright body position. In the first position, the arms are along the trunk, which might be more consistent for a dead body (Figure 7). But both models experience a flow of 1.6 to 2 m/s, which is much more than a corpse lying on the bottom of a river would experience. In any case, the C_D of a body with its arms along the trunk is higher than that of a model with the arm extended (respectively 0.7 and 0.4) (Marinho et al., 2008).

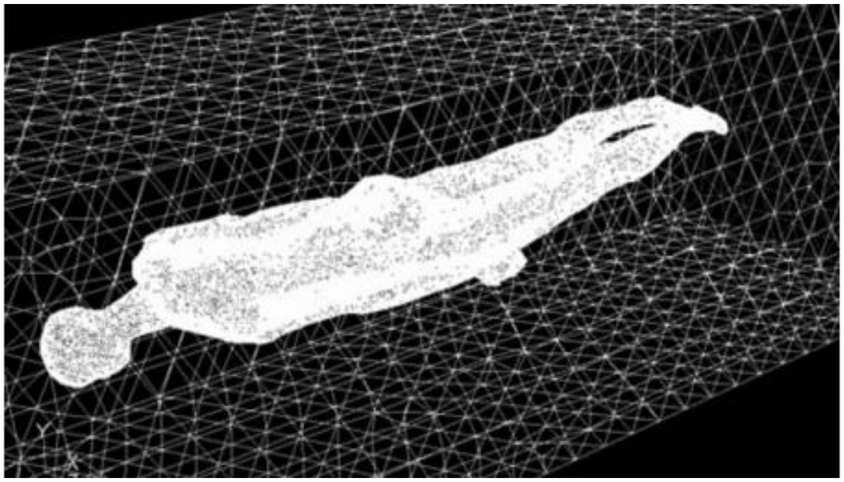

Figure 5 - The model used by Marinho et al. (2008) in a ventral position with arms alongside the trunk in the CFD domain

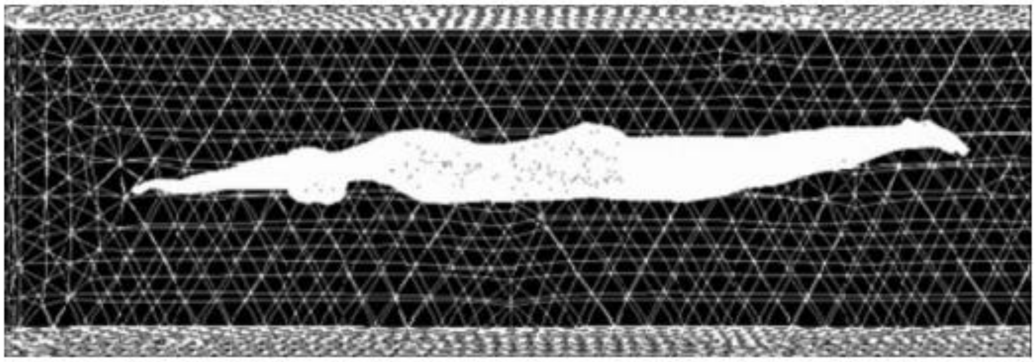

Figure 6 - The model used by Marinho et al. (2008) in a ventral position with the arms extended at the front with the shoulders fully flexed in the CFD domain

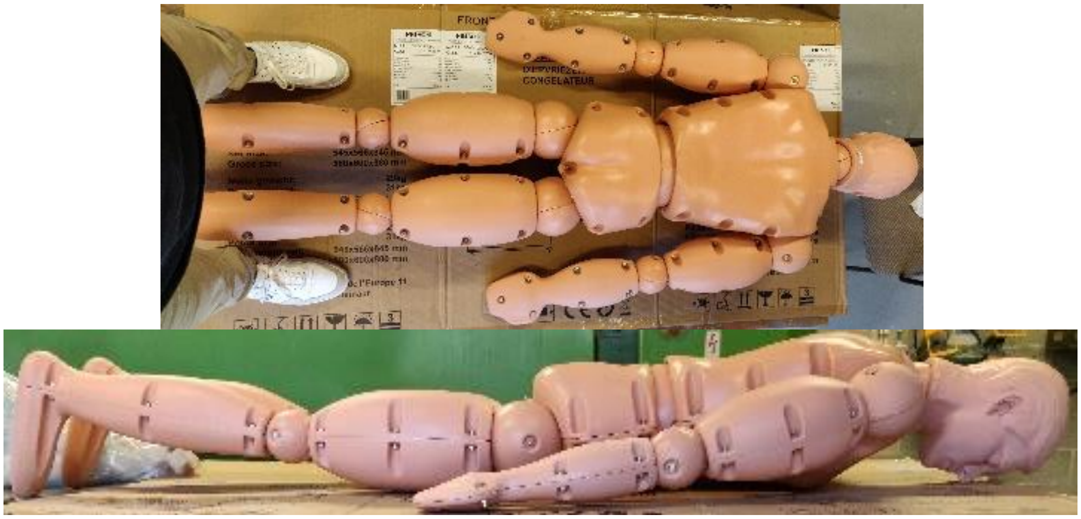

Figure 7 – Picture of a model in a ventral position with arms alongside the trunk (top view and profile view)

In swimming, three types of drag are involved: the skin-friction drag, the pressure drag and the wave drag. These drags are found in the case of a drowned body, although these forces do not always have the same direction. The skin friction drag depends on the flow velocity, and on the surface and characteristics of the body area. The pressure drag is the difference in pressure between the front and the back of the body. This drag can be influenced by the cross-sectional area of the body. Secondly, the wave drag may have little to no influence because the drowned body will be drawn towards the bottom of a stream. This drag was in any case not taken into account in the studies of Marinho et al. (2008a).

In the case of a swimmer moving through the water at rest, the pressure drag is dominant (>75%) and it takes into account the velocity of the swimmer (Figure 8).

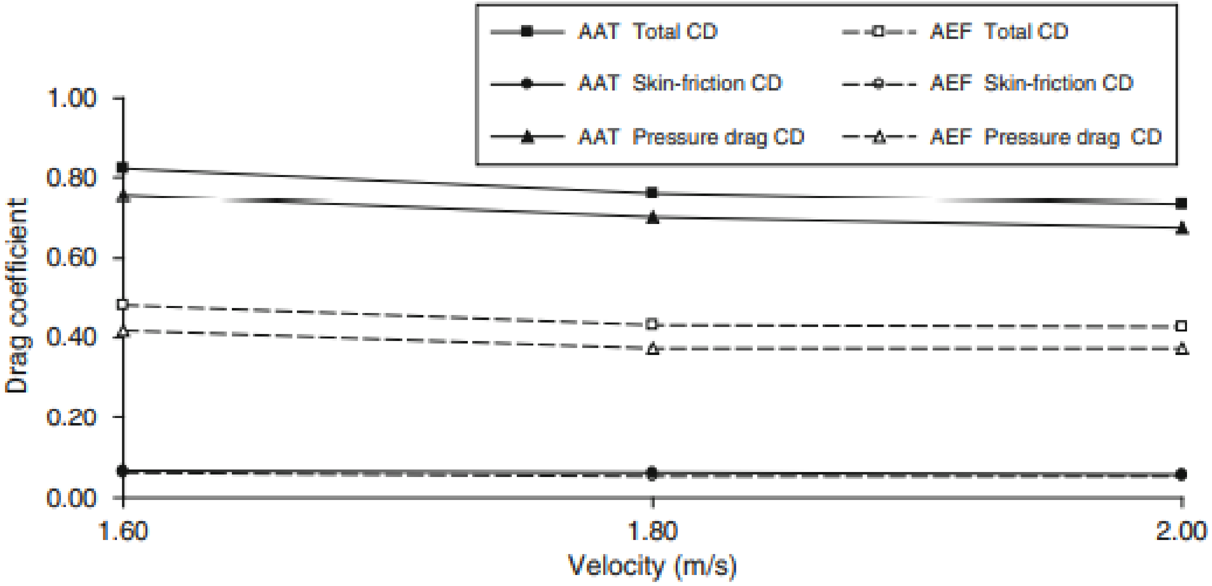

Figure 8 - Relationship between total drag, skin-friction drag and pressure drag and the gliding velocity for the positions with arms alongside the trunk (AAT) and extended at the front (AEF), from Marinho et al. (2008a)

2.4. Wind tunnel results of drag coefficient

The wind tunnel is an experimental tool that allows, among other things, to obtain the drag coefficient of an object. As with CFD, there are few articles that focus on the study of people who have drowned. Therefore, article related to different applications will be reviewed, articles which can be applied to our topic. This will give an idea of the values of the drag coefficient that should be obtained in wind tunnel tests.

Schmitt (1954) conducted a study to obtain the drag coefficient of a human body in a wind tunnel for a man of average stature. Lift, side force and moments were also acquired. The subjects were given five body positions: standing, sitting, supine and two squatting positions. The test for these positions varied according to the yaw angles and for a clothed or naked model. The weight, height, volume and surface area of each of the 8 subjects were known. For the supine position, which is closest to the drowned position (Section 2.2), the C_D obtained by Schmitt (1954) is between 1.5 and 4 for a wind speed of 27.49 m/s.

Another experiment conducted in a wind tunnel, but this time for speed skating, was led by D'Auteuil et al. (2012). This experiment was conducted on full-scale model to obtain an optimisation of the drag coefficient of a skater for different Reynolds number. The model had a single position: sidepush (Figure 9), which has the leg and torso in a position close to that of a drowned body (as discuss in Section 2.2), but not so much for the arms which are not pointing downwards. The drag coefficient should therefore be smaller for the skater compared to the coefficient of a drowning body. A test conducted in smooth flow revealed that the C_DA tends to decrease with the speed of wind and to be more stable above 40 km/h. The C_DA ranged from 0.09 to 0.1 for different winds speeds.

Figure 9 –Sidepush position in the test section (D'Auteuil et al., 2012)

A number of wind tunnel experiments have been carried out for cyclists, which are summarised on Table 2. The Figure 10 gives an overview of some of the positions used to obtain the results. This table shows the C_DA values obtained for a given wind speed, with values higher than those obtained for skating. These large variations between the different values available suggest that the projected surface area will have a huge impact on the results. Once again, the position differs from the one of a drowning body, especially with the presence of the bicycle. But these are tests carried on in quantity and which may prove to be valuable.

Table 2 - Comparison of drag areas for several wind tunnel experiments for cyclist model (Defraeye et al., 2010) with the results obtain for the model

Author	Position	Wind speed [m/s]	Drag area (C_DA) [m^2]	Test section size [m^2]	Number of cyclists
Kyle and Burke (1984)	Hill descent	9 – 15.5	0.23	3*2.1	1
Dal Monte et al. et al. (1987)	Time trail	15	0.246 – 0.254	9.6*4.2	1
Broker et al. and Kyle (1995)	Time trail	13.3	0.203	/	5
Zdrakovic et al. (1996)	Time trail	+/- 8.2	0.17 – 0.23	2.2*1.6	2
Gilbertini et al. (2008)	Time trail, dynamics	13.9	0.223	4*3.84	1
Garcia-Lopez et al. et al. (2008)	Time trail	15	0.260	3*2.2	5

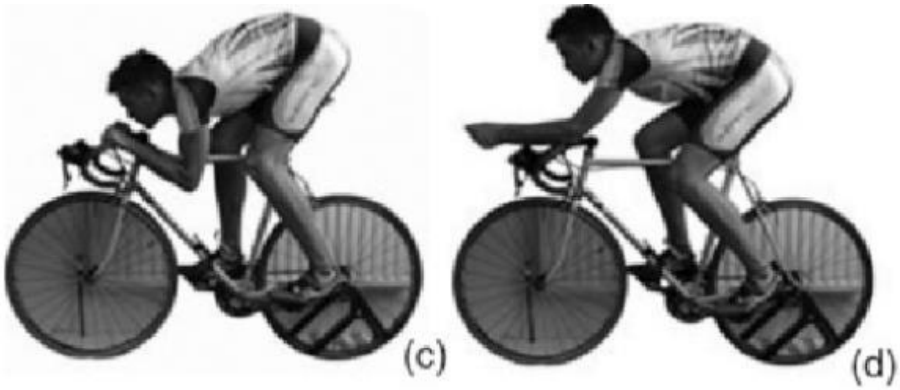

Figure 10 – (c) The Hill descent position, (d) Time trail position (Lukes et al., 2005)

The skying field is also a field where wind tunnel tests have been carried out. Indeed, air drag, frontal area and drag coefficient have been obtained by Ainegren et al. (2018) for different skying techniques. The advantage of this paper is that it highlights two main parameters needed in the calculation of a numerical model for drowning victims. Numerous positions were tested with for example the skier in different downhill positions (Figure 11). The air velocity varied between 6 and 14 m/s depending on the position studied and drag coefficients varied between 0.62 to 1.18. The C_DA tends to increase with the air velocity. The projected total surface of the different positions was calculated using a two-dimensional image, which may lead to an underestimation or overestimation of this value depending on the distance from the camera (Figure 12).

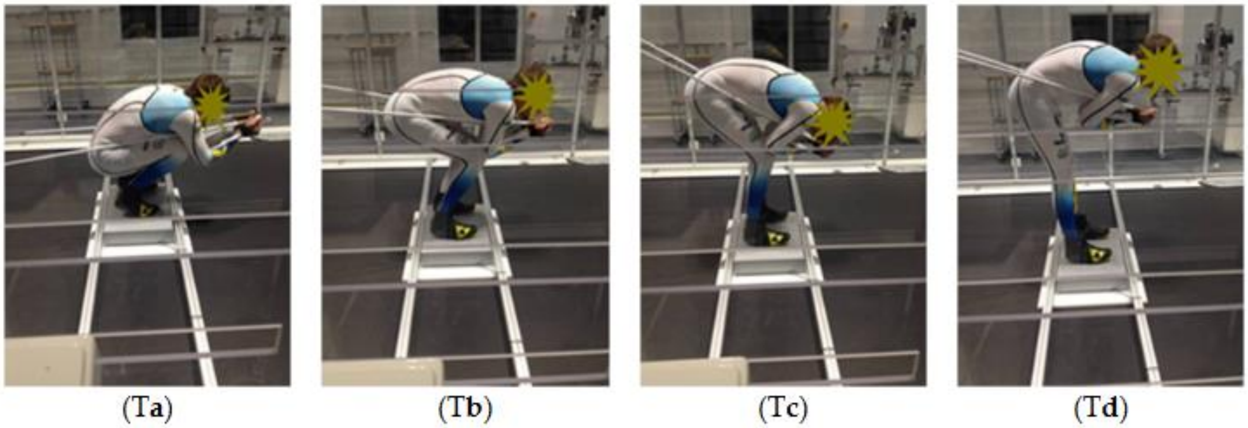

Figure 11 – Different positions of skying techniques (Ainegren et al., 2018)

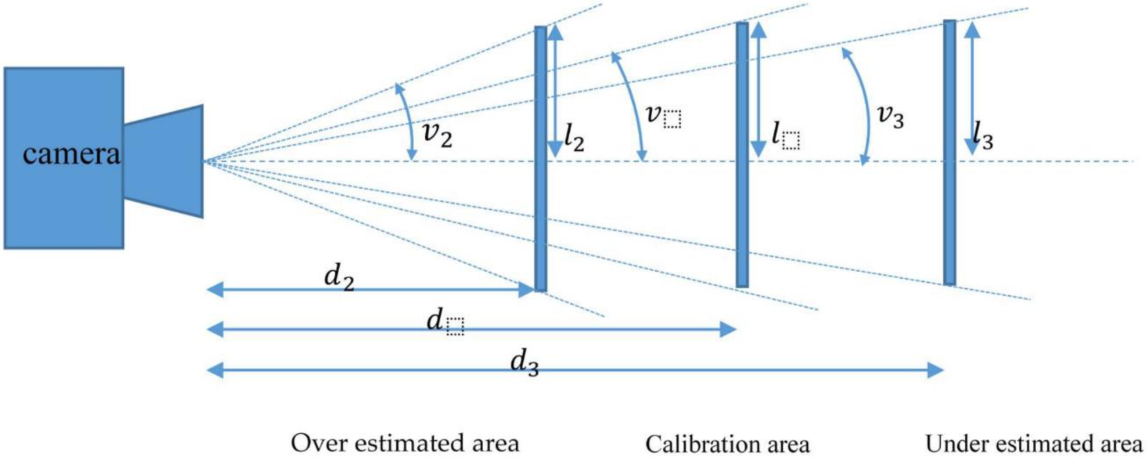

Figure 12 - How the calibration area with length l is perceived by a camera at different distances (Ainegren et al., 2018).

2.5. Objectives of this work

The present master's thesis is a contribution to research effort to predict the motion of a drowning victim in urban rivers. In a first step, a full-scale model is studied and compared to a human body. For this purpose, the positions reproduced by the model are compared with those of a human body, and then the frontal areas of the two bodies are compared in the same position from a numerical model and from the literature respectively. Then, the model is used in a wind tunnel and the measured drags compared with those of the literature for a human body. Once the experimental setup is validated, we can extend our study to the reference position of a drowning victim.

3. Numerical modelling

The objective of the numerical modelling part is to create a 3D digital model of the dummy (named Ken) that will be used in future experiments. In fact, it gives a better understanding of the geometry of the object and it allows to obtain the projected area of the model. The positions of the dummy used in the experimentation are described in the next section as well as the tools to obtain the model. Two acquisition methods will be completed and then four software packages will be used to compute the numerical model of the 3D body: Cloud Compare, Meshlab, Reality Capture and Blender. The main goal of the digitisation, in the end, is to obtain the projected surface area of the model at any position, as well as its total surface.

3.1. Description of the tools

3.1.1. Characterization of the model (Randy 9000)

The model shown below is the Randy 9000 produced by 3B Scientific. In this work, we will refer to it as Ken. It is a full-scale model designed to help firefighters rescue people from fires, from drownings and from other high-risk sites. It is made up of rugged polyethylene parts that are joined together using stainless steel hardware. Each part is waterproof. The joints have a large range of motion that is faithful to that of an adult man (Figure 13). It is designed to be customised, with empty parts in the body that can be filled with water or sand to weigh it down (Figure 14).

The rugged polyethylene of which the model is made has a very high reflectivity which will affect the quality of some of the results obtained later in Section 3.2. The large range of motion of the joints will also affect the results in Section 4 and several adjustments will have to be made to achieve a tolerable range of motion.

The weight of the model is 30.6 kg when empty and the height is 1m90 tall. When compared to a human body, Ken is not within the average size for a man, and his shoulders are particularly broad in comparison to those of Clément, our human model (Figure 15). The model does not belong to the average height or weight of the Belgian or any other European population as the parameters from Table 3 underline it. This should be taken into account when conducting experiments and especially when analysing the results.

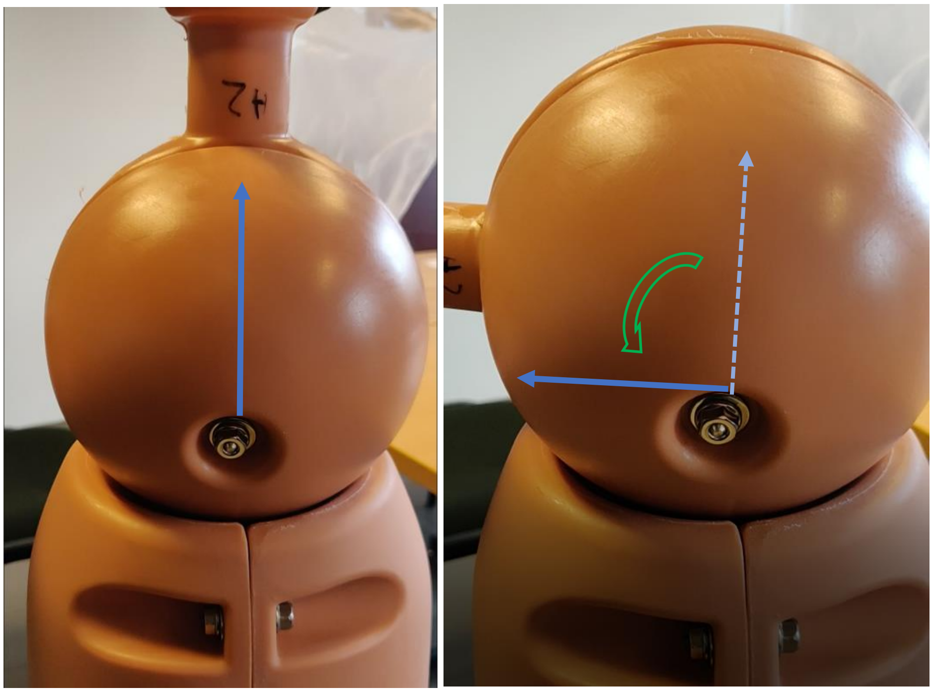

Figure 13 - Picture of the joint between the basin and the leg of the model, with different angles of motion

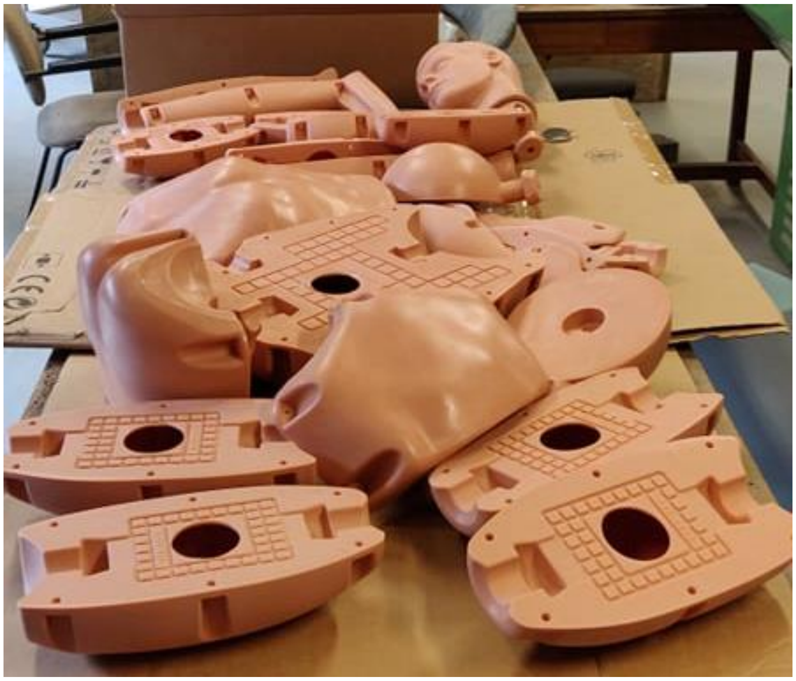

Figure 14 - Picture of Ken disassembled, where the holes which allow to fill Ken are visible

Table 3 - Comparison of the model and an average man for different parameters

	Ken	**Clément**
Height	1m90	1m85
BMI	(will be calculated in Section 3.2.5)	21.3
Shoulder larger	55 cm	47 cm
Inseam gap	94 cm	81 cm
T-shirt size	2XL	
Pants size	XL	

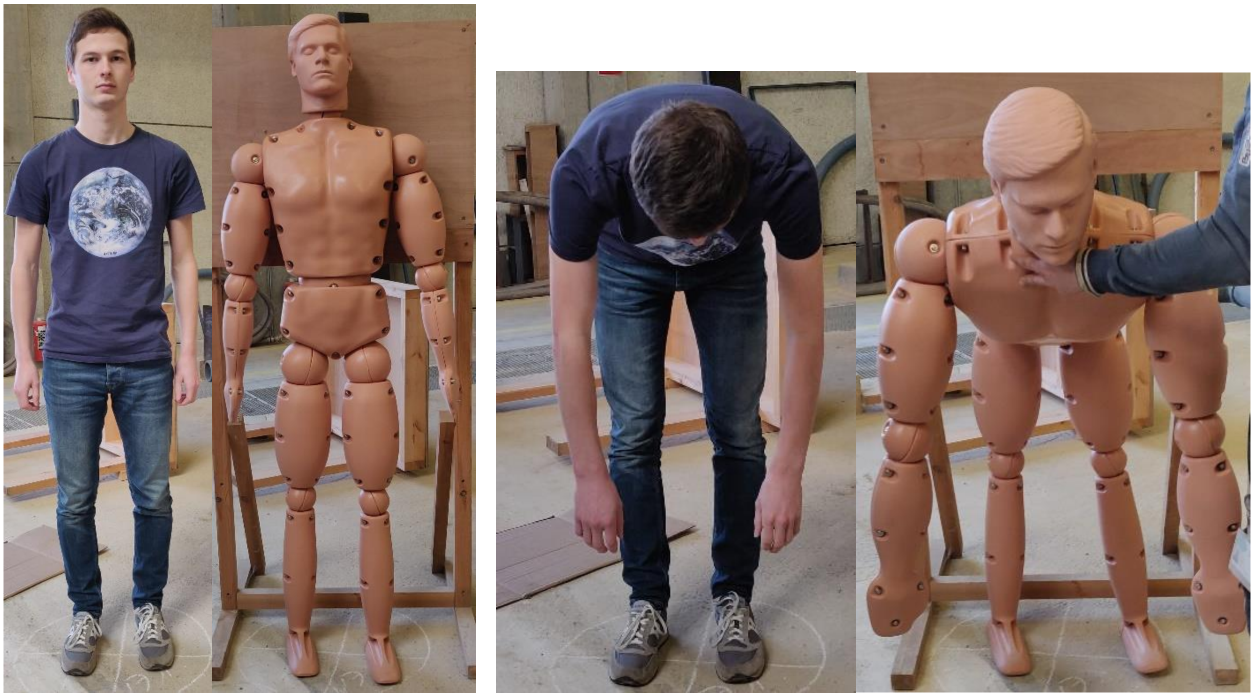

Figure 15 - Picture of the model from a frontal view for two main positions (configuration 1 on the left and 3 on the right) in comparison with the human body of Clément

Several key positions have been identified, which could be observed on a body in the case of a drowning victim. These positions are given and labelled in Figure 15 and Figure 16 and described in Table 4. The reference position corresponds to the drowning phase where there is still a little air in the drowning victim's lungs but the limbs are already weighed down by the liver mortis. The other configurations are intended to complete the other phases that may occur or to allow comparison with certain positions that can be found in the literature.

Table 4 - Description of the different configuration considered

Configuration	Description
1 – Standing position	Straight position from the legs, torso and head, with arms alongside the body
2 – Standing with arms outstretched	Straight position from the legs, torso and head, with arms outstretched at about 70° from the vertical axes
3 – Reference position	The torso has an inclination varying from 30° to 90° from the horizontal and the limbs hang down
4 –Belly on the bottom	Lying on the bottom, head down, arms alongside the body
5 – Back on the bottom	Lying on the bottom, head up, arms alongside the body

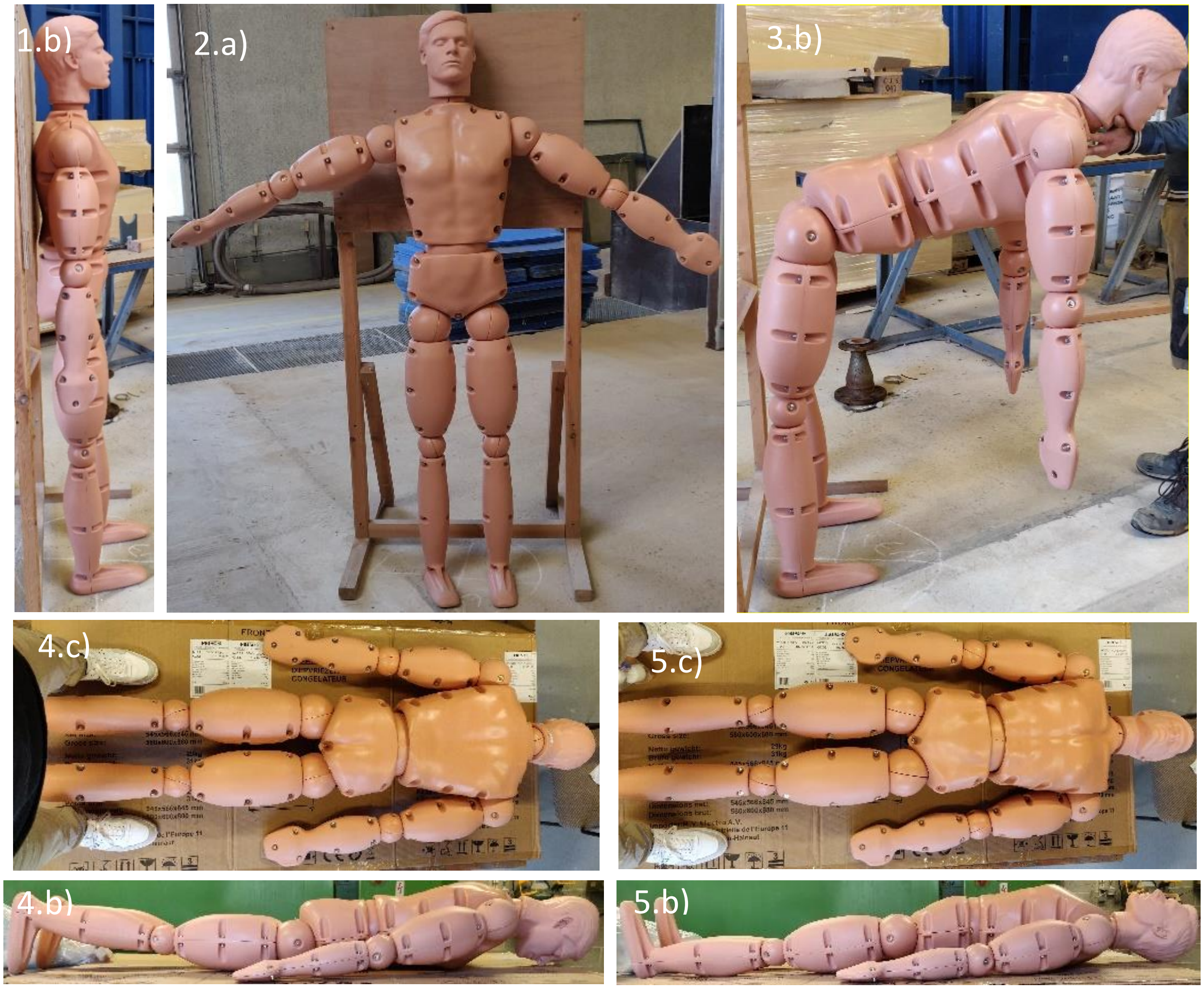

Figure 16 – Picture of Ken in the a) frontal, b) profile and c) top view for different configurations (numbered from 1 to 5)

3.1.2. 3D laser scanning

The 3D Scan has been realized using a laser scanning method. This is a method using laser light that can capture anything in its field of view. In this process, a laser line or a dot is project onto an object from the device and a sensor measures the distance to the surface of that object. To be more precise, laser scanning systems use a beam that will bounce off the surface and be reflected back to the sensor. The sensor then calculates the distance between the surface to itself by measuring the time it takes for the light to travel that distance. The mirror deflects the laser beam in a vertical direction onto the same object and an angle is encoded with the measured distance, giving a vertical angle. The horizontal angle is obtained by the 360 degrees rotation of the laser scan horizontally and is encoded as well (Berchon, 2014). The 3D laser scanning techniques are then refined to measure and inspect complex geometries such as the geometry of a 3D model and will give more accurate results than traditional methods (Virtanen, 2014). However, as the laser misses reserve side of target, which are not visible on a scan, it would be necessary to process more than one scan (Figure 17).

Laser scan collects the data in the form of a point cloud with XYZ coordinates. The spatial and dimensional aspect of the object will be well represented. This data is processed using numerical software such as Cloud Compare or Reality Capture which will be described in Section 3.4.

The 3D laser scanning used here to obtain data from the model is the BLK 360 from Leïca (Figure 18). Most of the time, it was placed on a tripod. The vertical visual field of the laser is 300 degrees and the horizontal one is 360 degrees. Four laser scans are performed, one in each corner of the room and a fifth scan is performed with the laser on the floor to collect information from beneath the model (Figure 19).

It is important to note that the errors related to the acquisition can have an impact on the results. Indeed, the surface of the model strongly reflects daylight, which leads to a lack of data in the point clouds for these highly reflective parts. Similarly, the accuracy of certain areas that are less accessible to the laser scanner, such as the armpits or the crotch can lead to errors.

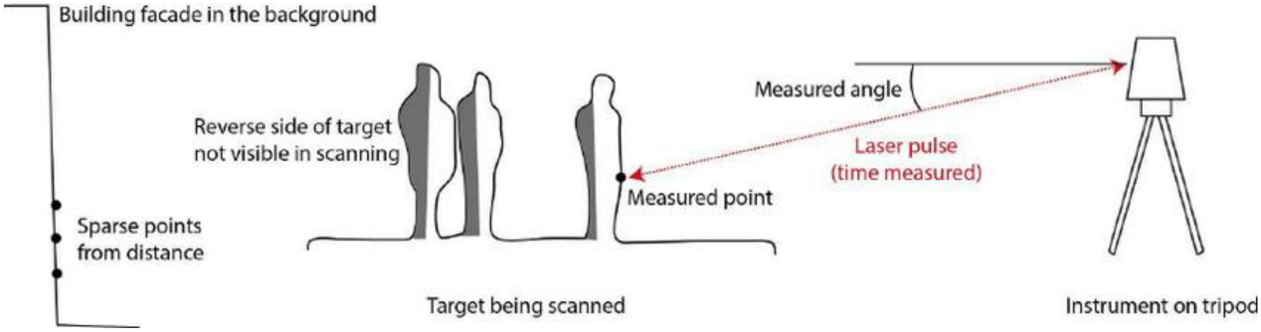

Figure 17 - Laser scanning principle (Virtanen, 2014)

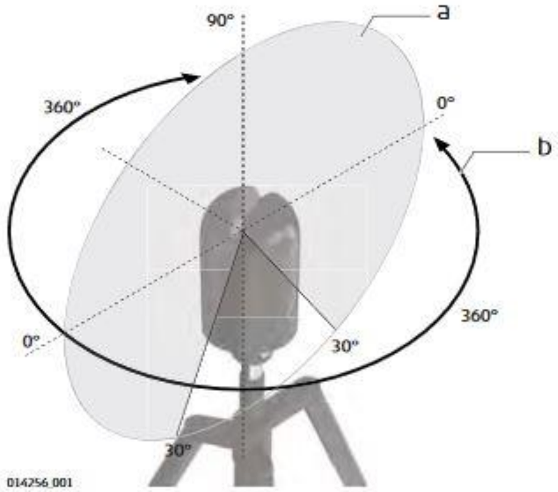

Figure 18 - A BLK 360 leïca on a tripod with a) Vertical visual field; b) Horizontal visual field (Leïca Geosystems AG, 2018)

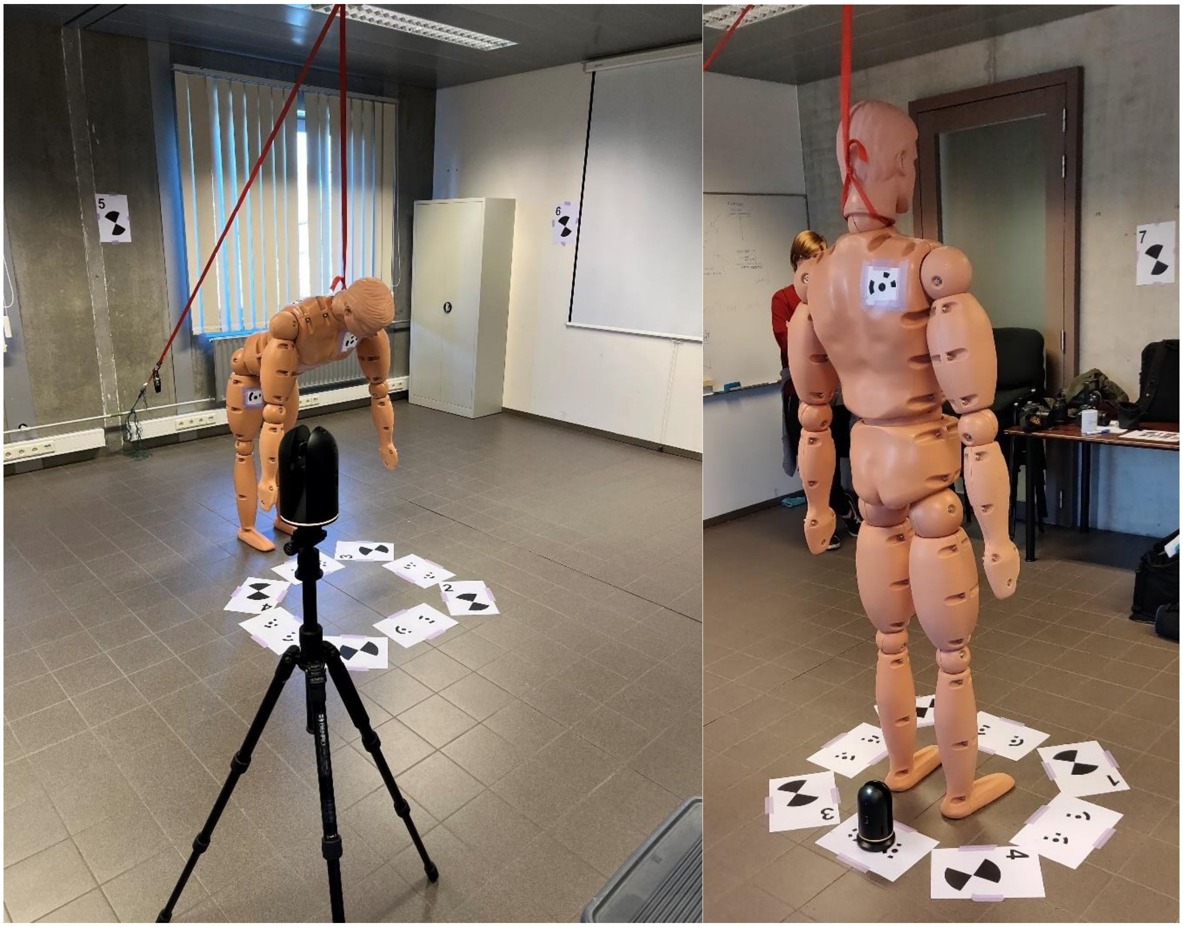

Figure 19 - Picture of the scanning completed on Ken, with on the left: the model in configuration 3 with the laser scan on a tripod and on the right : the model in configuration 1 with the laser on the ground.

3.1.3. Photogrammetry

The study of geometric picture analysis dates from the Renaissance with the appearance of the first principles of stereoscopy (Figure 20) and perspective (Mikhail, 2001). Stereoscopy is a technique which is used to achieve a three-dimensional effect, adding a sense of depth to an image. It is also the basic principle of the vision in depth with which man is endowed (Winkler, 2011).

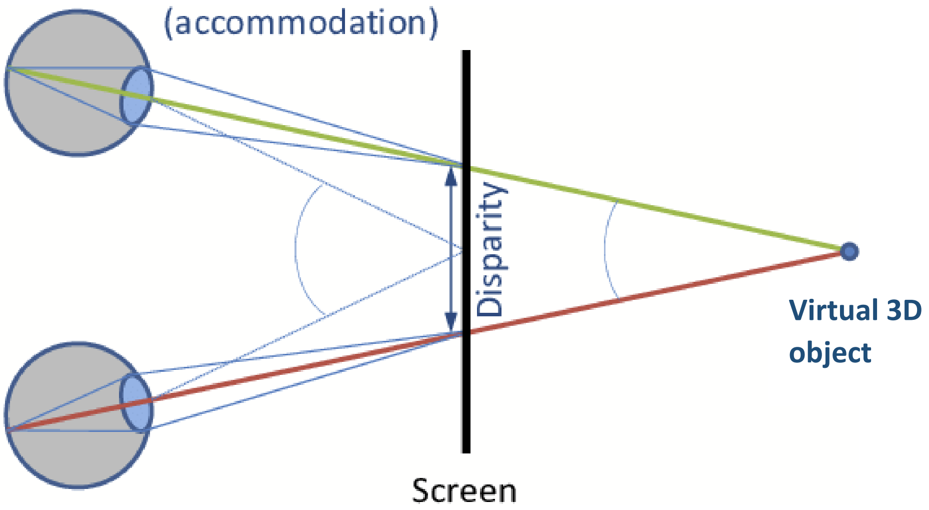

Figure 20 - Stereoscopic view of 3D object (Winkler, 2011)

In 1895, Professor Laussedat invented the photogrammetry technique, known at the time as the metrophotograhic procedure, designed to determine the three-dimensional geometry of an object from measurements taken on a photograph. This method not only makes it possible to see the relief but also to measure it. It is only at the beginning of the 20th century that the photogrammetry was industrialised and in 1909, the first aerial photographs from an aircraft were taken by Wilbur Wright and led to the use of aerial photogrammetry (Figure 21). It finally became digital in the 2000s. Thus, it is possible to invest the application of 3D measurements in the field with the creation of Digital Elevation Model (DEM). Nowadays, photogrammetry is used in many different fields such as geology, cartography, GIS, architecture or topography (Mikhail, 2001).

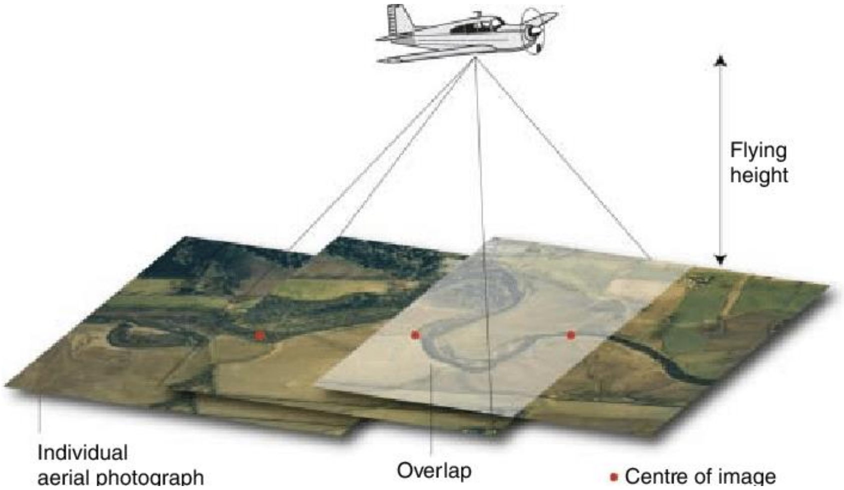

Figure 21 - Aerial photogrammetry principle

Photogrammetry uses a set of photos with a high percentage of coverage to reconstruct a numerical model. The advantages of such a method are speed, budget, accessibility and continuity. Indeed, a digital camera is enough to collect data, the acquisition is not too time-consuming and once the image processing skill is acquired, it is easy to provide a result and the method is without contact with the subject and allows to obtain a continuous representation of reality. It is a 3D technique whose mathematical model uses central projection (Stylianidis, 2020). In fact, it uses the parallax obtained between several images, taken from different point of view with a certain overlap. The more images are added, the more this method will be accurate (up to a certain threshold). The parallax is the effect of these different viewpoints on the images obtained (Figure 22).

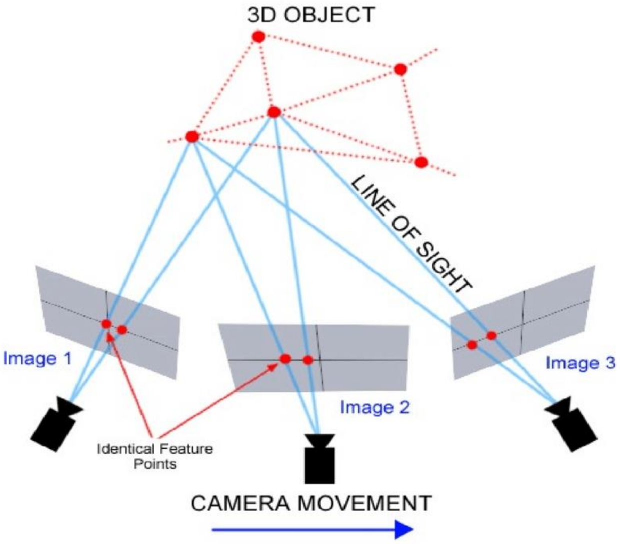

Figure 22 - Principle of photogrammetry (Tokkari et al., 2017)

Here the camera used is a Nikon D750 (Figure 23), in order to have good quality images for the first photogrammetry performed. The second camera used is a Nikon Z6 with a 50 mm lens and 40 mega pixels. Once collected, this data will also be processed using a numerical software (Reality Capture) which will be described later. The first acquisition consisted of 530 pictures, while the second included more pictures for a better accuracy due to counteract the reflectivity of the model. Those pictures have 80% coverage and were taken by walking in a circle around the model at different heights in order to cover the whole body. Additional photos were taken to ensure that the necessary amount of information was available for more sensitive areas such as the armpits, the crotch, etc.

It is important to note that errors related to the acquisition can have an impact on the results. Indeed, the surface of the model strongly reflects daylight, which leads to a lack of data in the point clouds for these highly reflective parts.

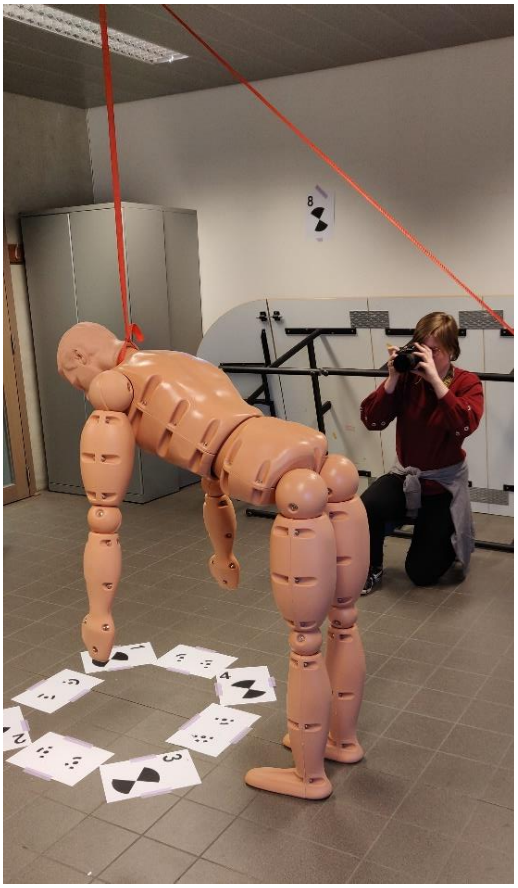

Figure 23 - Picture of the setup of Ken in configuration 3 while doing photogrammetry

3.1.4. Description step by step of the use of software to obtain the model

Cloud Compare is only used to analyze the 3D laser scanning images. Photogrammetry cannot be processed by this software. Cloud Compare is an open-source software that can process dense point clouds, so it is the reason why it was used in this case.

The point cloud (Figure 24) is processed to keep only the model and the floor beneath it. Cloud Compare's scalar field associates each point cloud with a numerical value and displays the colour field with the minimum saturation values of the scalar field in blue and the maximum saturation values in red (Girardeau-Montaut, 2015). This scale (Figure 24) allows us to see the areas that may have a deficit or a surplus of points.

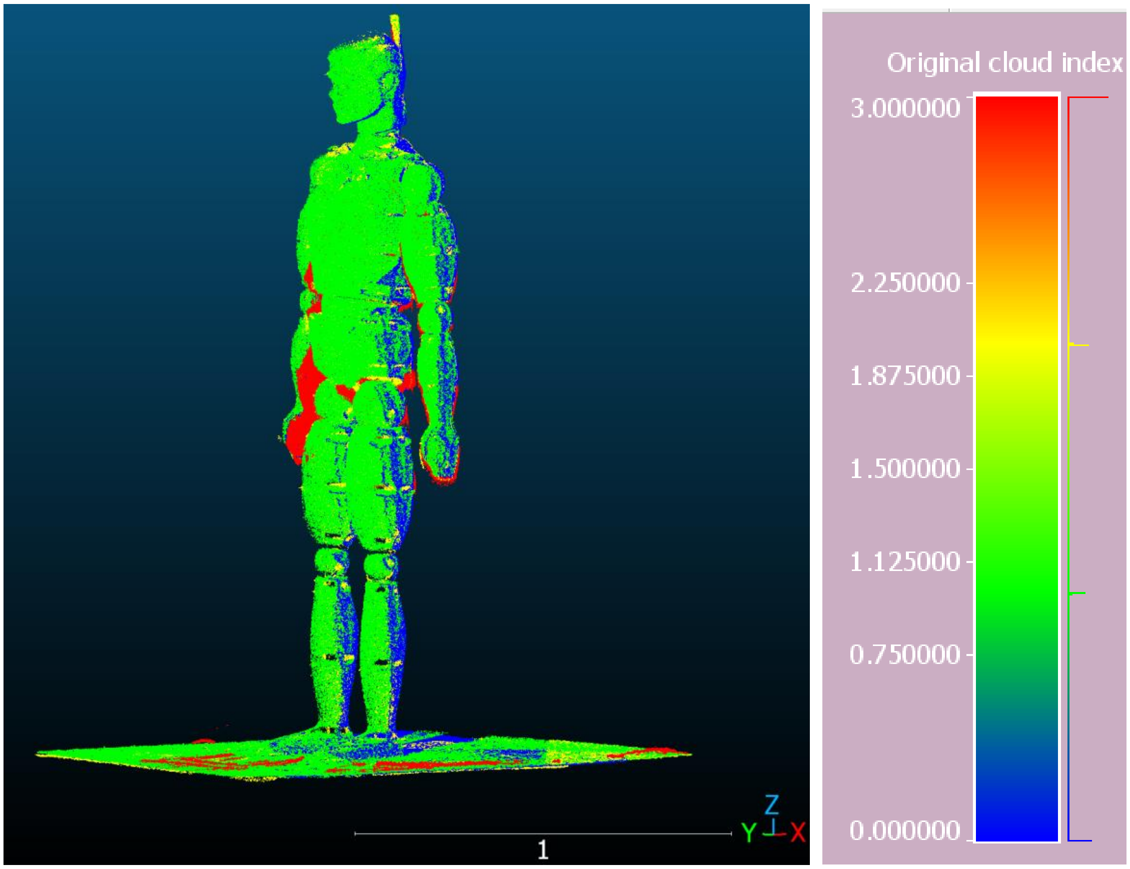

Figure 24 - Cloud points, results from 3D laser scanning on Cloud Compare (left), color-bar scale (right)

First of all, the point cloud needs to be cleaned in order to eliminate the outliers as well as the ground on which the model was located. The Cloud Compare tools used to perform this step are essentially *statistical outlier filter, segment* and *cross section. Statistical outlier filter* is a tool that will remove points that are far from the neighbours, the outliers. Therefore, extreme value with too much difference from others are removed and their impact on the modelled as well. The *segment* tool is a manual segmentation tool that refines the results obtained with the outlier filter. It allows the entities that are selected on the screen to be manually sliced. Finally, the *cross-section* tool is mainly used to cut out the soil layer on which the dummy was located (Girardeau-Montaut, 2015).

Once the point cloud is clean, the normals can be calculated using the *Compute normal* tool. The normal is a vector that represents the orientation of the surface of a polygon and is tangent to the plane (Figure 25). It can be used to visualise the reflectance of light (Nenad, 2018). Here, to obtain the most accurate normals, the quadratics model is used to obtain the polygons. This is because it is an accurate calculation for curved surfaces such as the one of the models. A number of local neighbours (equivalent to a sphere) must be selected to calculate the normals. To do so, a radius is chosen as the neighbour extraction process is based on an octree structure (Girardeau-Montaut, 2015).

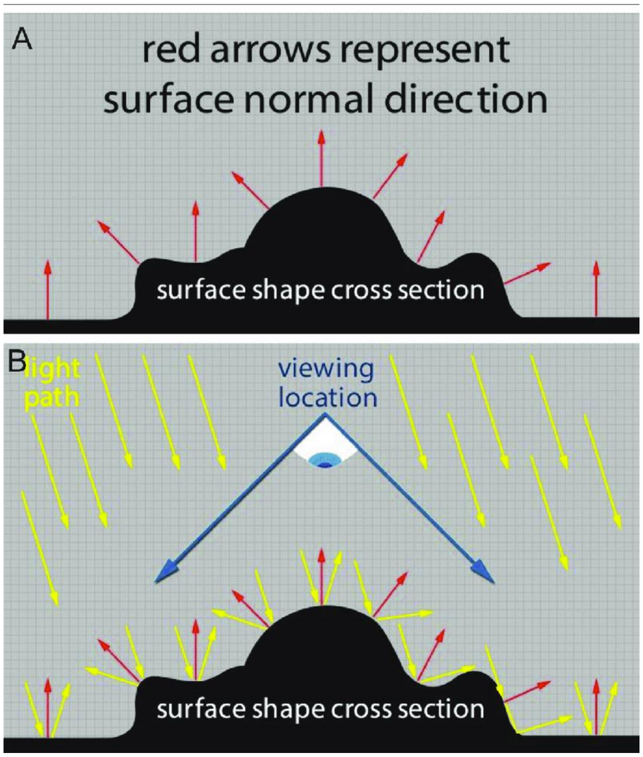

Figure 25 - Normals on a 3D shading model with the position of the normals vector (in red) and the visualization of the light reflectance (in yellow) (Nenad, 2018)

An octree structure (Figure 26) corresponds to the recursive partition of cubical volume of space and is initiated from the square bounding box of a cloud. The larger the radius, the smoother the generated normal. However, increasing the radius implies a longer processing time but it precises the normal. On the opposite, decreasing the radius may decrease the quality of the generated normal, which can even be considered invalid (Girardeau-Montaut, 2015). Here, after many tests on the model, the final radius chosen is 0.1027 m because with a larger radius, the computer is no longer able to process the information.

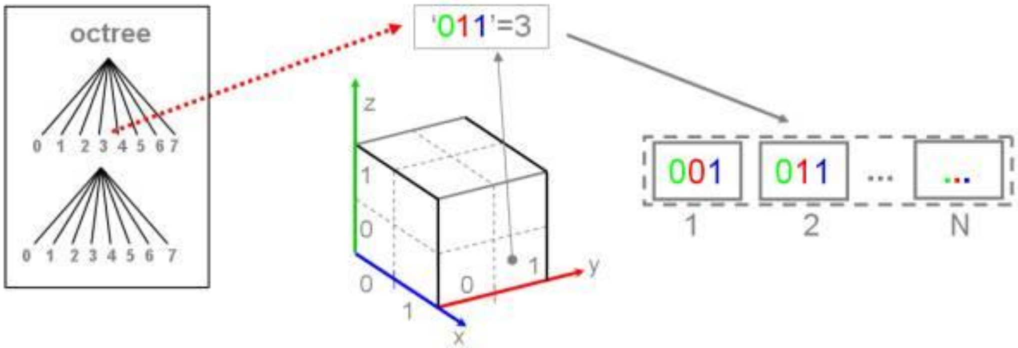

Figure 26 - Octree structure (Girardeau-Montaut, 2015)

To obtain a good orientation of these normals, the *Minimum Spanning Tree* (Figure 27) is used. This method reorients the normal of a cloud starting from a random point and propagates through the neighborhood. This method uses a subset of the edges of the connected neighbours and thus, the results are more accurate with a larger number of neighbours. However, if a large number of neighbours is chosen, the memory and time required to process the information will also be greater. Here, 12 neighbours are specified as beyond this number the computer will crash.

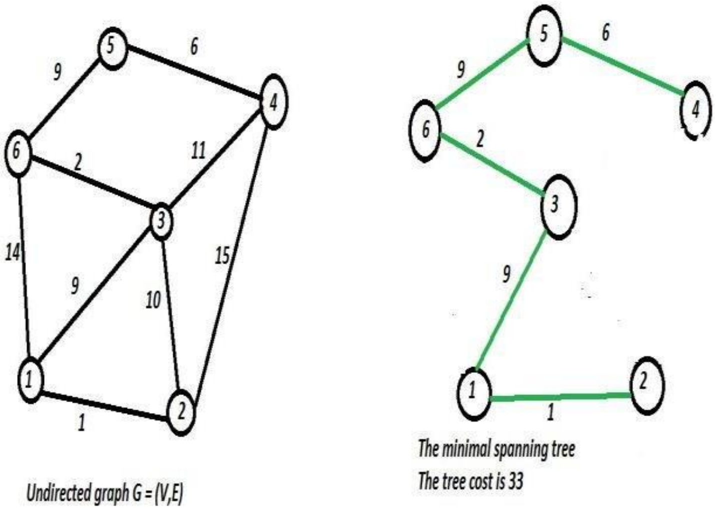

Figure 27 - Example of the minimum spanning tree method (Nabi, 2017)

The next step is to perform the triangulation to obtain the mesh of the 3D model. The software offers different types of triangulations such as Delaunay triangulation, or the one used in this case which is the *Poisson surface reconstruction*. This tool is an interface to the triangular mesh generation algorithm proposed by Misha Kazhdan et al. (2006). Indeed, Delaunay triangulation on a point cloud is a 2.5D method that will work best on very flat vertically oriented clouds and gives poor results in the case of the model. The *Poisson surface reconstruction* is a method that allows to construct a triangular mesh by solving a 3D Laplacian system with positional value constraints. Moreover, after comparison with other reconstruction methods, this method is considered to have a highly resilient to data noise. The surface is reconstructed using a shape indicator named χ which is 1 or 0 for points in or out of the cloud point respectively (Figure

28). This depends on the previously calculated normals. The points are represented by a vector field $\vec{V}$ and the goal is to find the χ that best fits this vector field (eq. 2). Then, the application of a divergence operator can be done and the problem can be process as a Poisson problem (eq. 3) (Kazhdan et al., 2006).

$$min_{\chi} \left\| \nabla_{\chi} - \vec{V} \right\| \qquad (2)$$

$$\nabla \cdot (\nabla_{\chi}) = \nabla \cdot \vec{V} \;\; \leftrightarrow \;\; \Delta_{\chi} = \nabla \cdot \vec{V} \qquad (3)$$

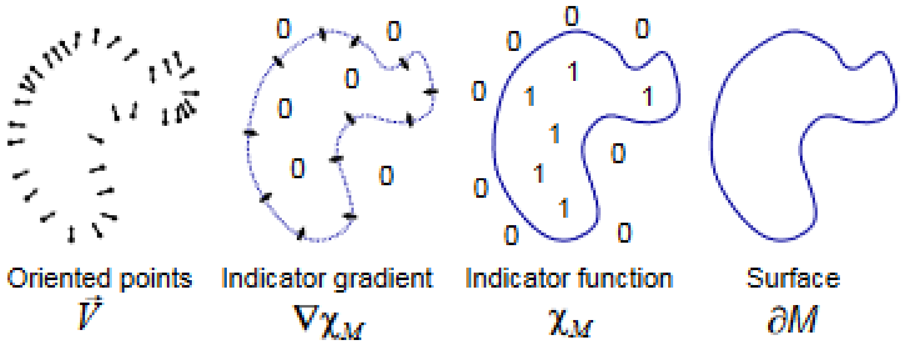

Figure 28 - Poisson reconstruction principle in 2D (Kazhdan et al., 2006)

Unfortunately, using this method on the whole dummy still gives many errors in the results or poor results (Figure 29) due to the differences of point density -especially in the arms and legs. To overcome this problem, the model is cut into five segments using the *segment* tool. The number of points for each part is shown on Table 5, and the difference between the left and the right limbs can be explained by the imperfection circle in black on the right and left side of the model in Figure 30. The different limbs are modelled individually (Figure 30) after recalculating the normal of each segment using the appropriate radius. Then, the 3D modeling of each segment is merged to obtain a better result.

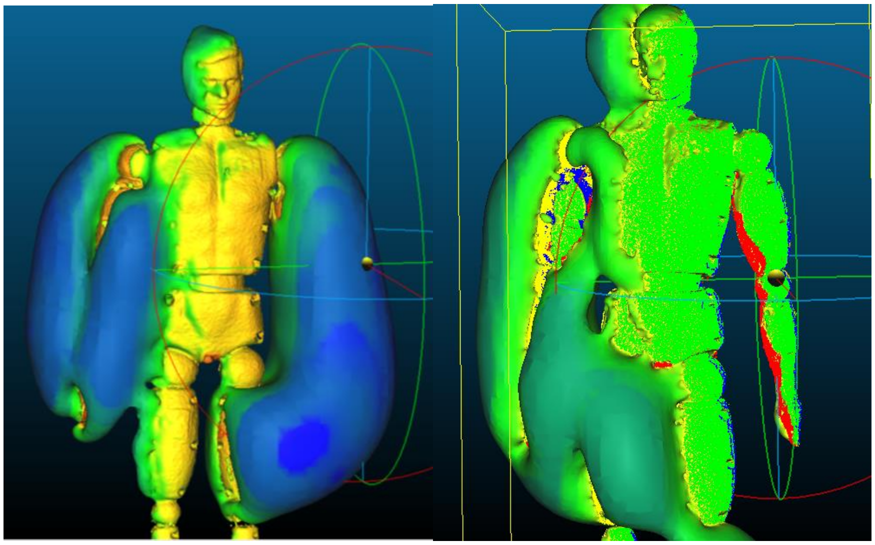

Figure 29 - Two results of the 3D modeling of the dummy using Poisson surface reconstruction

Some parts of the dummy are then still rough and a final segmentation, removing the points from the point cloud leading to these errors, is performed to obtain the final version of the model (Figure 31). This is the case for the head, the left arm and left leg.

Table 5 - Quantities of point from the cloud point for each part of the model

Body parts	Torso + Head	Left leg	Right leg	Left arm	Right arm
Number of points associated	10,660,327	1,179,559	1,017,950	1,191,891	1,353,153

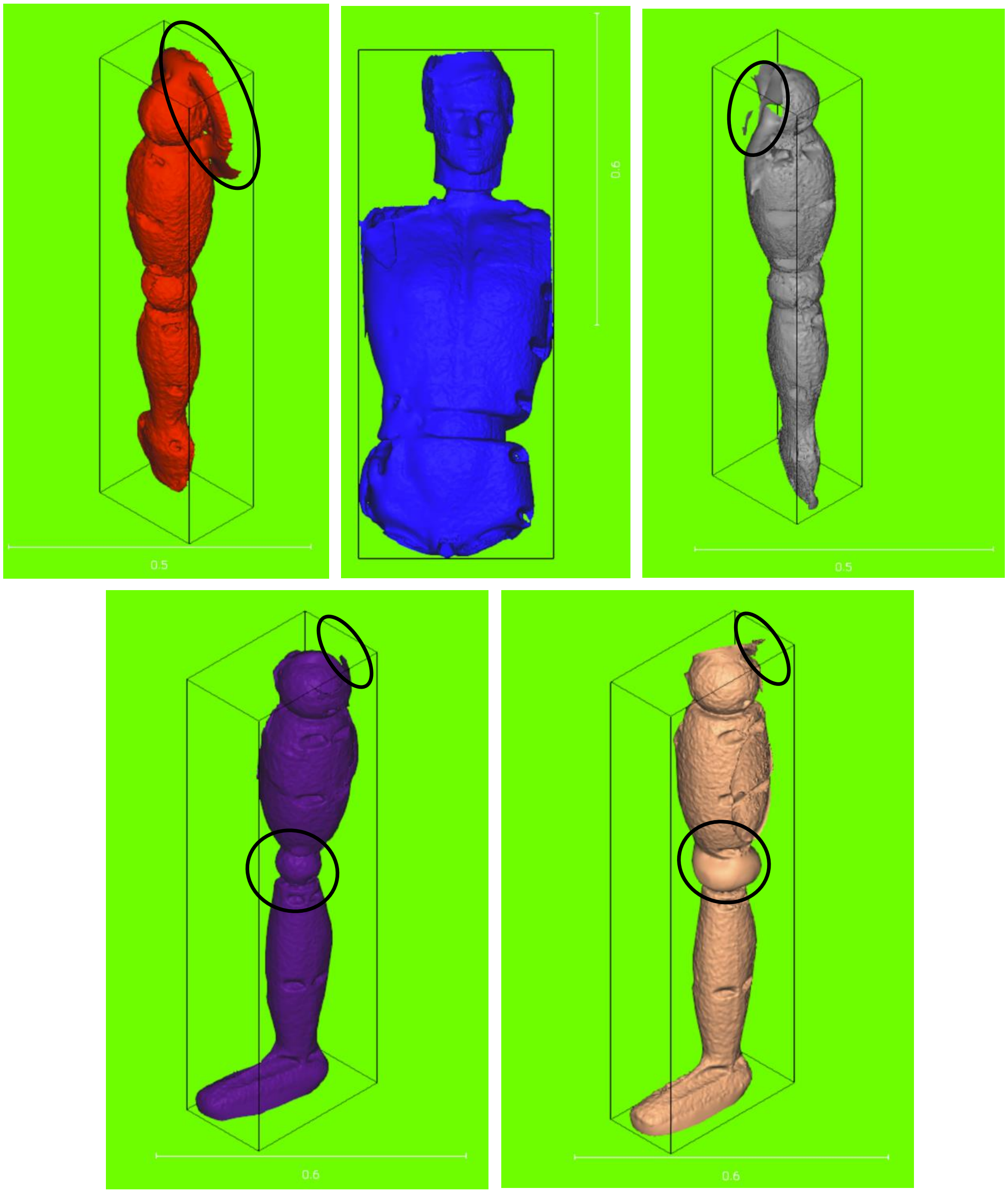

Figure 30 - The five segments of the model with the scale in meters (top left :right arm, top middle: torso and head, top right : left arm, bottom left : right leg, bottom right : left leg), and some of their imperfection circle in black

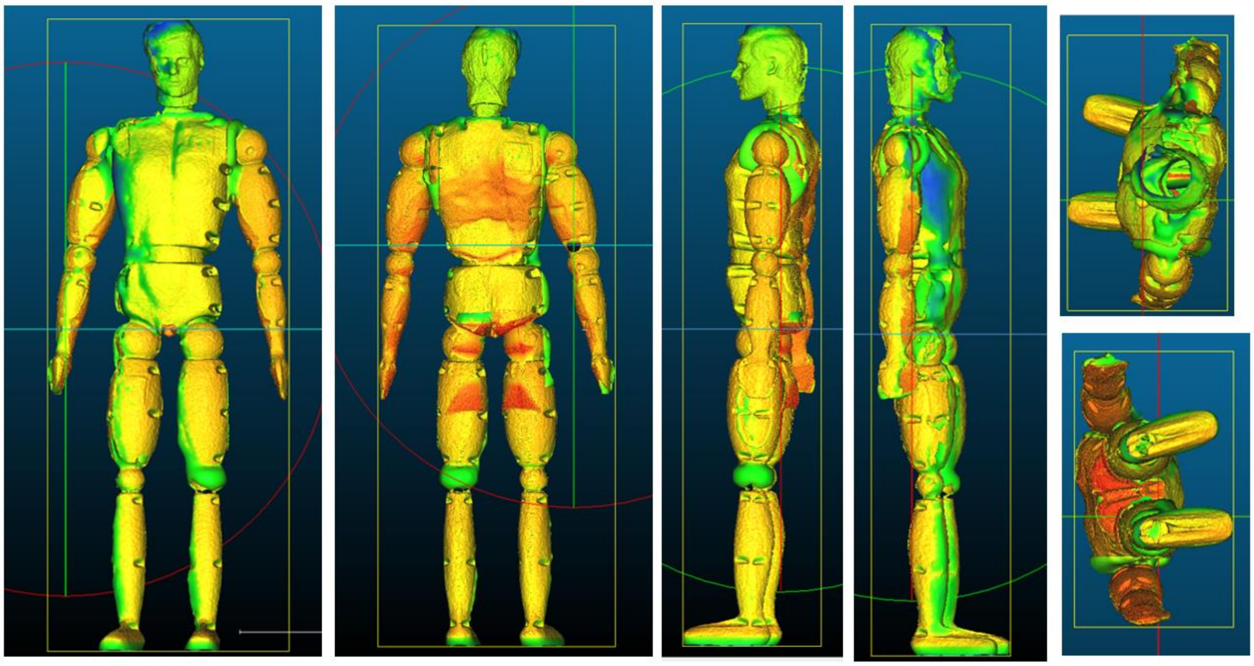

Figure 31 - Final modeling of Ken

The resulting mesh is not continuous and has holes in it. Using different software such as meshlab or blender, different techniques are used to try to fill the holes in the mesh but none of them work. Indeed, using the *hole filling* parameters leads to a model with a few filled holes inside of the model and this significantly increases the mesh surface of the model (Figure 32). Another method is to fill the hole manually using blender but this does not work because even when the macroscopic holes are filled, it seems that the mesh is still open (Figure 33).

The 3D modeling made with Cloud Compare is used to calculate the projected surface area of the model, using Matlab.

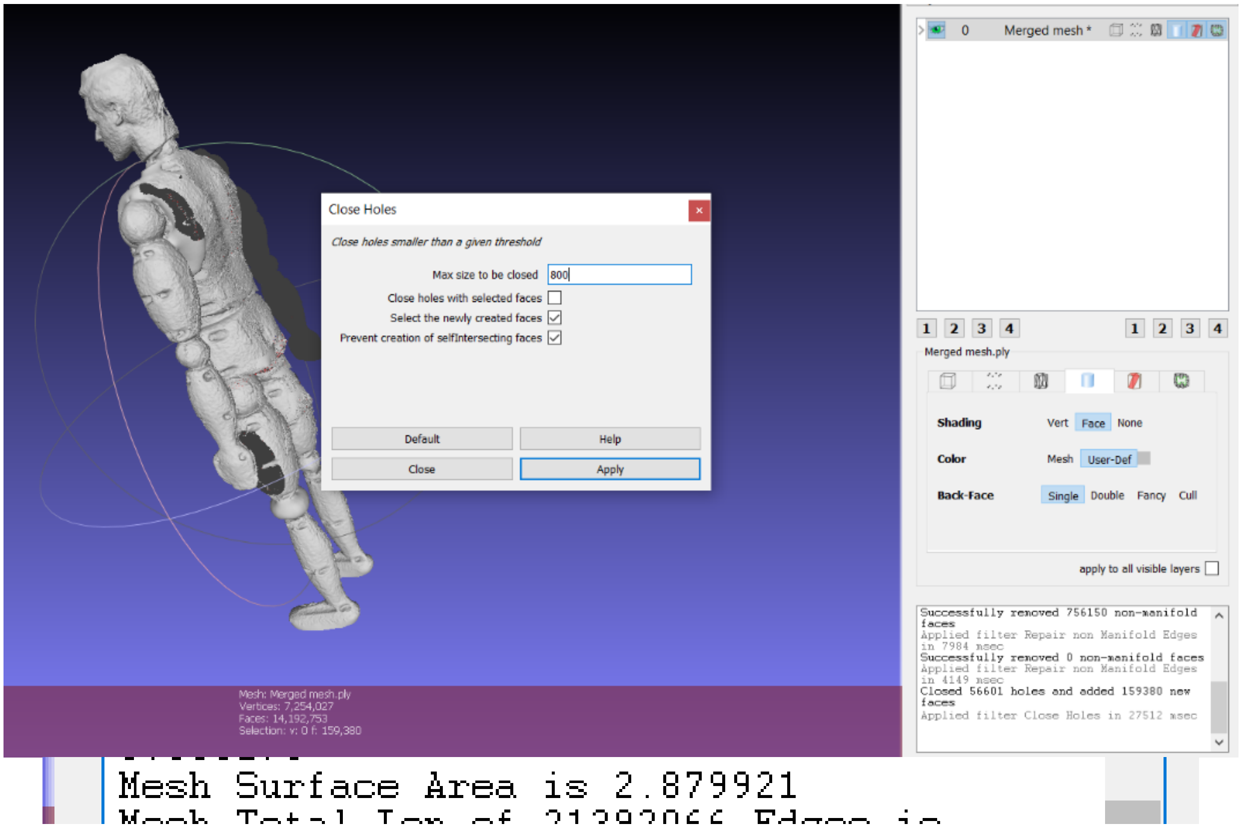

Close Holes

Close holes smaller than a given threshold

Max size to be closed: 800
☐ Close holes with selected faces
☑ Select the newly created faces
☑ Prevent creation of selfIntersecting faces

Shading: Vert [✓ Face] None
Color: Mesh [✓ User-Def]
Back-Face: [✓ Single] Double Fancy Cull
☐ apply to all visible layers

```
Successfully removed 756150 non-manifold
faces
Applied filter Repair non Manifold Edges
in 7984 msec
Successfully removed 0 non-manifold faces
Applied filter Repair non Manifold Edges
in 4149 msec
Closed 56601 holes and added 159380 new
faces
Applied filter Close Holes in 27512 msec
```

```
Mesh: Merged mesh.ply
Vertices: 7,254,027
Faces: 14,192,753
Selection: v: 0 f: 159,380
```

```
Mesh Surface Area is 2.879921
```

Figure 32 - Closing holes on meshlab and the surface area obtain in mm^2 using this method

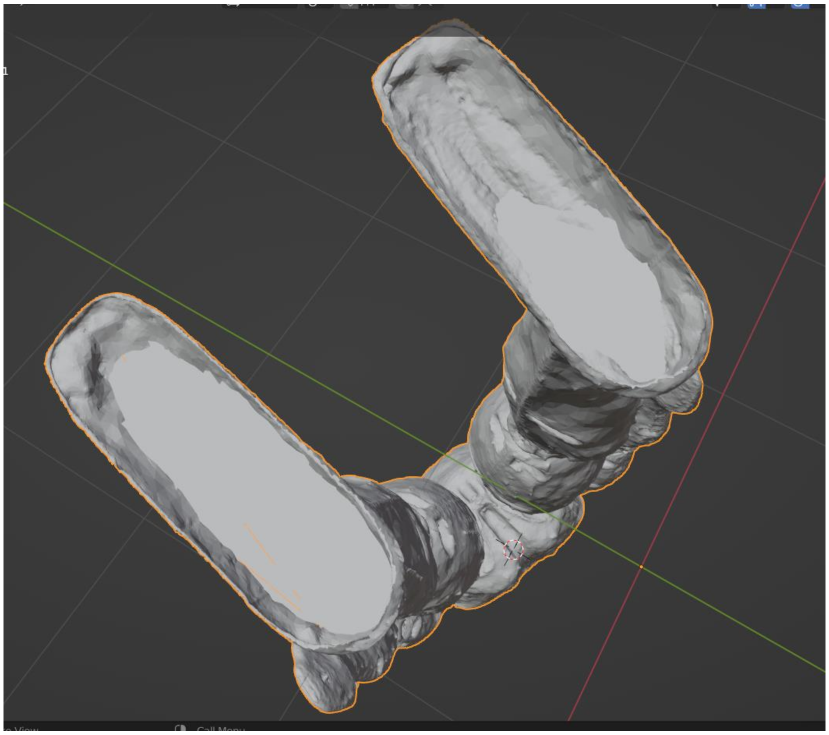

Figure 33 - Filling holes using blender

3.2. Analysis of the data collected

3.2.1. Total projected surface

In order to obtain the projected surfaces in all directions and in all positions detailed in Figure 3, Figure 15 and Figure 16, a Matlab code is used (modified from Tayeb, 2013). This code analyzes the RGB colors of a screenshot taken in the desired positions and provides the number of pixels of each color. To do this, it is necessary to impose colors on each part of the body that is to be analyzed (Figure 34), and a scale of known dimension (Figure 35) is used so that the number of pixels can be transformed into cubic meters.

Figure 34 - Picture of the colors used to calculate the projected surfaces (respectively named left arm in red, torso in blue, right arm in grey, left leg in purple and right leg in orange) for the configuration 1

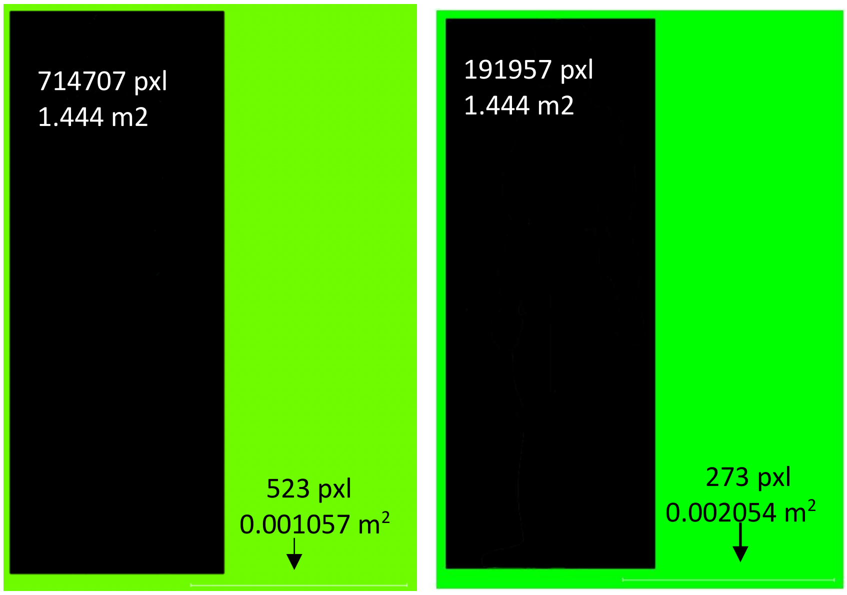

Figure 35 - Scale of screen captures for two different screens (black box of know dimension and white scale of unknown dimension)

It is important to notice that this scale varies according to the quality of the screen capture and can change from one computer to another, so it must be calibrated in consequence. With this in mind, the size of a single pixel in the results that are given in this chapter can vary from 2.0207E-06 m^2 and 7.5236E-06 m^2.

The projected surface area is obtained for the configuration 1 along the *y* and *x-axis* (Figure 36 and Figure 37) for comparison with the literature. Their values are available in the Appendix (Table 13, Table 14, Table 15 and Table 17). The angle is chosen starting from 0 degree, but the model does not have perfectly straight limbs, which can lead to a slight variation in the projected area, especially when comparing the different limbs and especially in some positions where the limbs should be perfectly aligned.

In the paper by Morais et al. (2020), which works on the frontal surface area of swimmers, for a swimmer's position of "right upper-limb exit and left upper-limb catch" or whose "left upper-limb exit and right upper-limb catch" (Figure 38), frontal surface area measurements are computed using digital photogrammetry. These positions approximate the 0° position of our dummy when rotated along the *x-axis* (Figure 37). Morais et al. (2020) measurements are made on 17 adolescent swimmers with an average height of 1m73 for an average weight of 66.62 kg. For these two positions, the averages surface area is 0.0806 +/- 0.012 m^2 and 0.0825 m^2 while for Ken, this value is 0.1577 m^2. This difference between the values obtained for the dummy and those obtained for the swimmers can be explained by the larger size of the dummy's body, especially at the shoulder, and the difference in the position of the arms alignment of the dummy. It is logical that the model has a larger frontal surface area. If we compare with the article of Gatta et al. (2015), who work on male swimmer with an average height of 1m82 for an average weight of 78.9 kg for a "streamlined leg kicking condition" position, the frontal area that is calculated using a planimetric method is 0.15 +/- 0.01 m^2 while for the equation used by Clarys (1979), this value is 0.08 +/- 0.01 m^2 and for the equation used by Mollendorf et al. (2004), this value is 0.21 +/- 0.03 m^2. The value obtained by the planimetric method is very close to the value of 0.1577 m^2 obtained with Ken. This can be explained by the fact that the measurement is made on swimmers who have physical characteristics closer to those of the model. But for the three methods mentioned, the difference in results is significant.

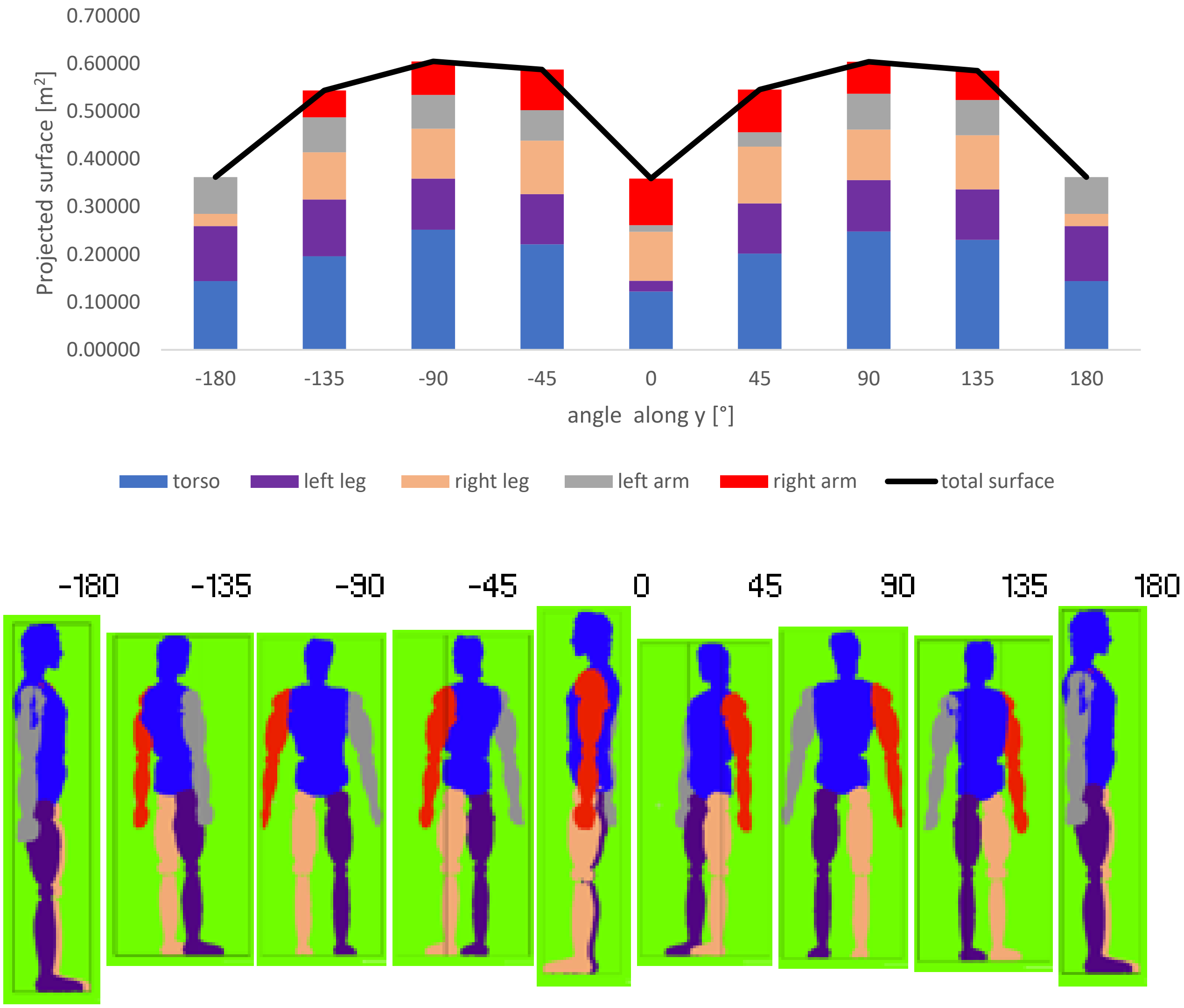

Figure 36 - Graphic of the projected surface for configuration 1 with rotation along the y-axis and their corresponding positions

The surface area is minimal with an angle of -180°, 0° and 180° along *x-axis* but also along the *x-axis* and the maximum surface area with an angle of -90 and 90° along *y and x-axis* which is consistent given the surface area of the body visible in Figure 36 and Figure 37.

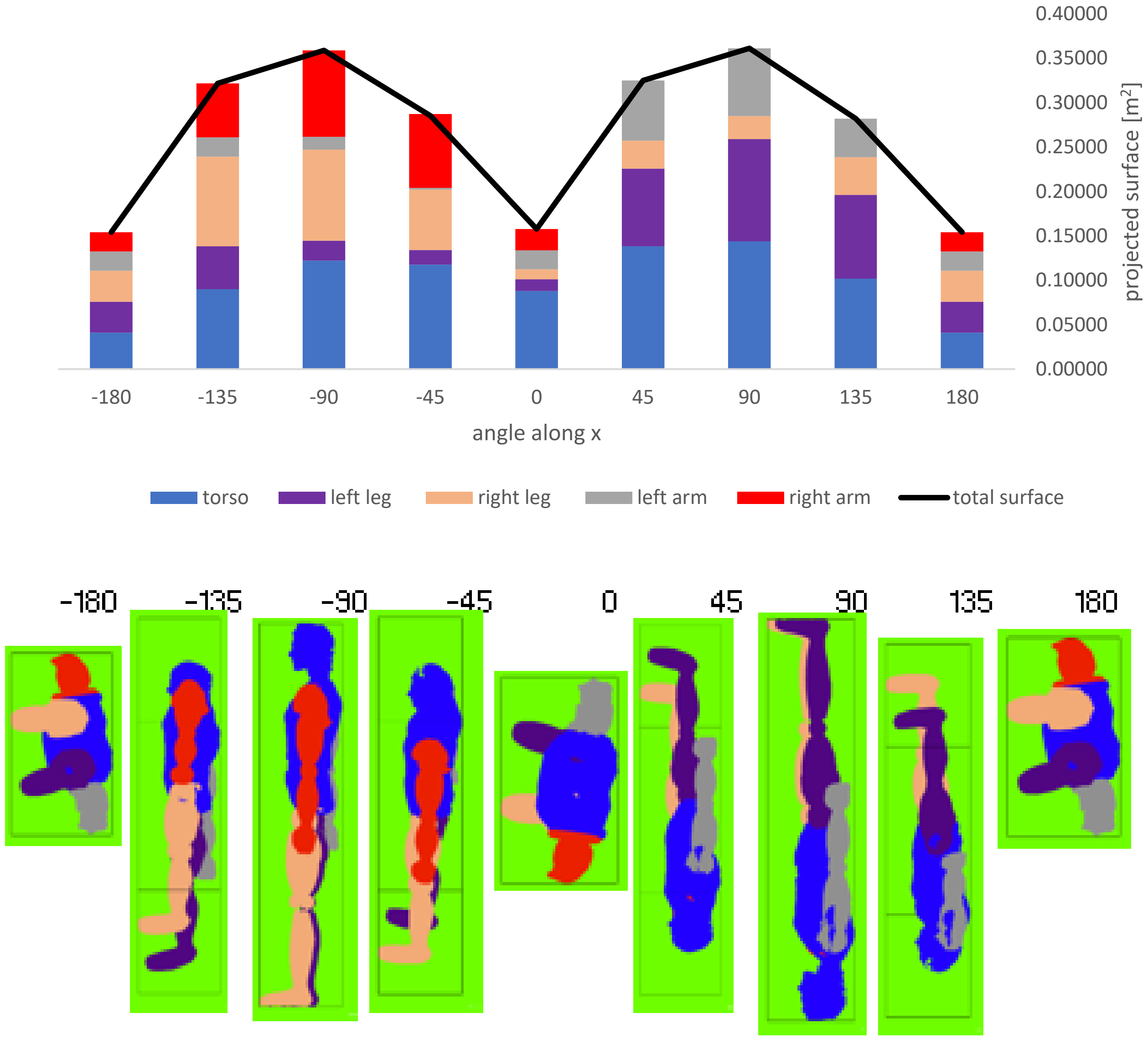

Figure 37 - Graphic of the projected surface for configuration 1 with rotation along the x-axis and their corresponding positions

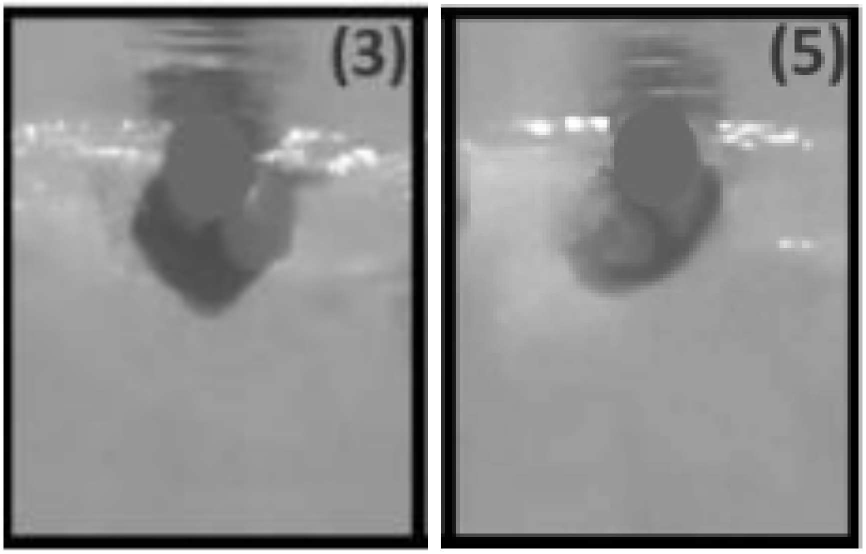

Figure 38 - Position of the swimmer (Morais et al., 2020) (3) : right upper-limb exit and left upper-limb catch and (5) left upper-limb exit and right upper-limb catch

The projected surface area is then obtained for configuration 2 (Figure 39) and configuration 3 (Figure 40 and Figure 41) along the *x-axis*. Their values are available in the Appendix (Table 18, Table 19, Table 21 and Table 22). For configuration 3 (angle of the torso: 90° from the horizontal), an angle of 90 degrees is chosen between the torso and the legs because if some experiments are to be carried out in the wind tunnel, this is the position most likely to be applied.

The configuration 3 for a 90° rotation angle along the x-axis can be compared with the position of some cyclists to see if the value can be trusted. Heil (2002) took photographs of 21 male racing cyclists (average height 1.82m and average weight 74.4 kg) which are digitized by hand using Scion Image Beta 4.02 software. The traditional acro-position" and the "drops position" (Figure 42) can be compared to configuration 3. It is important to note that the A_p of the cyclists included their helmet and clothes. For the traditional acro-position, the A_p is equal to 0.342 m^2 and for the drops position, the A_p is equal to 0.414 m^2. In comparison, the deduced A_p for Ken is equal to 0.547 m^2. Once again, the stature of the model can explain this difference in results. In addition, the legs and arms of the model are unfolded in contrast to the cyclist position. If for the arm and legs, only 2/3 of the surface are taken into account in our results, the surface area will be of 0.4017 m^2 which is relatively close to the results of Heil (2002).

In the article of Bonamy (2021), 14 cyclists (average height of 1m77 for an average weight of 74.8 kg) are digitized for three different positions (Figure 43). The A_p is 0.433 m^2 for position 1, 0.413 m2 for position 2 and 0.387 m^2 for position 3. The A_p is still 0.547 for Ken and still larger. This time, the A_p for the different positions take into account the bicycle, but the cyclists are smaller (with 13 cm of difference with Ken). Furthermore, in the article by Debraux et al. (2009), for the same position 1 as Bonamy and using digital photography, the A_p is equal to 0.533 m^2 which is very close to the results obtained for Ken. Using *CAD* (Computated-Aided Design) Debraux et al. obtain an A_p of 0.565 m^2.

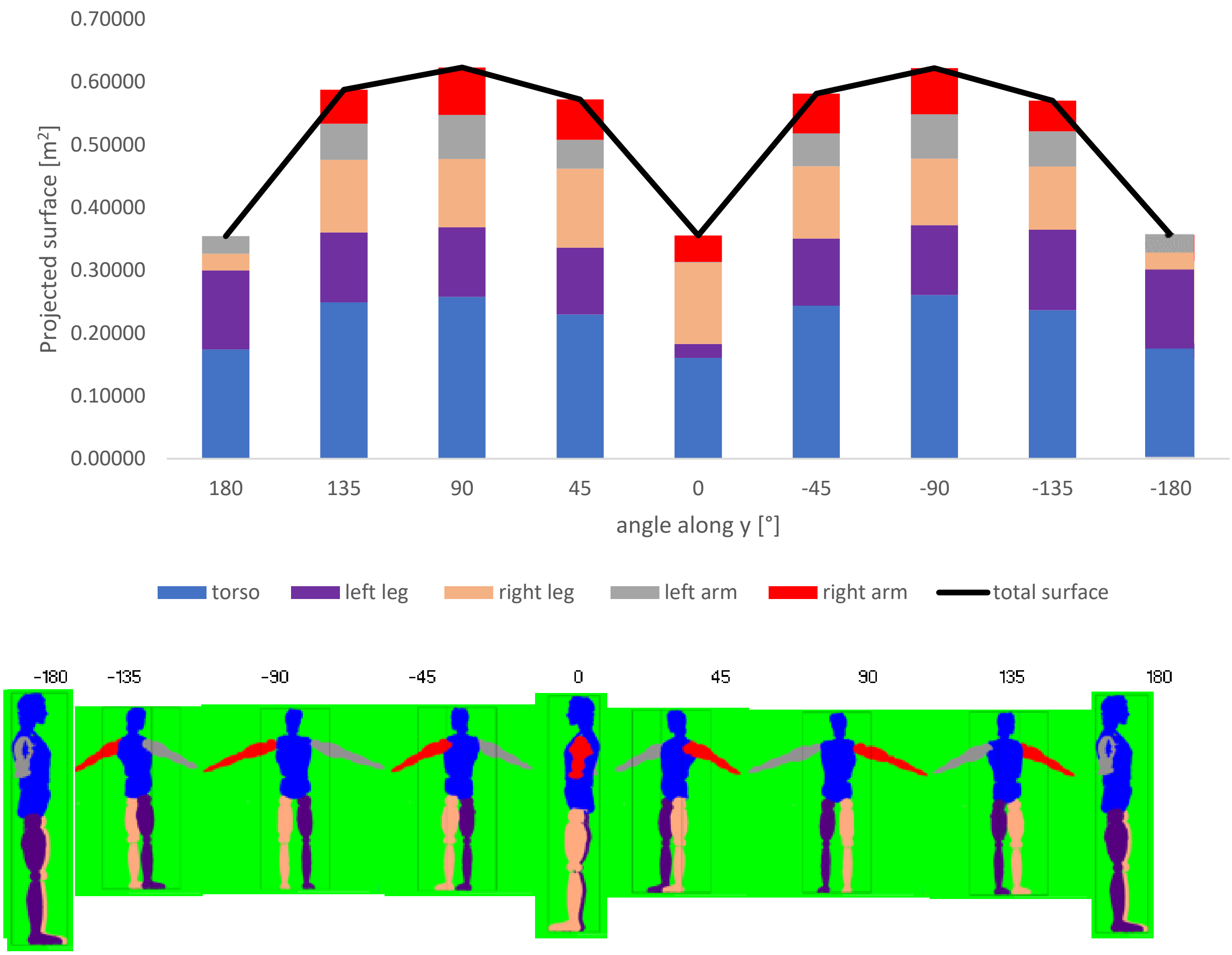

Figure 39 - Graphic of the projected surface for configuration 2 with rotation along the y-axis and their corresponding positions

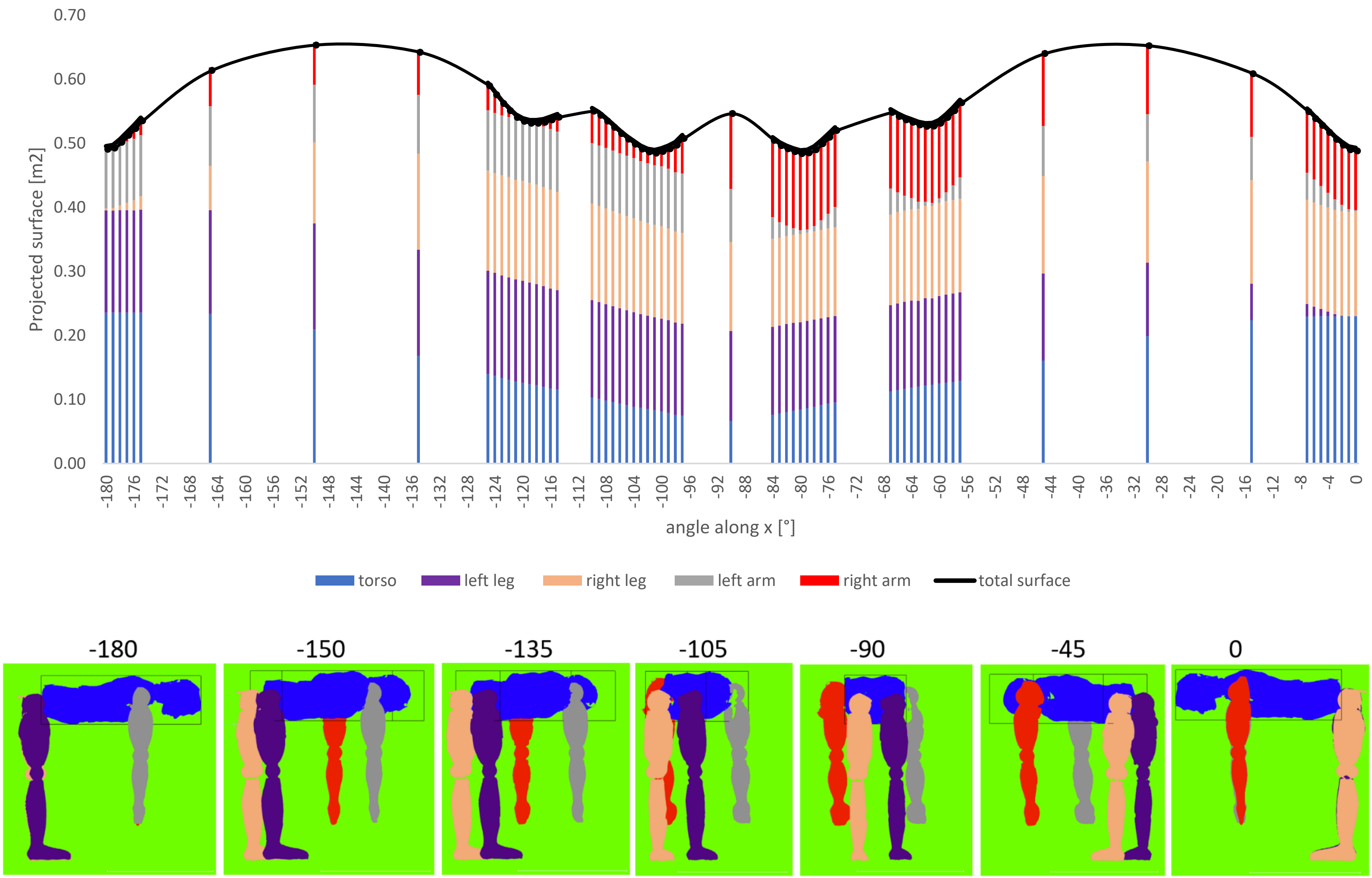

Figure 40 - Graphic of the projected surface configuration 3 (angle of the torso: 90° from the horizontal) with rotation along the y-axis and some of their corresponding positions

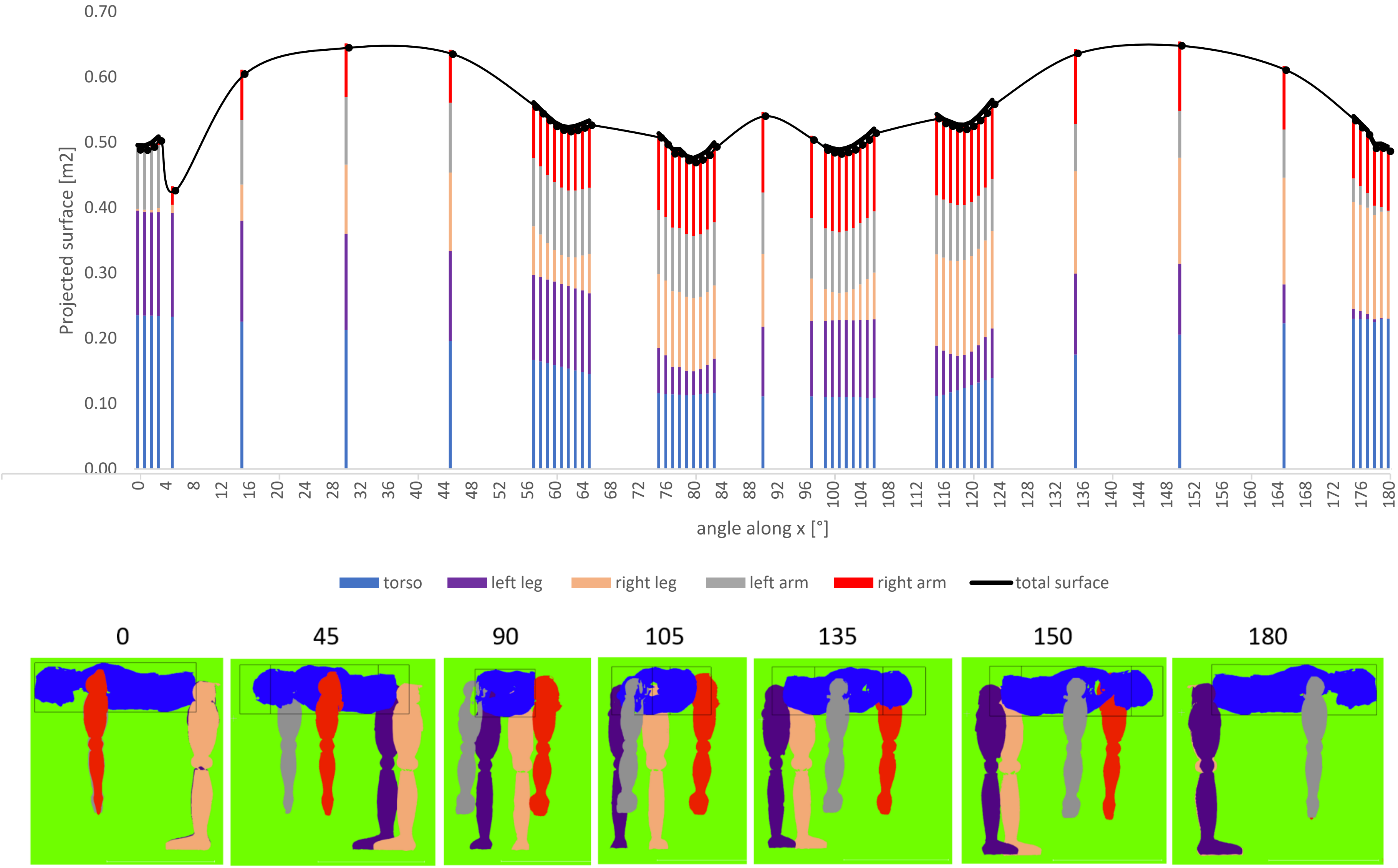

Figure 41 - Graphic of the projected surface for configuration 3 (angle of the torso: 90° from the horizontal)with rotation along the y-axis and some of their corresponding positions

Figure 42 - Left : cyclist drops position, Right : cyclist traditional acro-position (Heil, 2002)

Figure 43 - 3 positions of a cyclists (respectively P1 to P3) with difference in hand and elbow positioning (Bonamy, 2021)

3.2.2. Body part projected surface

For configuration 1 with rotation along the *x-axis* (Figure 44), the results for positive and negative angles are almost the same. At 180 degrees, the right arm is not taken into account which is logical since it is hidden by the torso of the model. Normally, at 0 degree, the same should be true for the left arm but it is not quite the case because the model is not perfectly aligned and straight. This error must be taken into account when the calculated projected surface is used in other calculations. This error is particularly noticeable for angles of -165 and 165 degree or -15 and 15 degrees, with a major difference in the projected area. Some mesh errors resulting in holes may also play a role in these differences.

Configuration 1 with rotation along the *x-axis* (Figure 45) confirms this error, with for example the left arm present at -90 degrees when it should not be. Apart from this, the various values obtained seem consistent, with projected area values that can be used for the calculations that will be made later.

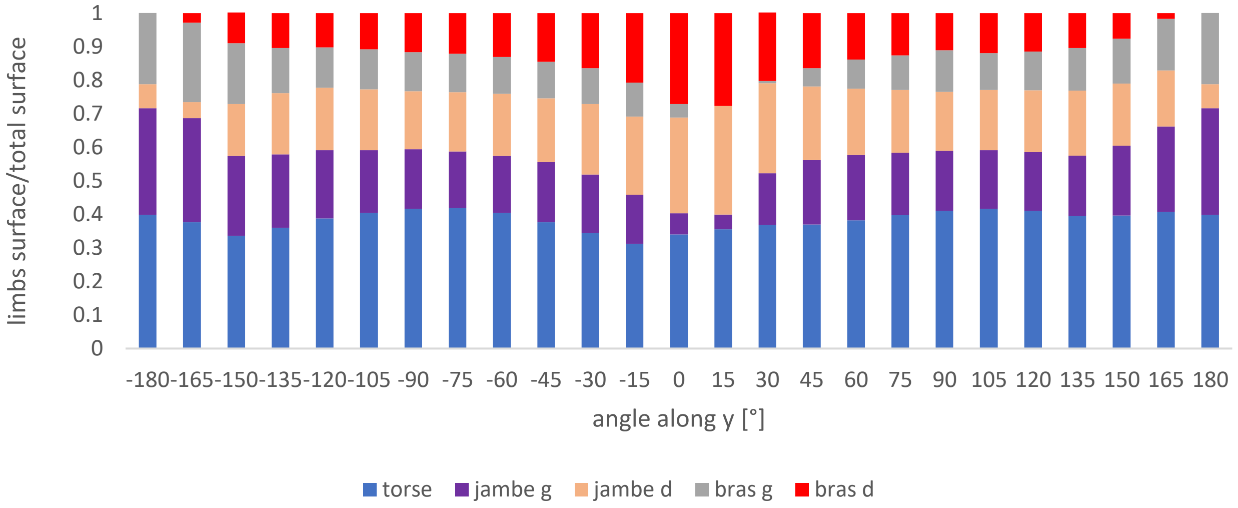

Figure 44 - Graphic of the projected surface for each part of the body for configuration 1 with rotation along the x-axis

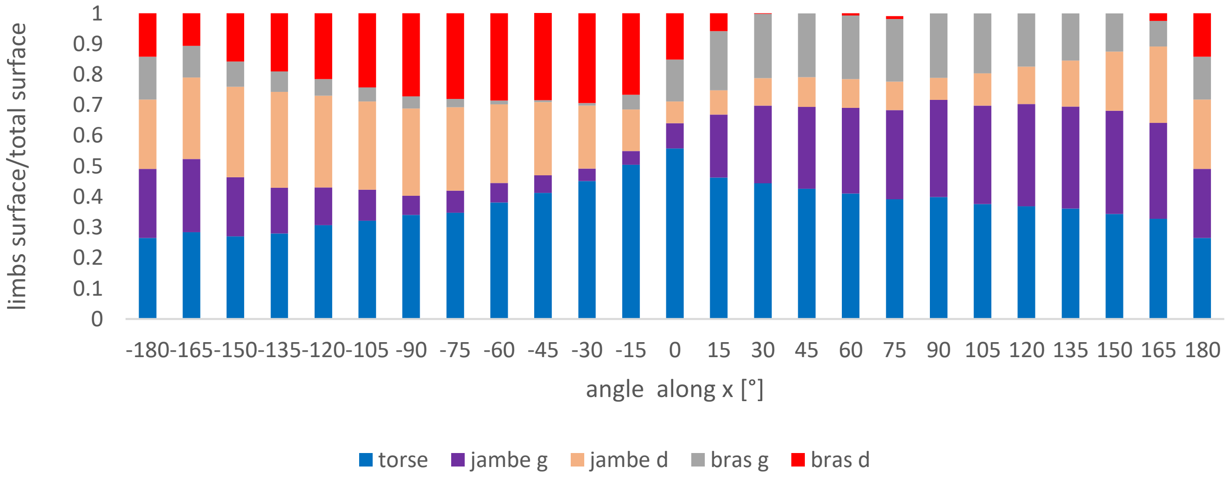

Figure 45 - Graphic of the projected surface for each part of the body for configuration 1 with rotation along the x-axis

For configuration 2 with rotation along the *x-axis* (Figure 46), once again, the results for positive and negative angles are almost the same. For this position, the main difference is between -15 and 15 degrees, where the left arm and the left leg are not similar. This is again due to the fact that the model is not perfectly upright in its limbs and this leads to a slight difference in the results.

For this same configuration, with a rotation along the *x-axis* (Figure 47), the right arm appears to be almost hidden between 60 and 135 degrees and the left arm appears to be more hidden between -105 and -60 degrees which corroborates the fact that the limbs are not all aligned with each other.

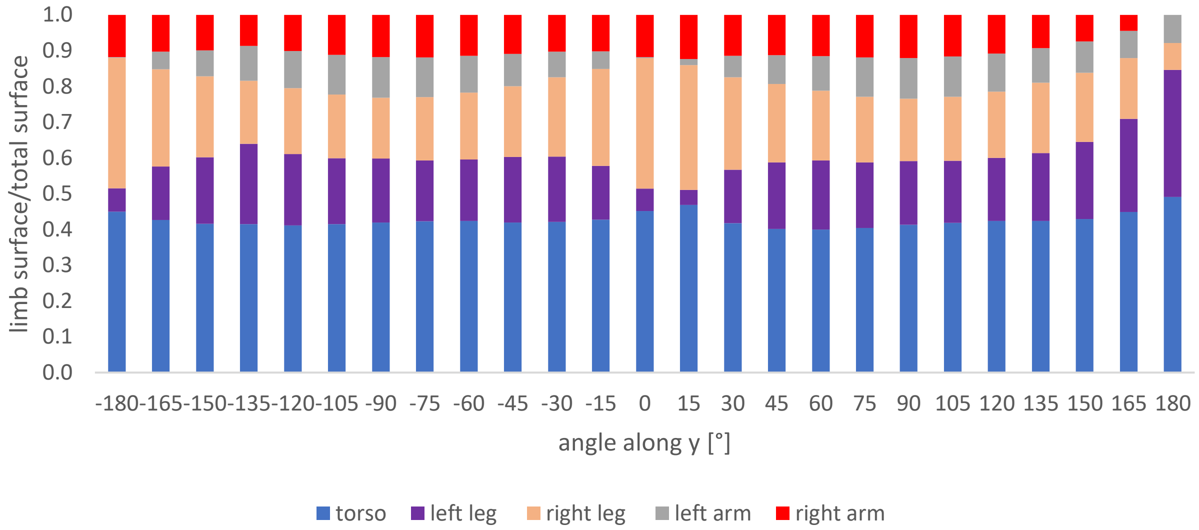

Figure 46 - Graphic of the projected surface for each part of the body for configuration 2 with rotation along the x-axis

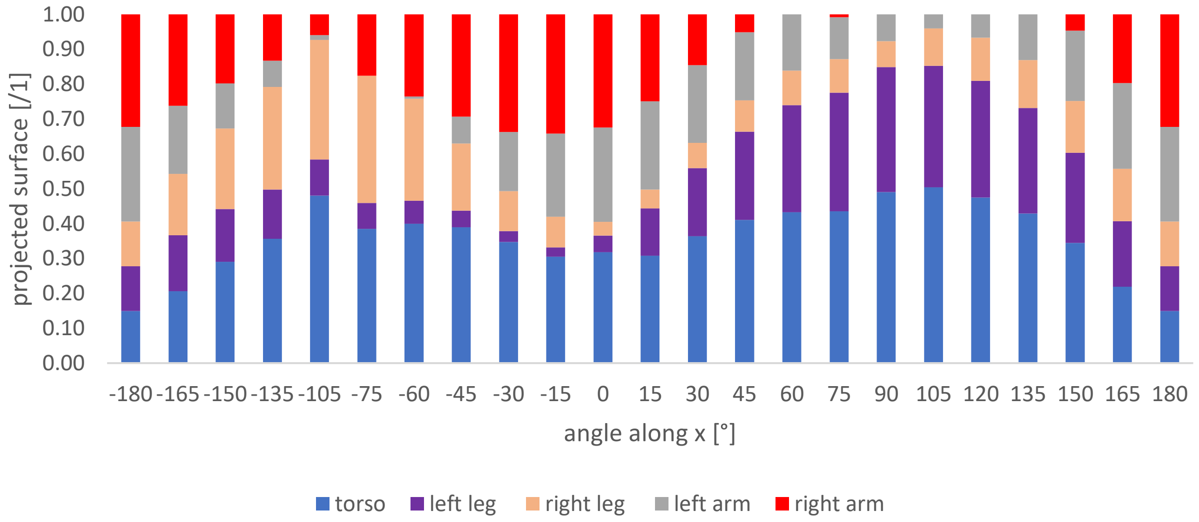

Figure 47 - Graphic of the projected surface for each part of the body for configuration 2 with rotation along the x-axis

For configuration 3 with rotation along the *x-axis* (Figure 50), more results are obtained for a larger number of angles in order to analyze this position in detail as it is the preferential position of a drowning person. More detailed results are obtained in particular for positions where some body parts are hidden (arms or legs).

The positive angle for which the torso surface is the greatest is 180 degrees but for the negative angle, it is -176 degrees with a surface of 0.235 and 0.236 m^2 respectively. And the positive angle for which the torso surface is minimum is 74 degrees and for the negative angle it is -90 degrees with a surface of 0.109 and 0.066 m^2. It is important to emphasize that in contrast to the value obtained for the minimum torso surface, here the measurements are very different. This is because the angle is also very different. If compared with the angle of -75 degrees with a surface of 0.0951, the value of 0.109 already seems a little more similar. But this difference is due to the fact that there is the presence of the arm or legs which are located in front of the chest which can hide part of it (Figure 48), playing on its total visible surface. As mentioned earlier, errors in the mesh result in holes which can also play a part in these differences.

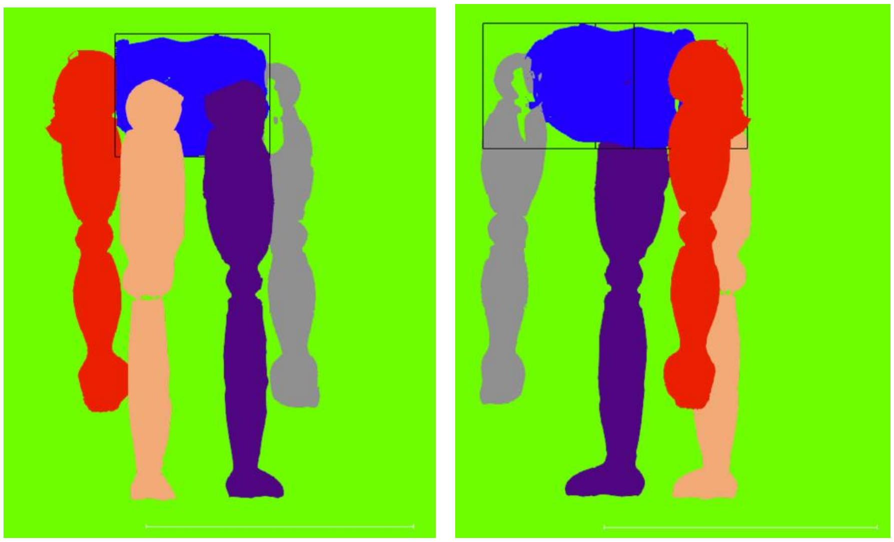

Figure 48 -Position of the body in configuration 3 for the angle of -90 (on the right) and 74 (on the left) with rotation along the x-axis

For the left arm, the maximum surface area obtained is for a rotation of 135 degrees for a positive angle and -180 degrees for a negative angle with surfaces of 0.107 and 0.097 m^2. And the minimum surface area is of 0 degrees with 0.002 m^2. The 135 degrees angle has the maximum surface area because it is the area where the arms are most visible in their entirety but also and especially because the hand is presented flat, with its maximum surface where at 180 degrees, the hand is sideways (Figure 49).

For the left leg, the maximum surface area is this time obtained for a rotation of -135 degrees or for 180 degrees with 0.166 and 0.160 m^2. It is logical to obtain the same angle as before with opposite signs since these positions emphasize the legs more than the arms.

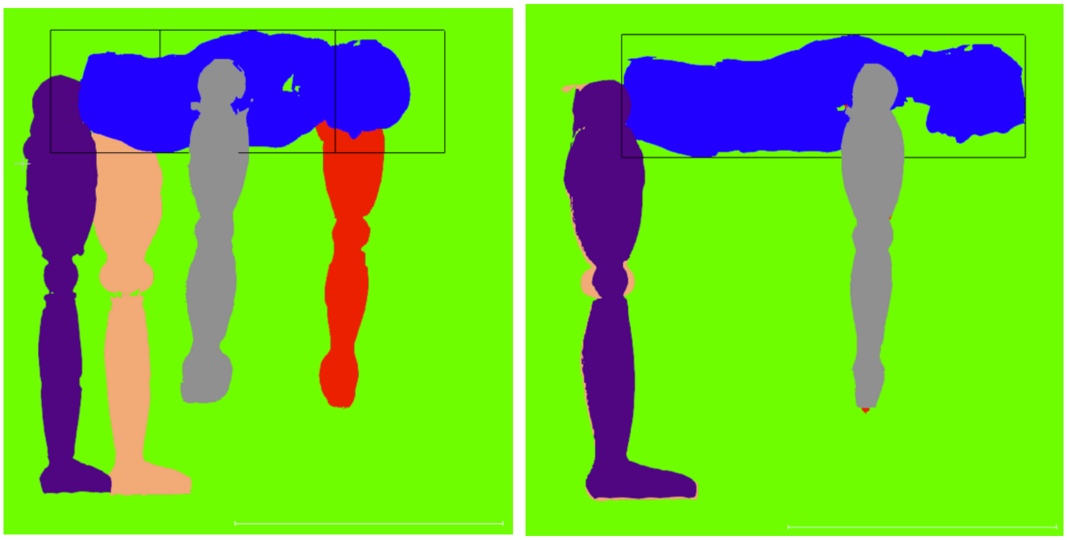

Figure 49 - Position of the body in configuration 3 for the angle of 135 (on the right) and -180 (on the left) with rotation along the x-axis

For the right arm, the maximum surface area is 0.127 m^2 for a positive angle of 77 degrees and 0.125 m^2 for a negative angle of -81 degrees. The difference of angles between those two absolute values is only due to the torsion of the right arm. And the minimum surface area is 0 m^2 for 180 and -180 degrees. For the left leg, the maximum surface area is 0.1636 m^2 for 5 degrees and not 0 degree and confirms once again that not all limbs are perfectly straightforward. The minimum surface area is 0.003 for a positive angle of 179 and 0.003 for a negative angle of -180 degrees.

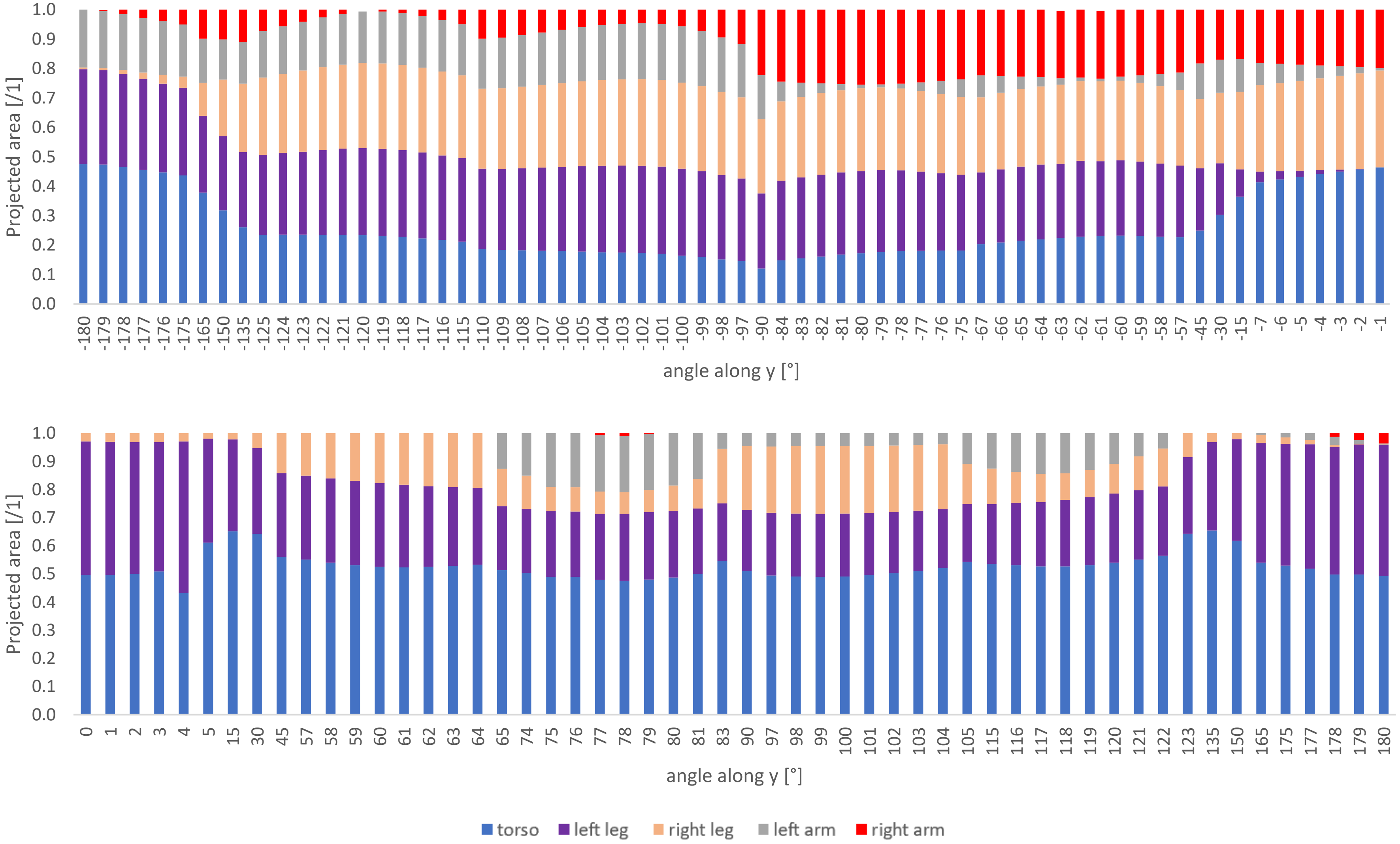

Figure 50 - Graphic of the projected surface for each part of the body for configuration 3 (angle of the torso: 90° from the horizontal) with rotation along the x-axis

3.2.3. Comparison of projected area to other methods

Other acquisitions are carried out to obtain the projected surface area of the model.

Indeed, a second photogrammetric acquisition (Figure 51) is carried out because the first photogrammetric acquisition is not of good quality because of the texture of the model which causes reflections that were too important to be exploited numerically. To counter the effect of reflections on the photos, three flashes are added to the camera (Nikon Z6), plus the camera is also equipped with a polarizing cash.

These results can be modelled via Reality Capture but this time using the least squares method, cleaned up via Cloud Compare using the slicing tool and analyzed via Matlab as it was realised previously with the laser scan results (Figure 53 and Figure 55). These results can be compared to those obtained previously (Figure 52 and Figure 54).

Figure 51 - Data acquisition of the model using a three flashes camera with polarizer

Along the *x-axis* (Figure 52), the results are quite similar to what was obtained previously with a larger difference for the 90 degrees angle. This difference can be explained by the fact that the alignment of the dummy for this photogrammetry is not exactly the same as for the laser scans acquisitions.

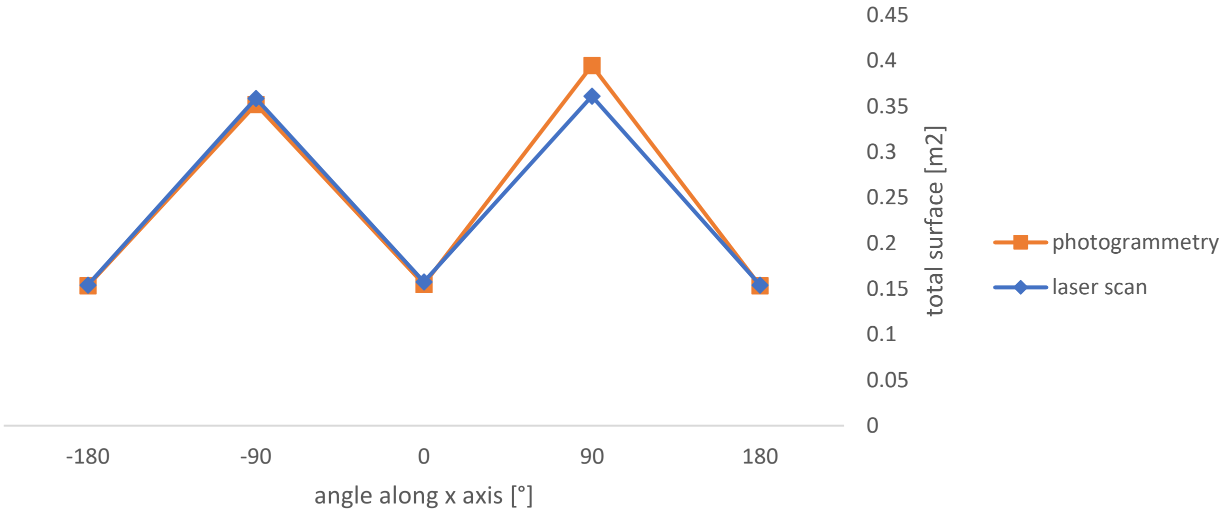

Figure 52 - Comparison between total surface for the model based on laser scan and photogrammetry along x-axis for configuration 1

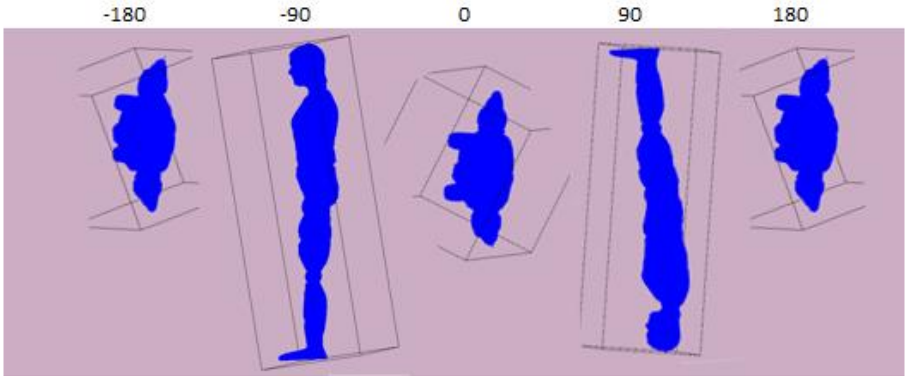

Figure 53 - Position of the model based on photogrammetry with rotation along x-axis

Along *x-axis* (Figure 54), the photogrammetry results are generally overestimated compared to those obtained by laser scanning due to the same inaccuracy as highlighted for the *x-axis*. Once again, the 90 degrees estimation is particularly impacted which tends to confirm that this difference is related to the alignment of the dummy. The photogrammetry is known to give less accurate results than laser scanning, resulting in a less accurate model. The modelling method is not the same and the method (*Poisson surface reconstruction*) used for the laser scanning results is also more precise due to the complex shape of the model.

The results obtained with photogrammetry generally corroborate those obtained with the laser scan with an error due the precision of the results.

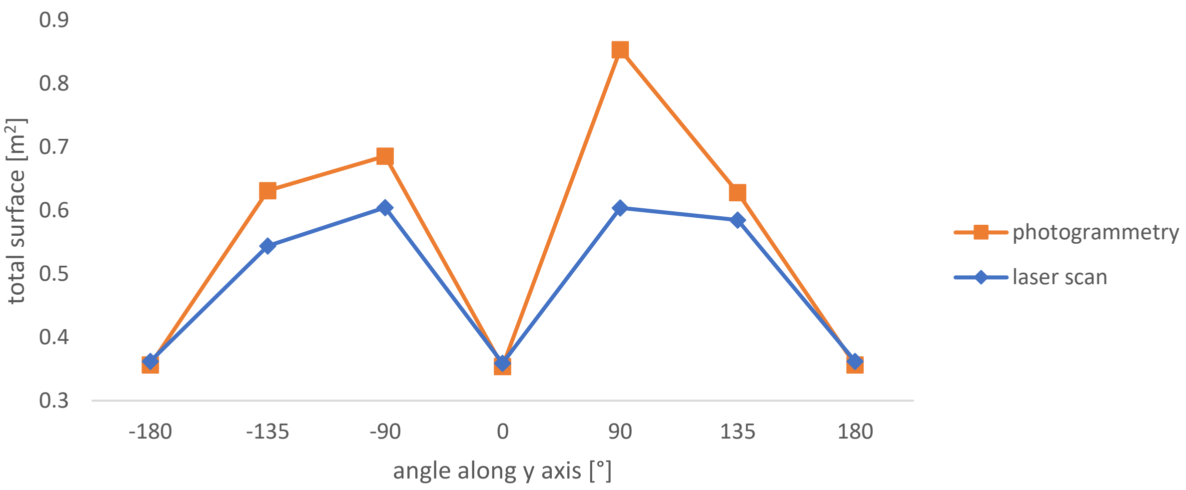

Figure 54 - Comparison between total surface for the model based on laser scan and photogrammetry along x-axis for configuration 1

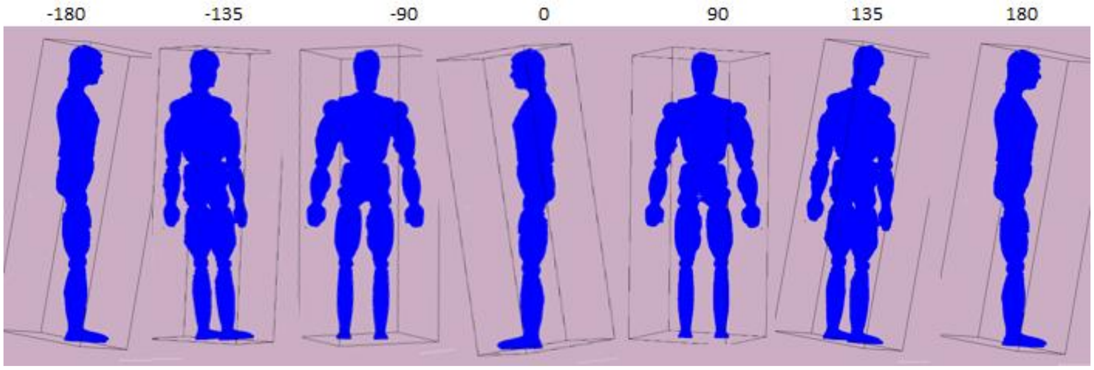

Figure 55 - Position of the model based on photogrammetry with rotation along x-axis

Another acquisition is carried out in partnership with Zakaria Boualem. The method is more or less similar to that of photogrammetry method, this time with pictures taken from three different locations and using a black and white squares background as well as landmarks (Figure 56). Zakaria then constructs an algorithm that will be used to perform the direct linear transformation (DLT) of the model with calibration points.

This acquisition is achieved for the model in configuration 3 with a leaning model ((angle of the torso: +/- 30° from the horizontal for DLT and +/-45° from the horizontal for scanning laser) so that it is compared to a model adjust in Cloud Compare with this same characteristic (Figure 58) which varies from the configuration 3 described in Section 3.2.2. The value obtained with this method are underestimated compared to those obtained with the laser scan. This is consistent since the method is again less accurate than the laser scanning method. This may be due to the number of calibration points or their position in space when configurating the algorithm. The values for positions of 90 and 45 degrees are particularly different, which can be explained by the fact that for these values, the position of the dummy's head or limbs is not perfectly identical in the two methods. The degree of inclination of the torso also varies and is probably the major cause of these differences. Indeed, for an angle of 0 degree along the *x-axis*, the value obtained with the two methods are much closer and this orientation does not take into account the inclination of the torso as much as the tree other.

Figure 56 - Data acquisition for the direct linear transformation

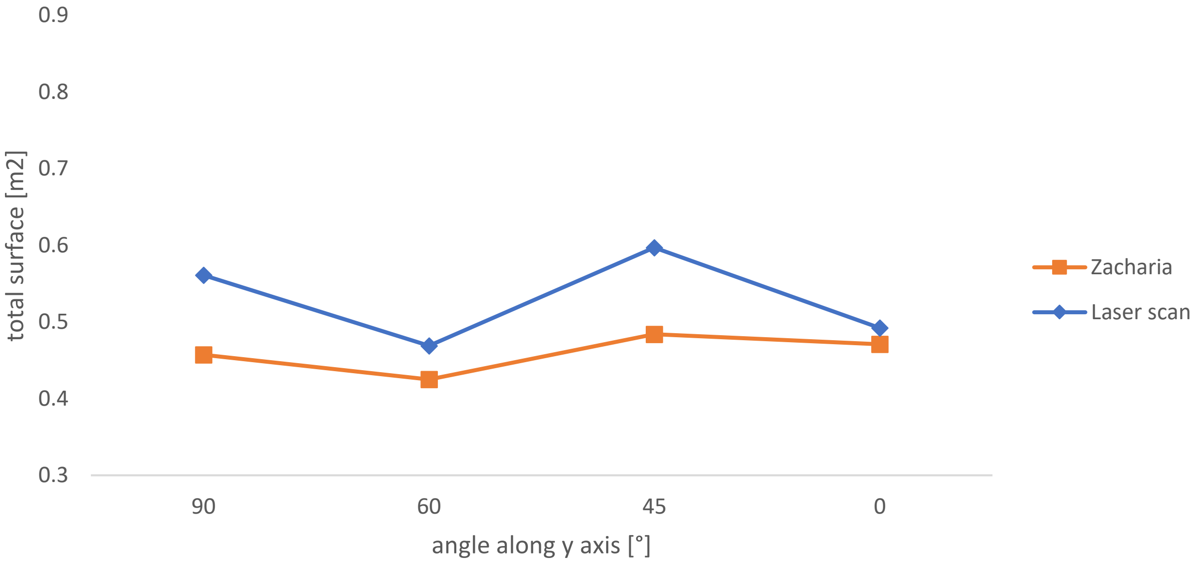

Figure 57 - Comparison between total surface for the model based on laser scan and Zacharia along x-axis for configuration 3 but with the leaning torso

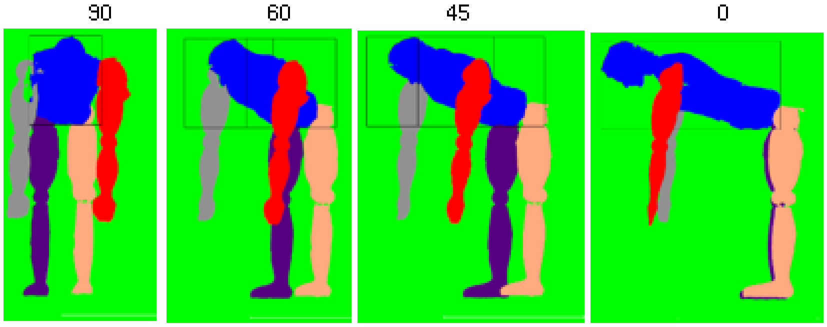

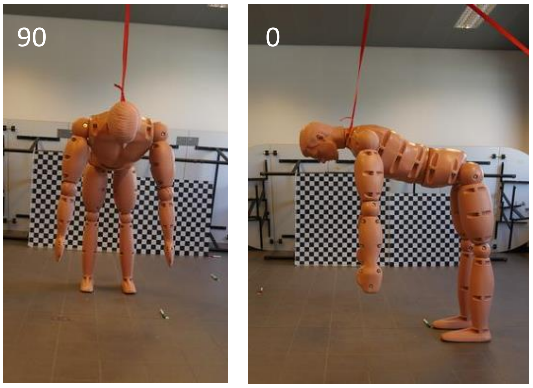

Figure 58 - Position of the model along x-axis with the laser scan model and with the direct linear transformation (Zacharia) for configuration 3 with leaning torso

3.2.4. Total surface area

The software total surface measurement tool gives an estimated mesh surface of 3.006 m^2 and a volume measurement of 0.05319 m^3, both of which are highly unlikely. Indeed, the surface of the mesh is estimated to be 3.006 m^2 but Cloud Compare must have taken into account the surfaces located in the holes (like the one located on the head of the dummy for example). And the volume is estimated to be 0.05319 m^3 but a clear message is given by the program to warn that the mesh has holes, which confirms that these values are not reliable.

Obtaining the exact total surface of the model via numerical methods is not possible. Indeed, many different software packages are used to try to obtain a result: Reality Capture, Cloud Compare, Meshlab or Blender but none of them is fairly accurate or handy enough to obtain a mesh without holes or without meshes forming inside the shape of the model.

Whether the method with laser scan or photogrammetry is used, the result remains the same and total surface area cannot be obtained despite all the tools available.

Cloud Compare, Meshlab and Blender share a tool named *hole filling* which is supposed to fill the holes in the mesh and help achieve a smooth and continuous mesh. But this tool does not work well, as it adds meshes inside the main mesh increasing the total area of the mesh considerably (sometimes with values that could go to 33 m^2!). Another option is to fill the holes manually using Blender (Figure 33, Figure 59) but some holes are too small to be found and even using this method, it is impossible to obtain a continuous mesh.

An approximate total surface area can be deduced using the projected area for a rotation along *the y-axis* of -180, -90, 0 and 90 degrees and the projected area for a rotation along the *x-axis* of 0 and 180 degrees given with the laser method. This gives a total surface area of 2.241 m^2. When calculating the total area with other software, this value should not be exceeded. But in all the other techniques used, this value was always exceeded!

A comparison with a home-made photogrammetry on a cardboard had to be made in order to understand the tools available on Cloud Compare or MeshLab and how the total surface area could be realised by the software on an object of known dimension. But despite the use of a high contrast between the cardboard and the ground, two types of different cardboard and a large number of photos, it was not enough to obtain a dense and coherent point cloud to model it in 3D, so an object available in a database (Artec3D) is finally used: a screw.

If compared with the mesh of a screw (Figure 60), the difference between the value of the total surface of the screw calculated by the software (this object having no holes or over-mesh) and the value of total surface obtained with the projected areas (as it was done previously for Ken) can be obtained. The total surface area of the mesh is 148.237 mm2 and the total surface of the screw obtained using the method with its six sides of projected areas is 163.8872 mm2. This means that the method used on the model before has here an overestimation of 110.56 %. But as the screw is a rather simple object compared to a human body, the percentage estimate could vary a bit.

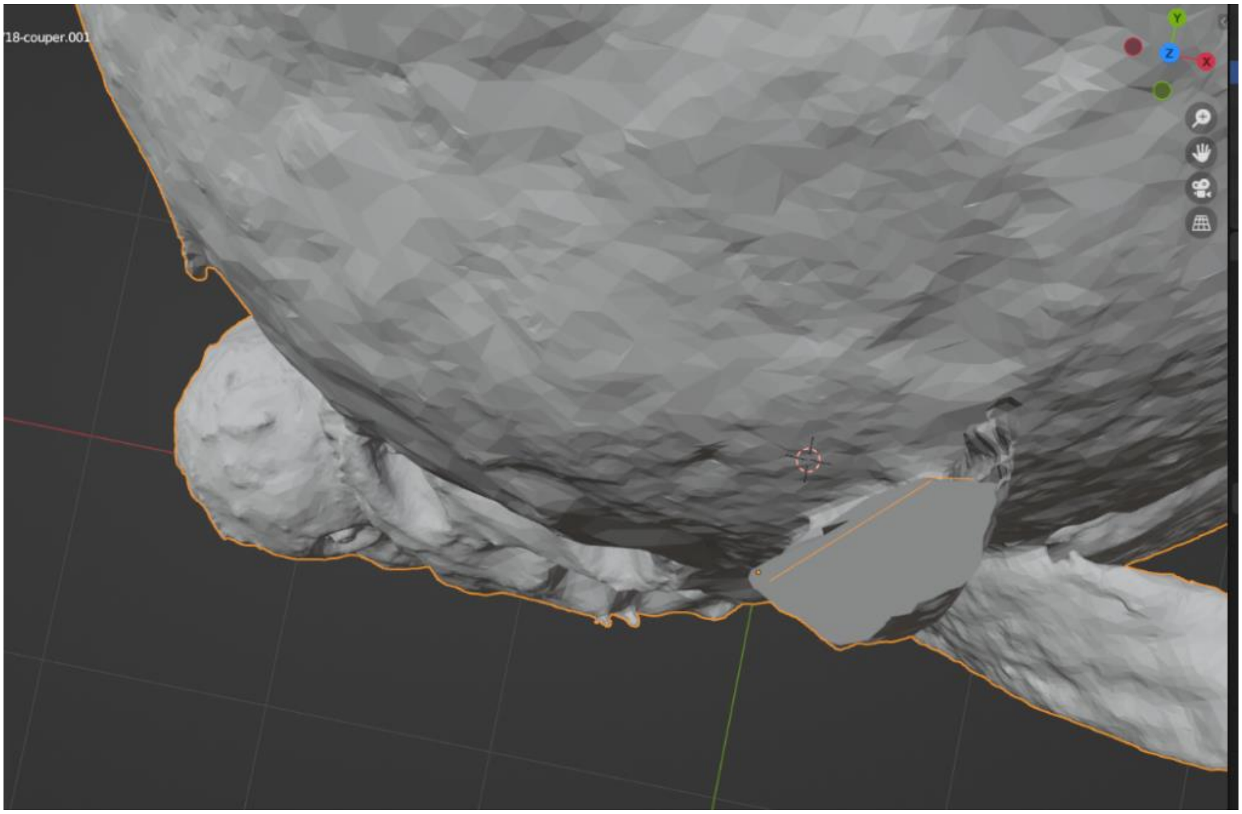

Figure 59 – Hole on the head or the feet of the model fill manually using blender

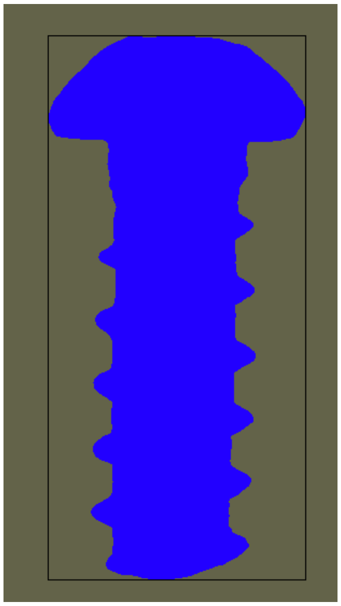

Figure 60 - Mesh of a screw by Artec 3D

3.2.5. Body Surface Area and Projected area factor

In the paper by Olds et al. (1995), formula (4) is used to calculate the projected surface of a cyclist in an aerodynamic position as a function of total body surface area.

$$\frac{A_p}{A_c} = 23.06 - 2.46\, A_c \qquad (4)$$

Where A_p is the projected surface and A_c is the total body surface.

The Body Surface Area (*BSA*) is the external surface of the skin covering the human body. It can be deduced in function of the mass and size of people. As mentioned by Tikuisis et al. (2001) in their article, laser scanning allows a more accurate determination of *BSA*. For a man, the best nonlinear regression to obtain the *BSA* is given by the following equation (5).

$$BSA\ [cm^2] = 128.1 * m^{0.44} * h^{0.60}\ (\text{with } m=\text{body mass [kg]},\ h=\text{height [cm]}) \qquad (5)$$

Another formula (6) is given by Dubois and Dubois (1916) but is a bit outdated even though it is used extensively in multiple articles.

$$BSA = C * m^A * h^B \text{ où } C = 71.84\ \ (\text{with } A = 0.425 \text{ et } B = 0.725,\ m=\text{body mass [kg]},\ h=\text{height [cm]}) \qquad (6)$$

The article of Robinette et al. (1999) is a survey of body measurements of people from three different countries including the Netherlands. The Dutch population is the tallest of the three and therefore the most appropriate population for comparison with our model. In the article, the maximum height for the Netherlands is 1.84 m for a weight of 78.4 kg. But even there, our model is taller.

As our model is 1m90 tall and no studies are found for such a height, the *BMI* (Body Mass Index) will be used to estimate its weight as if the model were a real human. The *BMI* is generally equal to the weight (kg) divided by the square of height (m). The *BMI* for an average person is estimated between 18.5 and 25 (Keys et al., 1972).

The *BMI* is estimated to be 23.2 in this case, as it is equivalent to the *BMI* resulting from the Dutch sample that was 1m84 tall (corresponding to a stratum of Dutch population between 18 and 29 years old). So, the weight of the 3D model if it was human is estimated to be of 88.25 kg (Table 6). Another *BSA* is also chosen and calculated for a *BMI* of 25 (Table 7) because the model is very large and tall, wearing XL pants and 2XL t-shirt, and appears to be larger than the Dutch models, so it would be logical that his *BMI* would be too. The weight for this BMI is 90.25 kg, which is indeed more likely to correspond to the model's build.

The Figure 61 resumes the BSA obtained with different equations for our model for a BMI of 25 and 23.2.

The difference in the BSA results obtained by Tikuisis et al. (Table 8) for the Dutch sample and the *BSA* obtained with the model is consistent. Indeed, none of the Tikuisis models has the extraordinary stature of Ken and therefore, a comparison between these values would be rather inappropriate.

Table 6 - BSA for the model for a BIM of 23.2

Equations	C	A	B	heigth [m]	weight [kg]	BSA [cm2]	BSA [m2]
Du Bois and Du Bois	71.84	0.425	0.725	190	83.75	21170.51	2.117
Boyd	178.7	0.484	0.5	190	83.75	21000.32	2.100
Gehan and Geoge	154.5	0.463	0.545	190	83.75	20950.34	2.095
Haycock	242.7	0.538	0.396	190	83.75	20990.46	2.099
Mosteller	166.7	0.5	0.5	190	83.75	21028.33	2.103
Shuter and Aslani	94.9	0.441	0.655	190	83.75	20791.51	2.079
Tikuisis	128.1	0.44	0.6	190	83.75	20937.01	2.094

Table 7 - BSA for the model for a BIM of 25

Equation	C	A	B	heigth [m]	weight [kg]	BSA [cm2]	BSA [m2]
Du Bois and Du Bois	71.84	0.425	0.725	190	90.25	21853.84	2.185
Boyd	178.7	0.484	0.5	190	90.25	21773.98	2.177
Gehan and Geoge	154.5	0.463	0.545	190	90.25	21688.09	2.169
Haycock	242.7	0.538	0.396	190	90.25	21851.78	2.185
Mosteller	166.7	0.5	0.5	190	90.25	21829.11	2.183
Shuter and Aslani	94.9	0.441	0.655	190	90.25	21488.3	2.149
Tikuisis	128.1	0.44	0.6	190	90.25	21637.05	2.164

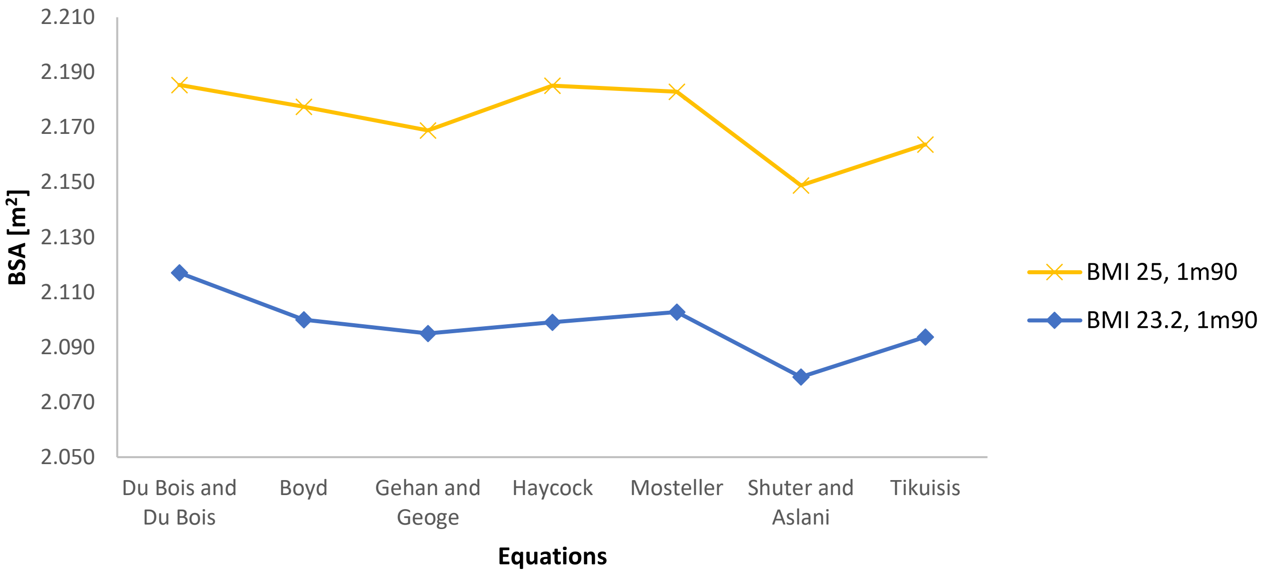

Figure 61 - BSA of the model for different equations for Ken

Table 8 -BSA for models in the article of Tikuisis et al., 2001

Equation	Mean BSA [m2]
Du Bois and Du Bois	1.910
Boyd	1.927
Gehan and Geoge	1.917
Haycock	1.937
Mosteller	1.927
Shuter and Aslani	1.886
Tikuisis	1.9165

The equation of *BSA* chosen is that of Tikuisis et al. (2001) as it appears to be more accurate and more recent than others proposed. It can therefore be concluded that the *BSA* is in the range of 2.094 and 2.164 m^2 for the model and this result is logical in the case of an oversized model like Ken.

The *BSA* of 2.164 m^2 is smaller than the total surface area value of 2.241 m^2 obtained previously, which is consistent since this value is an approximation and not the exact total surface area which could not be obtained.

The projected area factor (f_p) is the ratio of the projected area to effective area (Tanabe et al., 2000). The projected area is discussed in Section 3.2.2 and the effective area is discussed in Section 3.2.4. The equation for the projected area factor is $f_p = A_{projected}/A_{total}$.

The A_{total} used here is 2.241 m^2. A graph of f_p in function of alpha is available on Figure 62 with a comparison between standing persons modelled by Fanger et al. (1970) and our model. This graph takes into account an angle Bheta, which is the angle given by Figure 63 and which corresponds to a different angle of view for the different pictures taken. It is important to note that in this graph, the azimuth of the model for 0 degree corresponds to the position of the model of 90 degrees along the *x-axis* on Figure 36 and conversely the azimuth of the model for 90 degrees corresponds to the position of the model of 0 degree along the *x-axis*.

The trend followed by the curves obtained by Fanger et al. (1970) is not respected by the model curve. This may be due to inaccuracies in the projected areas (especially due to the alignment of the limbs) or to uncertainties in the total surface area previously calculated. These differences are particularly important for the values of 75, 90 and 120 degrees which correspond to the position of 15, 0, -30 and -45 degrees on Figure 36. These differences can be explained by the fact that the model (Ken) has a larger stature than the models used by Fanger et al. (1970) in his experience. Indeed, Fanger et al. experimented on both male and female. The projected area is also underestimated by the results obtained with the model in comparison to the value obtained by Fanger et al. (1970). These differences in results can be explained by the fact that the numerical method used by Fanger et al. is not the same as the one used in this dissertation. In addition, the A_{total} used in this calculation is overestimated which can explain the underestimation of the f_p for the model (Ken).

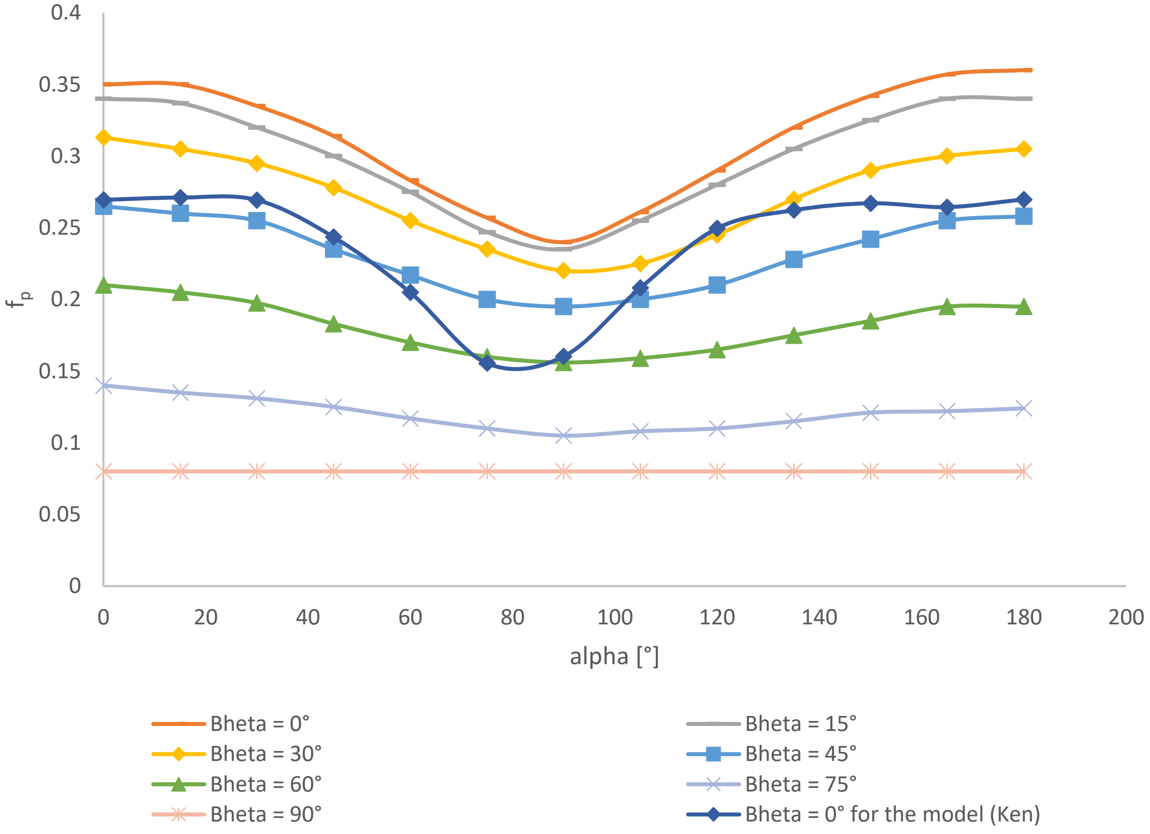

Figure 62 - Graph of f_p in function of alpha for standing people and for the model (Fanger et al., 1970)

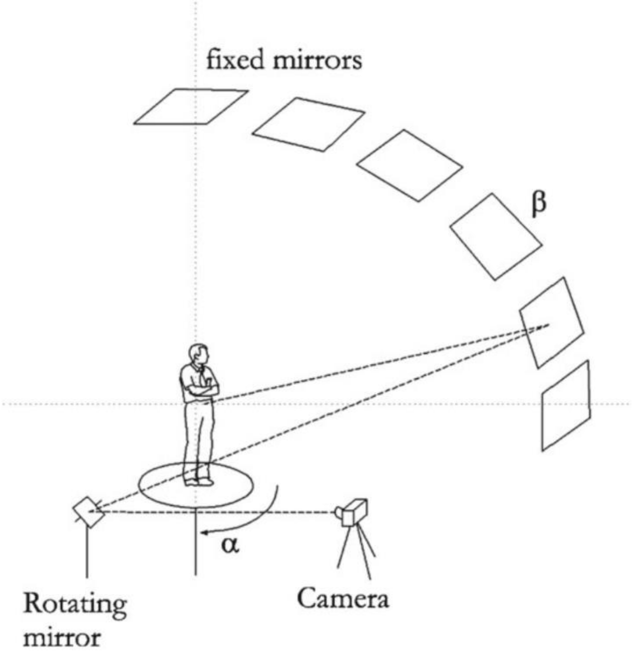

Figure 63 - Description of the photographic method of Fanger, with Bheta = 15° (Nucara, 2012)

4. Experimental modeling

4.1. Modification of the model

In order to be able to fix the model on the base -composed of an aerodynamics balance- of the wind tunnel, it is necessary to make several modifications to the model, to make it possible to fix its too mobile ball joints and to maintain the body in balance on the base with the desired configuration without it touching the ground. This maintenance must be accomplished with a material that is not too intrusive so as not to distort the results.

4.1.1. Modification for the first results

In order to keep the ball joints fixed, the first system implemented in place is the stiffening of the ball joints. Indeed, the Randy 9000 is not rigid as it should normally serve other purposes (as discussed in 3.1.).

To do this, neoprene joints are added to stiffen the joints in the legs and pelvis (Figure 64). Next, the normal cylinders of the joints are replaced with 3D printed cylinders whose mobility is reduced to 90 degrees (2x45 degrees) in total, instead of the original 180 degrees. Although this does not fix the joint 100%, it limits its movement (Figure 64). Finally, a thicker washer is used to clamp the two half-spheres of each joint together. This limits the movement of the joints using stiffening by friction.

The model must be placed on a female part that can be mounted on the male part of the prop used in the wind tunnel to make the measurements (Figure 64). This female part is thus attached to the model from a gas line collar placed around its ball joint at the level of the pelvis. This allows the part to be place without having to install a plate or some other intrusive system that would have alter the shape of the model.

Nevertheless, during the experiment, sticky paper is used to maintain the arms at chest height and the legs almost touching the ground.

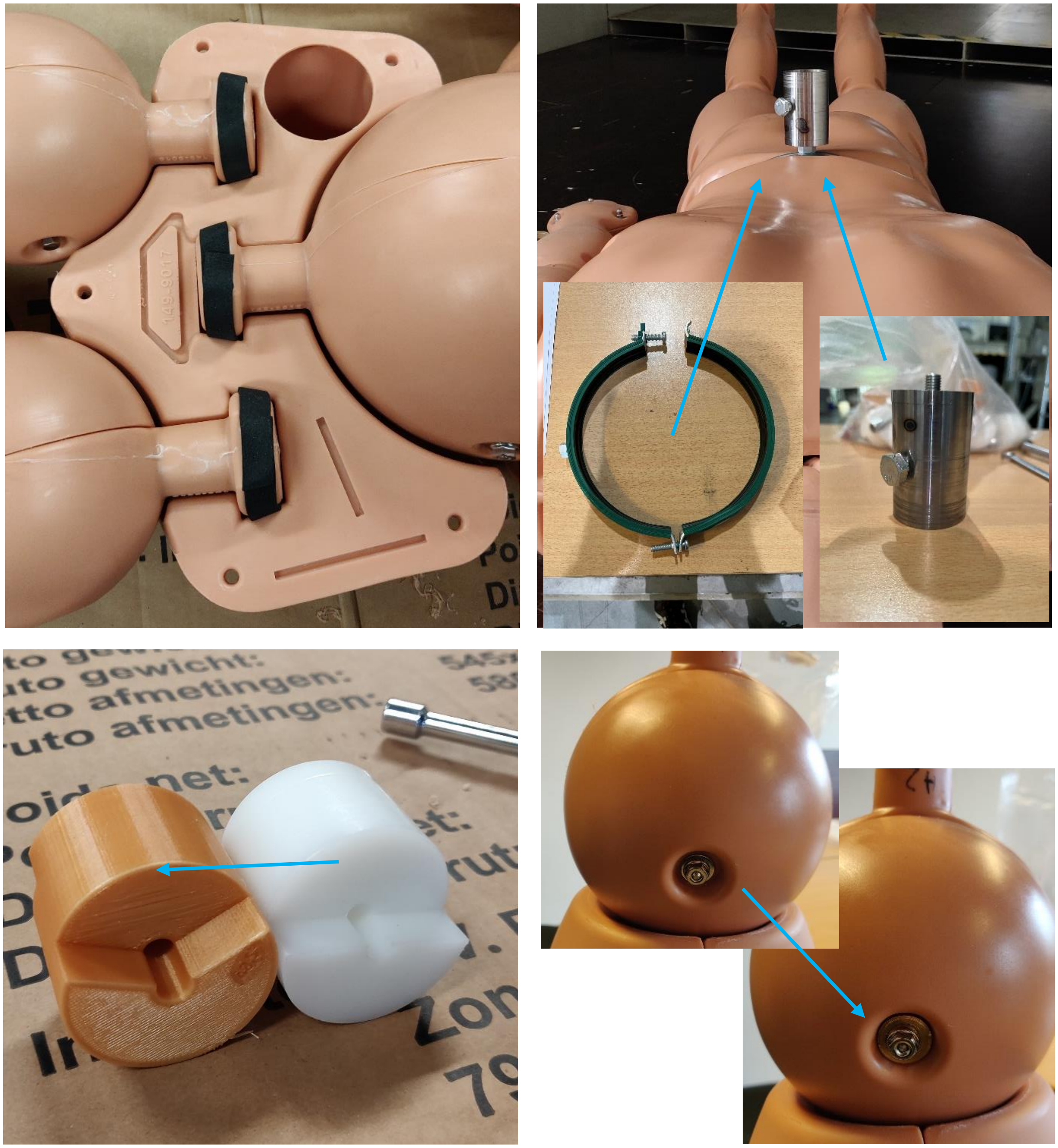

Figure 64 - Photos of the improvements made on the model (top left: neoprene; top right: female part to be able to fix the model on a male part on the base used in the wind tunnel, bottom left: in brown parts to fix the kneecaps of the shoulders and legs to replace the white one, bottom right: cylinder piece)

4.1.2. Modification for second slots of results

The previous arrangements are not sufficient to obtain the desired results and one of the decided configurations. To further improve it, another part is placed at the level of the ball joints (Figure 66). This notched piece modeled in 3D allows the ball joints to be fixed with greater efficiency. The difficulty in creating such a part is mainly due to the precision required in the notches but also comes from the material used to manufacture it. Indeed, the piece is easily breakable and the model must therefore be handled with great care to prevent this from happening.

The addition of a metal piece at the junction between the arm and the torso on both arms (Figure 65), also allows the arm to be kept straight without the need for adhesive paper or other more invasive methods.

Finally, the empty part of the torso is filled with water in order to raise its center of gravity and make it stands straighter during the experimentation.

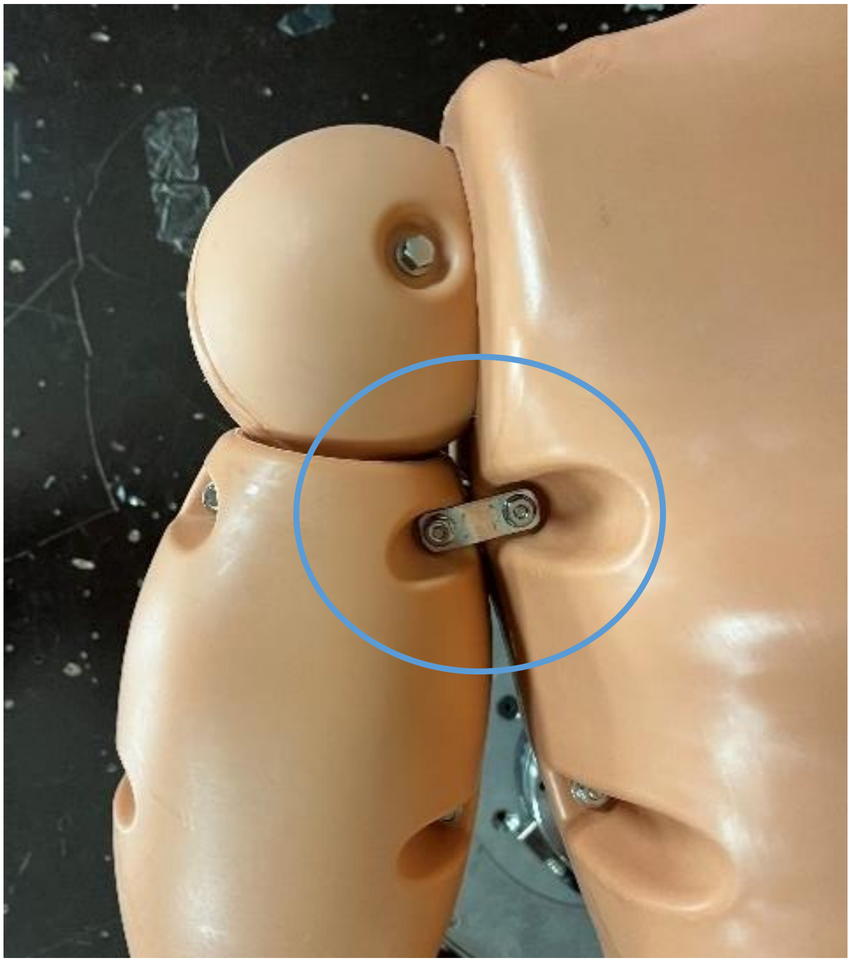

Figure 65 -Metal piece at the junction between the arm and the torso

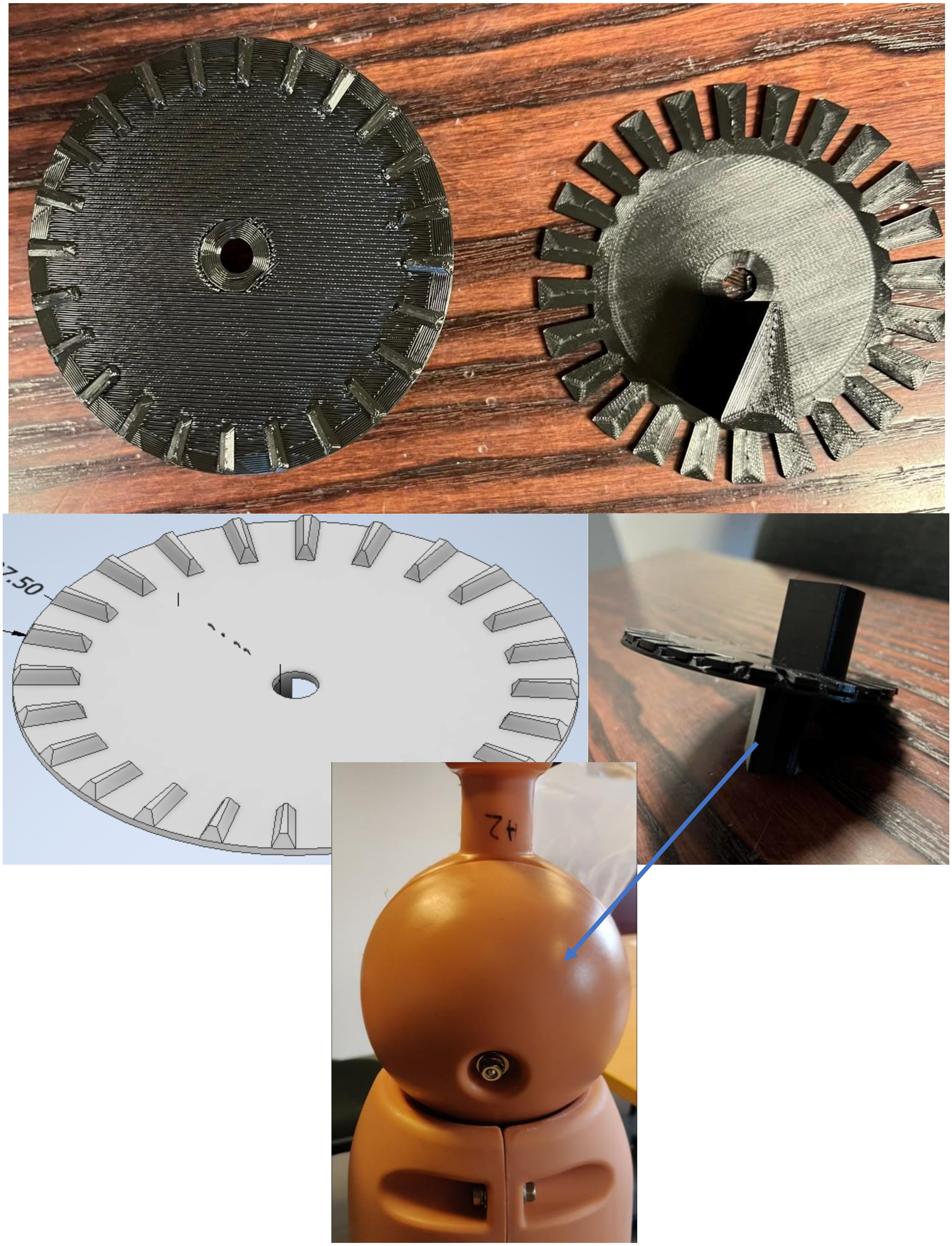

Figure 66 - Parts added to the ball joints to fix them

4.2. Wind tunnel and referential

A wind tunnel is a tool for studying the effects of airflow around a fixed object. It is composed of a circular tube in which the air is in motion thanks to the action of a fan (Figure 67). The one used at the University of Liege is a closed loop subsonic tunnel (Prandtl) and focuses on tests below 65m/s (Figure 68). In this kind of wind tunnel, the flow regime is compressible and the continuity law can be written as detailed in equation (7).

$$-\frac{1}{a^2}\frac{dp}{\rho} = -\frac{1}{a^2}\frac{-\rho V dV}{\rho} = \frac{V}{a^2}dV \qquad (7)$$

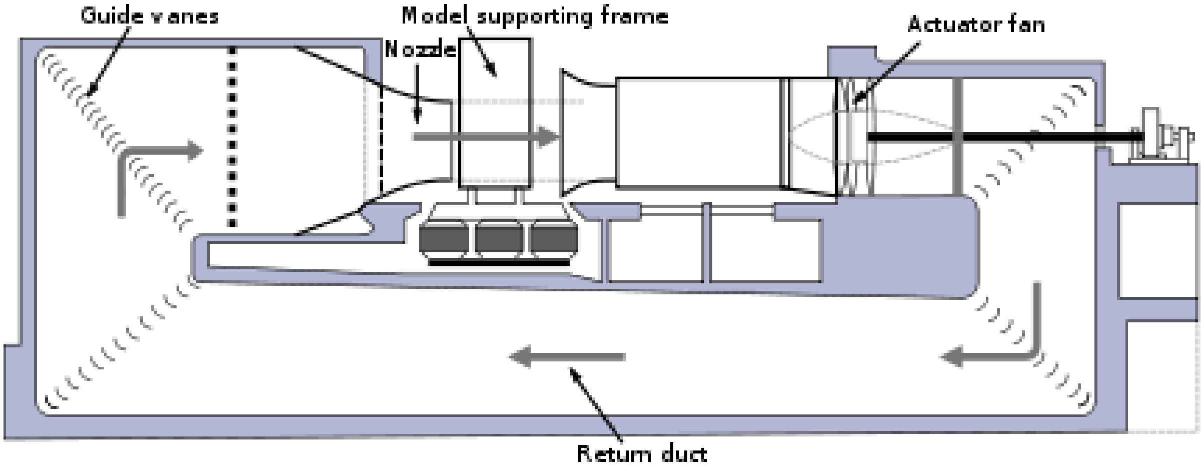

Figure 67 - Wind tunnel in close loop (Tomia and Liftarn, 2007)

Figure 68 – Wind tunnel of the university of Liège, and the aerodynamic balance on which the model will be pose

The aim here is to reproduce the conditions under which the model would be found if it was swept along by the current of a river. The air velocities must to be appropriate to represent the same Reynolds number as what will be experienced in the water. The model is therefore held in a stationary position but behaves as if it was in motion.

The model is placed in a test chamber, on an aerodynamic balance to measure the forces acting on it (Figure 68). The wind speed is measured by an anemometer (Figure 69) and a control box is used to obtain the desired speed value.

A reference frame for the position of the model in the wind tunnel is available in Figure 70 and Figure 71, with *x,y,z* the three axis and with ϑ the yaw angle.

Figure 69 - Control box (left) and anemometer (right)

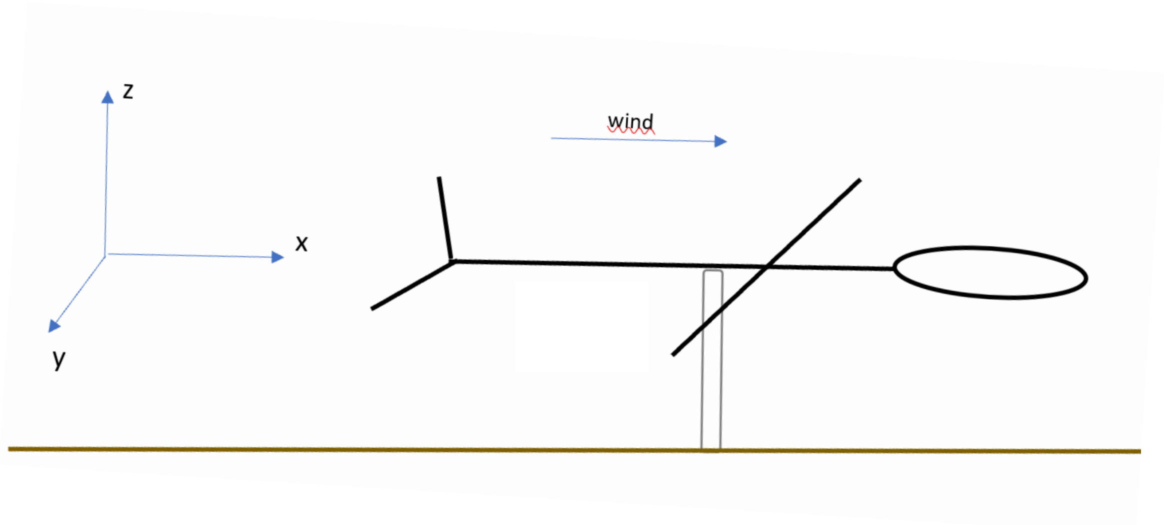

Figure 70 - Referential in the wind tunnel side view (ground in gold, mannequin in black, prop in grey), for a model at θ = 0°

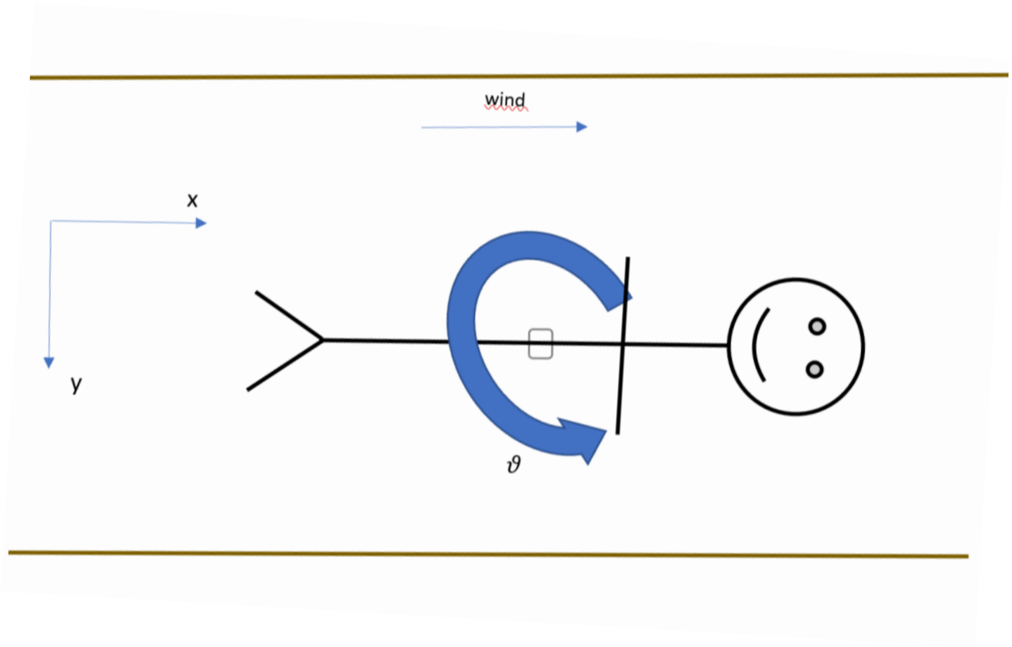

Figure 71 - Referential in the wind tunnel, top view (wall in gold, mannequin in black, prop in grey) for a model at θ = 0°

4.2.1. First results

A first series of tests is carried out after the modification described in Section 4.1.1. on the model. These results are detailed in this chapter.

A calibration is first performed to adjust the error in the results of the aerodynamic balance. To do this, weights are placed on the model along the *x-axis* at four different locations and permit to obtain a graph of the force compared to the torque along *x-axis* (Figure 72). The slope of the equation of this graph is 0.0489 and allows to obtain the parasite force along the *x-axis*.

Then, four slots of results are made: one with the model at 0 degrees and naked, one at 180 degrees and naked and then for the same two angles with a model with clothes on (Figure 73).

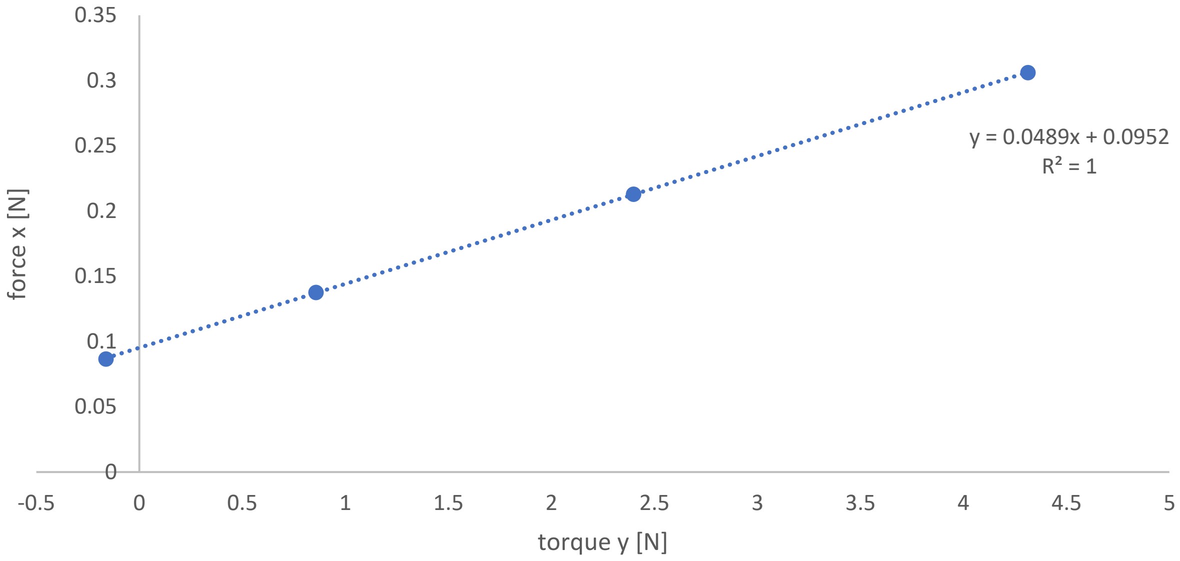

Figure 72 – Mean of the calibration along x-axis force and its interpolation

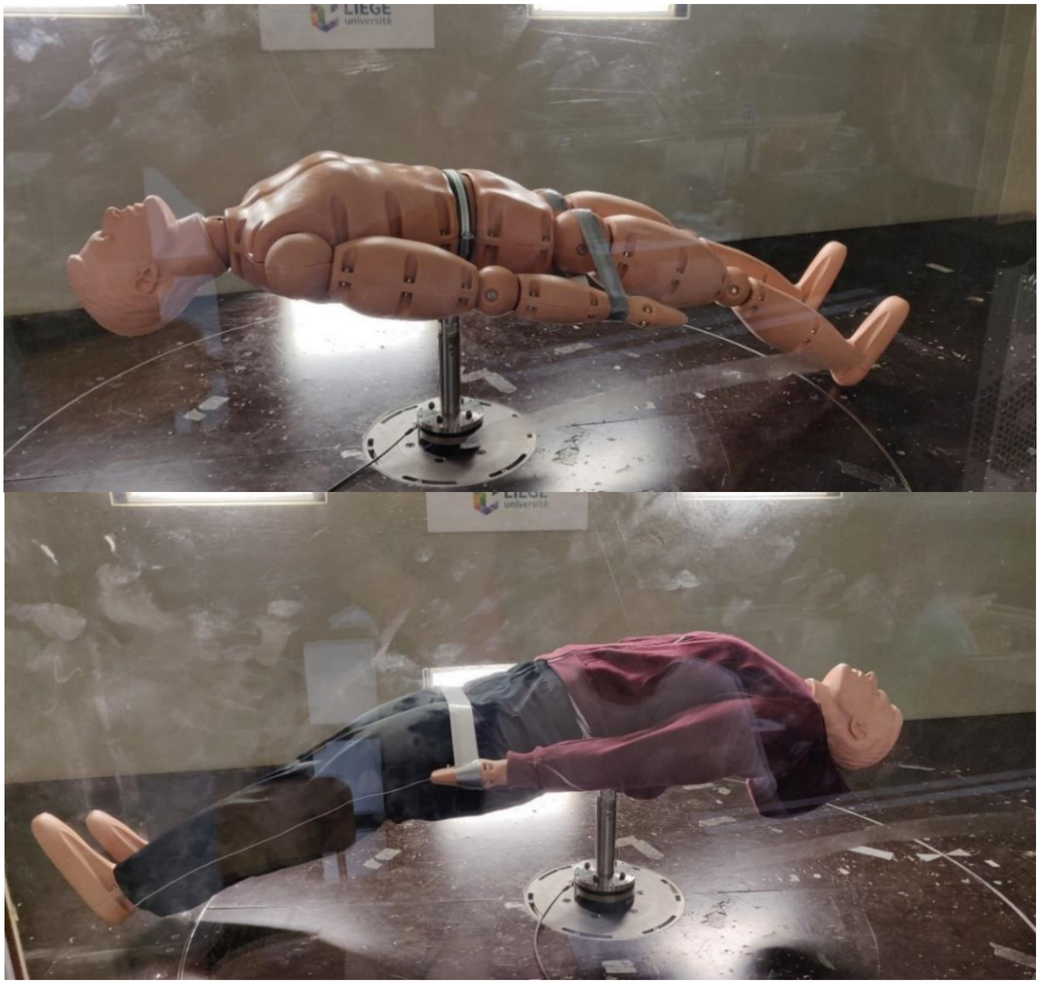

Figure 73 - Position of the model in the wind tunnel with the first arrangement, for configuration 1 with and without clothes for an angle of 0 degree (top) and 180 degrees (bottom)

The Table 9 includes the conditions under which the experiment takes place. The dynamic viscosity and the mass density of the air are obtained from the interpolation of Figure 74 and a data table respectively (Thermexcel, 2001). The aerodynamics balance is used to calculate the force along *x, y* and *z axis* and their respective torque for a known air speed.

Table 9 – Condition of the first results

Parameters	Value	Units
Temperature T	20.2	°C
Pressure P	99335	Pa
Dynamic air viscosity ν	$1.6*10^{-5}$	m^2/s
The air mass density ρ	1.204	kg/m^3
The wind tunnel section	4.5 (2.5m width*1.8m height)	m^2

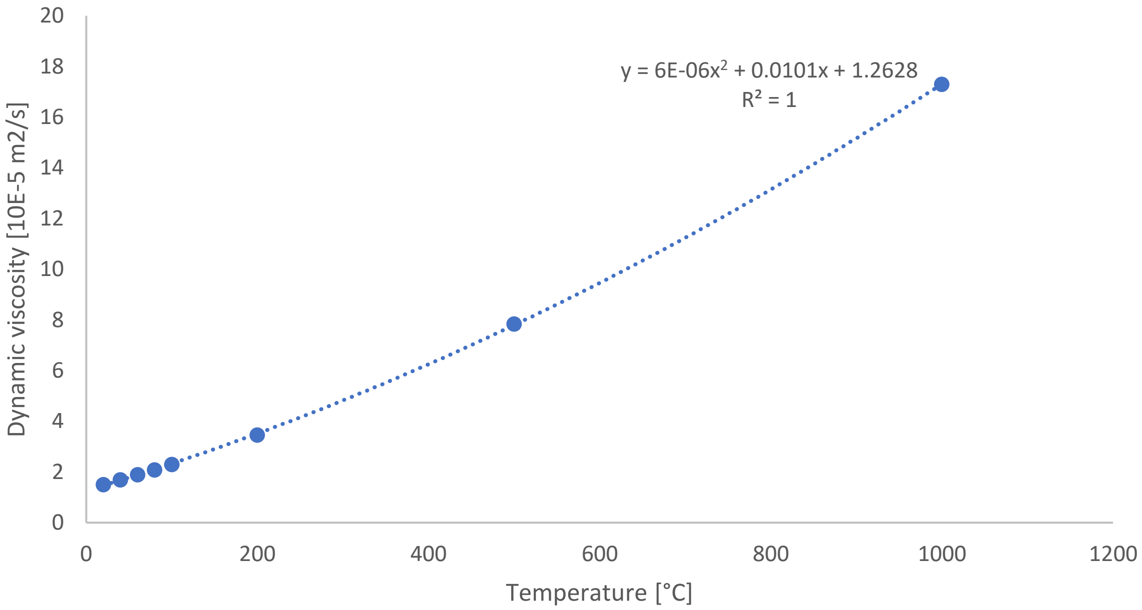

Figure 74 - Dynamic air viscosity as a function of the temperature and its interpolation (Huilier, 2010)

Moving averages are calculated to ensure that the number of samples and frequency are sufficient for convergence of results (Figure 75 and Figure 76). These averages are used to conclude that the number of samples taken during the tests is sufficient and representative. Thus, it is known that for the second slots of test, a time of 15 seconds at a frequency of 200 Hz for each speed is sufficient to obtain usable results.

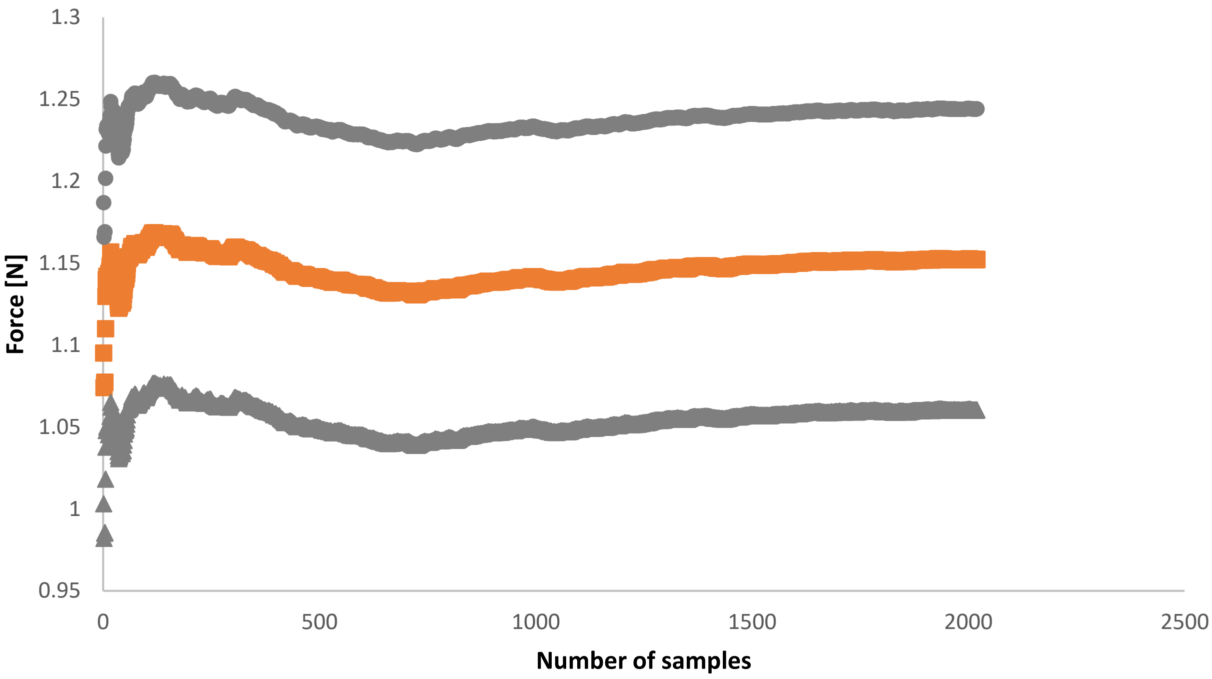

Figure 75 -Moving average of force (orange) for the model at 180 degrees with wind at 4.2 m/s and its standard deviation (grey)

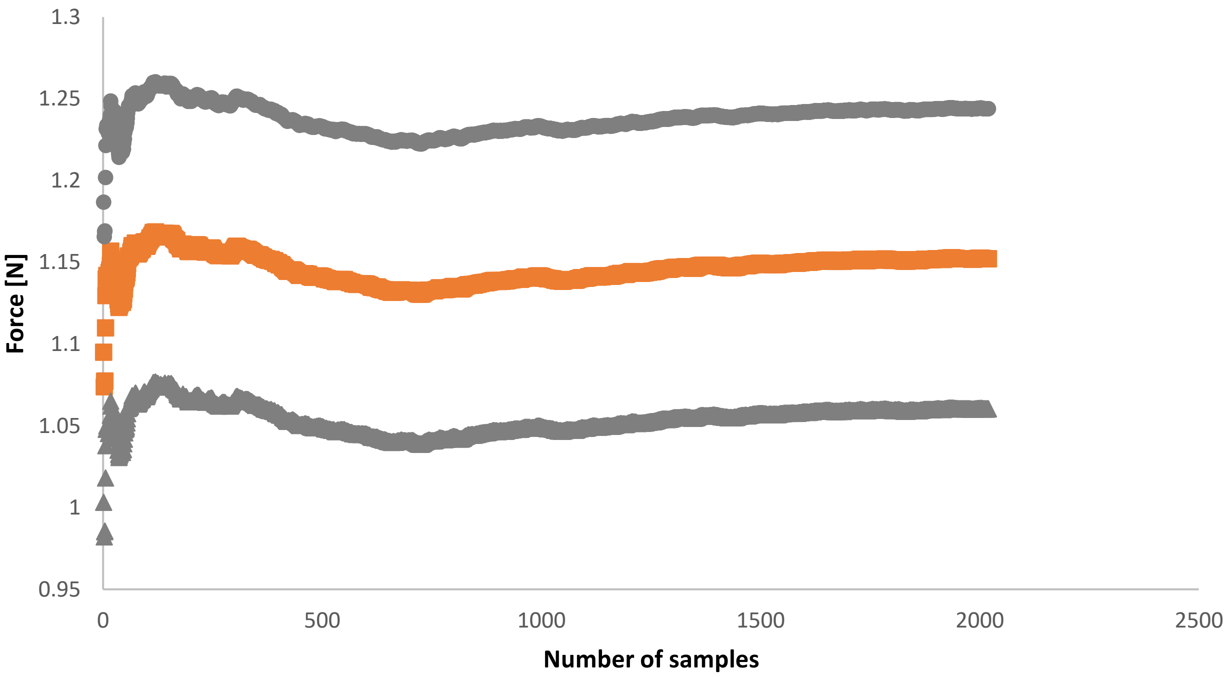

Figure 76 - Moving average of force (orange) for the model at 180 degrees with wind at 7.7 m/s and its standard deviation (grey)

The force along x is not the exact force that occurs on the model as the calibration is not yet taken into account. The equation (8) is used to calculate the $F_{x,real}$. Then, this $F_{x,\mathrm{real}}$ is applied to obtain the drag coefficient of the model with equation (9). The Reynolds number is also calculated according to equation (10) in order to compare the results with those of different papers.

$$F_{x,real} = F_x - 0.0489\, T_y \qquad (8)$$

$$F_{x,real} = C_x \frac{1}{2} \rho v^2 A \qquad (9)$$

$$Re = \frac{\rho v l}{\mu} \qquad (10)$$

Once these calculations have been made, Figure 77 and Figure 78 are processed. The force results seem logical, with lower recorded forces for low speeds and higher forces at high speeds. The results with the naked or clothed model are quite close, which can be explained by the fact that in both positions, the projected surface of the model is assumed to be the same.

The drag coefficient results are not very consistent with what can be found in the literature as the range of value seem to be underestimated compared to the value found by Schmitt (1954) and also with values that tend to vary with the Reynolds number. These poor results can be explained by the measurements carried out in the wind tunnel with a dummy that does not stand upright on the base and with measurements that may be hampered by the proximity of the feet to the floor or the presence of tape around the arms of the model. A second series of measurements will therefore be carried out, after ensuring the quality of the measurements by modifying the model rigidity.

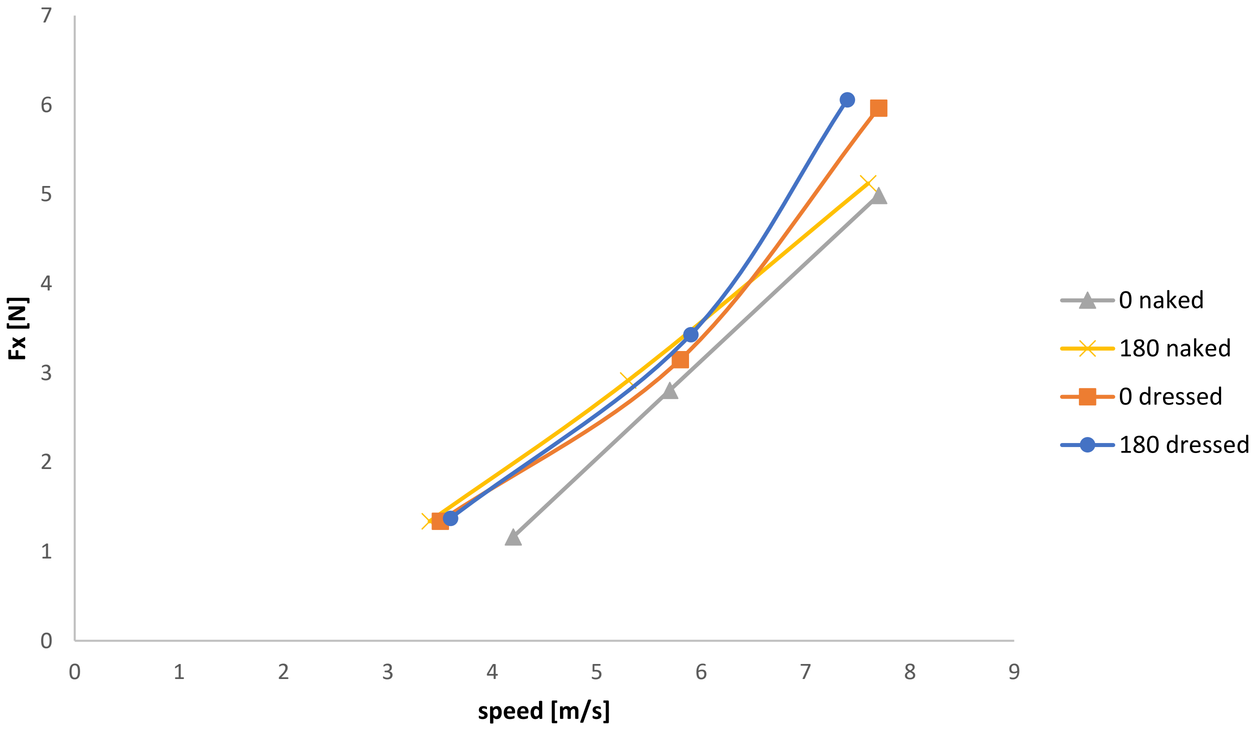

Figure 77 - Force x in function of the speed of the wind for the model in configuration 1, at 0 and 180 degrees with and without clothes

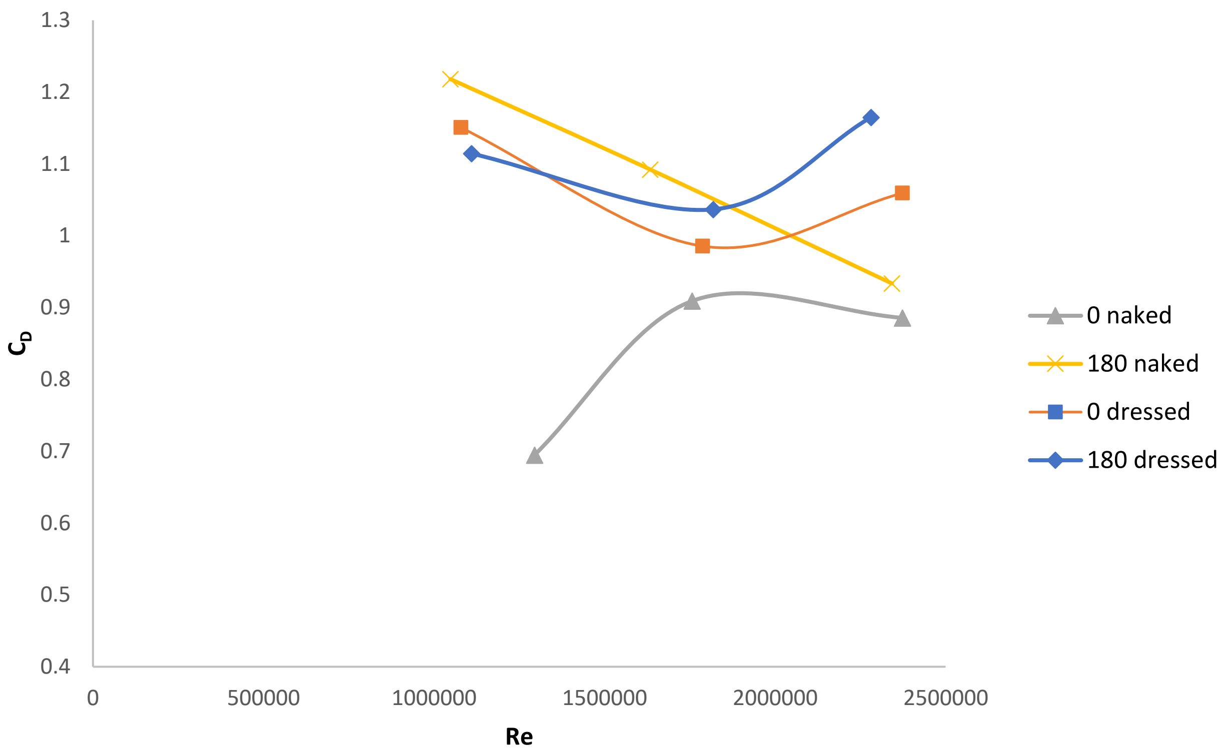

Figure 78 - C_D in function of Re for the model in configuration 1, at 0 and 180 degrees with and without clothes

4.2.2. Second results

The second series of results is carried out for other angle values than the previous ones of 0 and 180 degrees. This time, two calibrations are performed, one according to the x-axis and the other one according to the x-axis.

Those two calibrations are then used to adjust the error due to the aerodynamics balance. For the calibration along the *x-axis*, a 1 kg weight is placed at different locations on the model in order to obtain a graph of the force along *x-axis* compared to the torque (Figure 79). The slope of the interpolation of the graph points is here 0.0489 which is the same as for the first experimental results which proves that the error of the balance is the same, which is consistent. This value is used to obtain the parasite force along the *x-axis*.

For calibration along the *y-axis*, four different weights (1 kg, 500 g, 200 g and 100 g) are used as it is not possible to move the weight to four different locations along the *y-axis*. This is used to obtain the graph of the force along y-*axis* in comparison to the torque (Figure 80). The slope of the interpolation of the graph points is here -0.1786. This value is also used to obtain the parasite force but here along the y-*axis*.

Once these calibrations are carried out, sets of results can be processed for the model in the position of configuration 1 for many different angles ϑ (Figure 81).

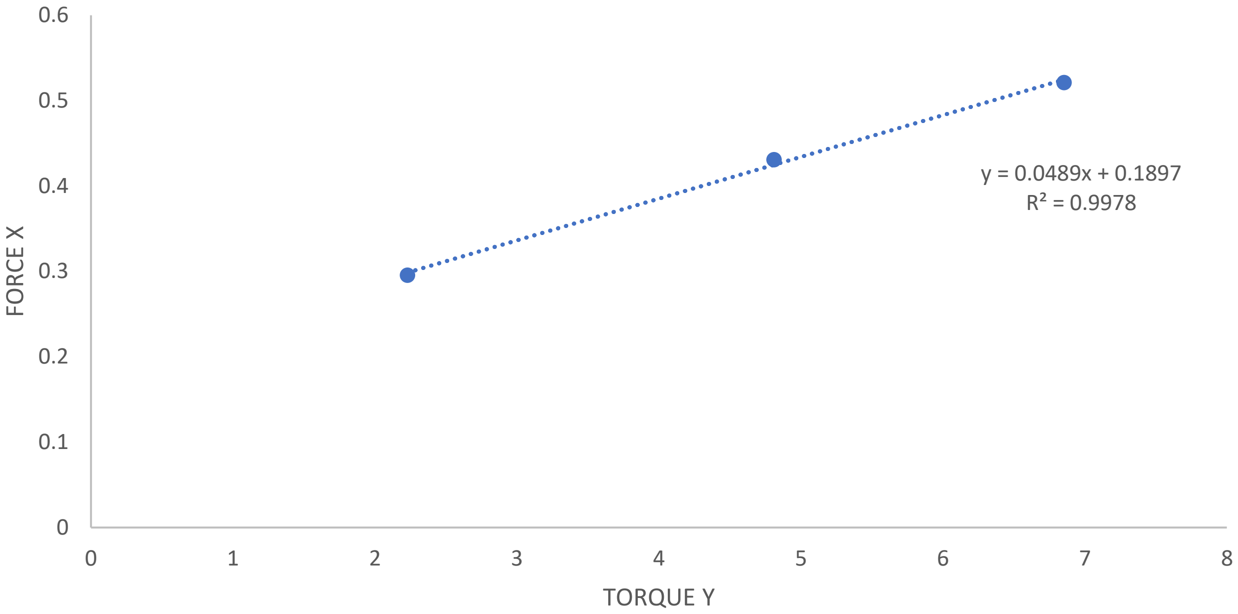

Figure 79 -Mean of the calibration along x-axis force and its interpolation

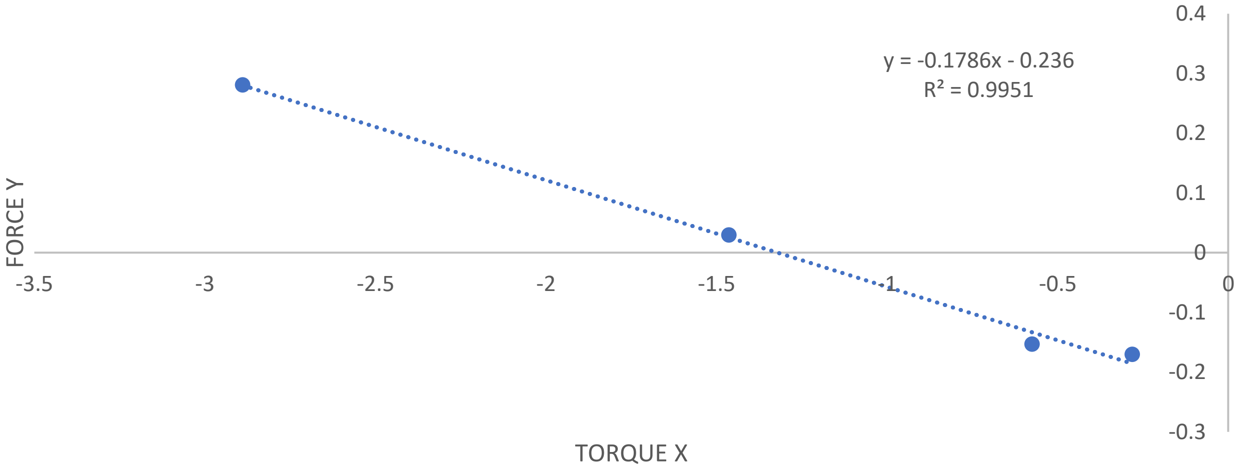

Figure 80 - Mean of the calibration along y-axis force and its interpolation

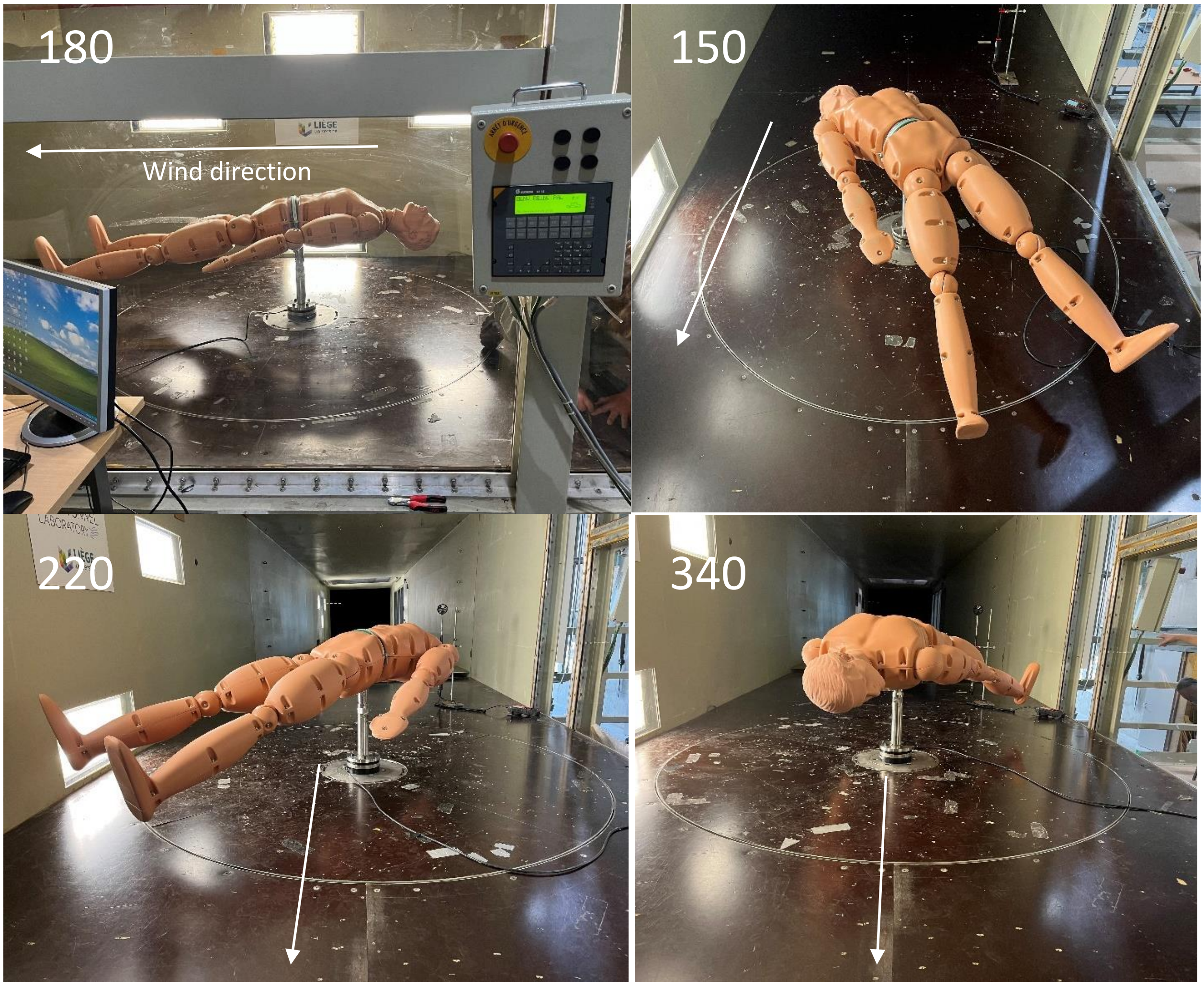

Figure 81 - Position of the model for different angle (180, 150, 220, 340°) and from different point of view for the configuration 1 on the wind tunnel (wind direction: white arrow)

Table 10 includes the conditions under which the experiment takes place, the dynamic viscosity and the mass density of the air are obtained using the interpolation in Figure 74 and a data table (Thermexcel, 2001) respectively. As with the first sets of results, the aerodynamic balance is used to calculate the force along *x, y* and *z axis* and their respective torque for a known air speed.

Table 10 – Condition of the second results

Parameters	**Value**	**Units**
Temperature T	23.7	°C
Pressure P	99429	Pa
Dynamic air viscosity ν	$1.5*10^{-5}$	m^2/s
The air mass density ρ	1.188	kg/m^3
The wind tunnel section	4.5	m^2

Moving averages are calculated for each position studied and for the different wind speeds to ensure that the number of samples is sufficient for the convergence of the results (Figure 83 and Figure 82) since the experiment is conducted for 15 seconds for each different wind speed and angle. From the moving averages obtained, it can be concluded that the number of samples taken during the tests is sufficient and representative.

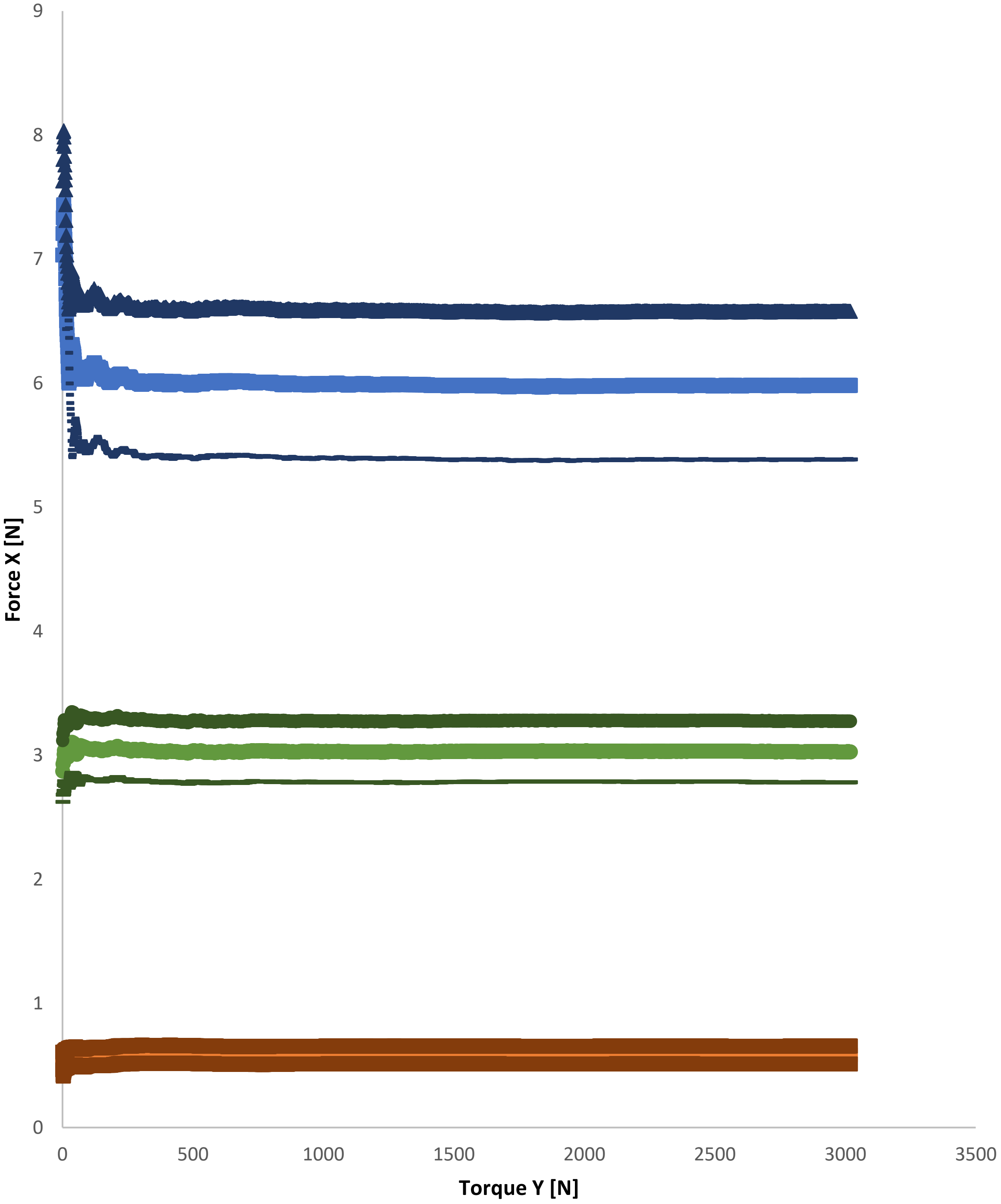

Figure 82 - Moving average of force (light colors) for the model at 150 degrees with wind at 3.1 m/s (in orange), at 6.6 m/s (in green) and at 9.3 m/s (in blue) and its standard deviation (dark colors)

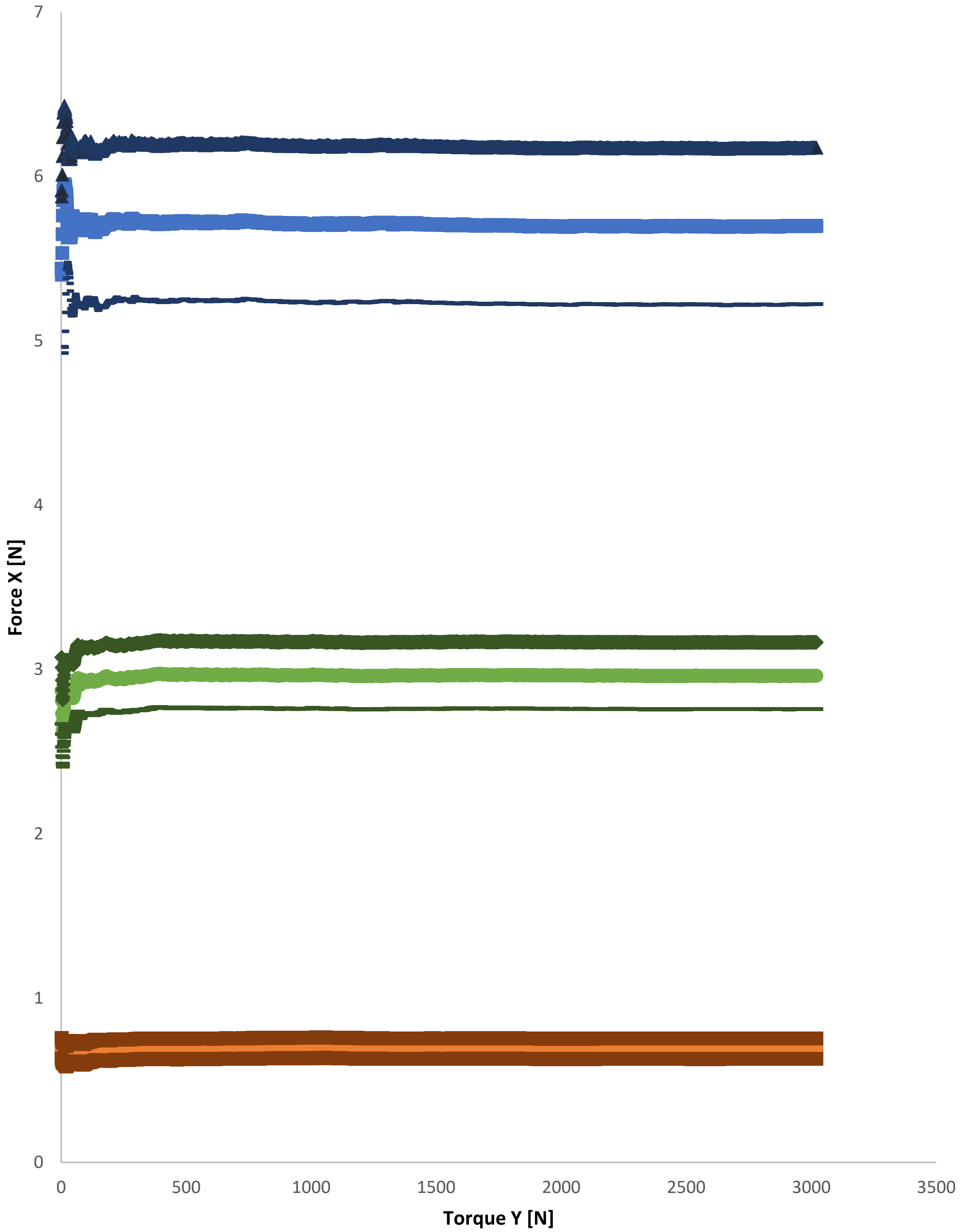

Figure 83 - Moving average of force (light colors) for the model at -10 degrees with wind at 3.1 m/s (in orange), at 6.6 m/s (in green) and at 9.3 m/s (in blue) and its standard deviation (dark colors)

The force along *x* and along *x-axis* is not the exact force that occurs on the model because the calibration is not yet taken into account. The equation (11) is used to calculate the F_{total}. Then, this F_{total} is used to calculate the drag coefficient of the model using equation (9). And as for the first set of results, the Reynolds number is also calculated according to equation (10) in order to be able to compare the results with those of different papers.

$$F_{total} = (F_x - 0.0489\, T_y) * \cos(\theta) + (F_y + 0.1786 T_x) * \sin(\theta) \qquad (11)$$

The total force results are available in Figure 84. This graph permits to see the trend of the forces which are increasing with the wind speed in the tunnel. For all angles, the trend seems to be quite similar even if the forces tend to increase faster for some angles than for others. Normally, some angles should have the same kind of trend, like 0 and 180° degrees or 20 and 340° degrees. This is not perfectly the case, which can be explained by the fact that the model is not exactly symmetrical, with differences when the feet or the head are in front or behind. For angles of 340 and 350°, the differences in the results can be explained by the fact that in order to be able to compute them, it was necessary to move the model and a calibration was not performed between the move and the taking of the results, so the calibration used can be slightly different and lead to an error in the results. Another important factor is the wind speed. Indeed, the chosen wind speed is between 3.1 and 9.4 m/s which is not very high. It is possible that the body of the model vibrated a little when the results were taken - due to a notched piece that broke during the wind tunnel experiment - resulting in these differences. Finally, as it can be seen in Figure 81, one of the notched pieces placed in the ball joint of the model's right leg broke during handling of the dummy, causing a misalignment of one of the two legs and possibly having a slight impact on the results.

In addition to this, the clamping screw that holds the dummy against the wind force to prevent it from rotating broke. This led, for some measurements with a larger projected surface A_p, to not obtaining results at too high speed (9.4 m/s or even 6.6 m/s for certain angles) because the model rotates and the results are not usable.

Figure 85 represents the C_DA as a function of the Reynolds number, which does not take into account the total surface projected A_p and the Figure 86 represents the C_D as a function of the Reynolds number. This allows comparison of these results with those of papers for which similar graphs or values are available. Normally, as for the forces, the trend should be fitting for opposite angles, but the same errors than the previous ones may have impacted the results. This is particularly true for C_D values that take into account the total area, as this value is already subject to its own uncertainties due to digitisation of the model. The C_D results for the same angle at different Reynolds numbers should be within the same value limit but this is not the case, some C_D results are quite different depending on the Reynolds number.

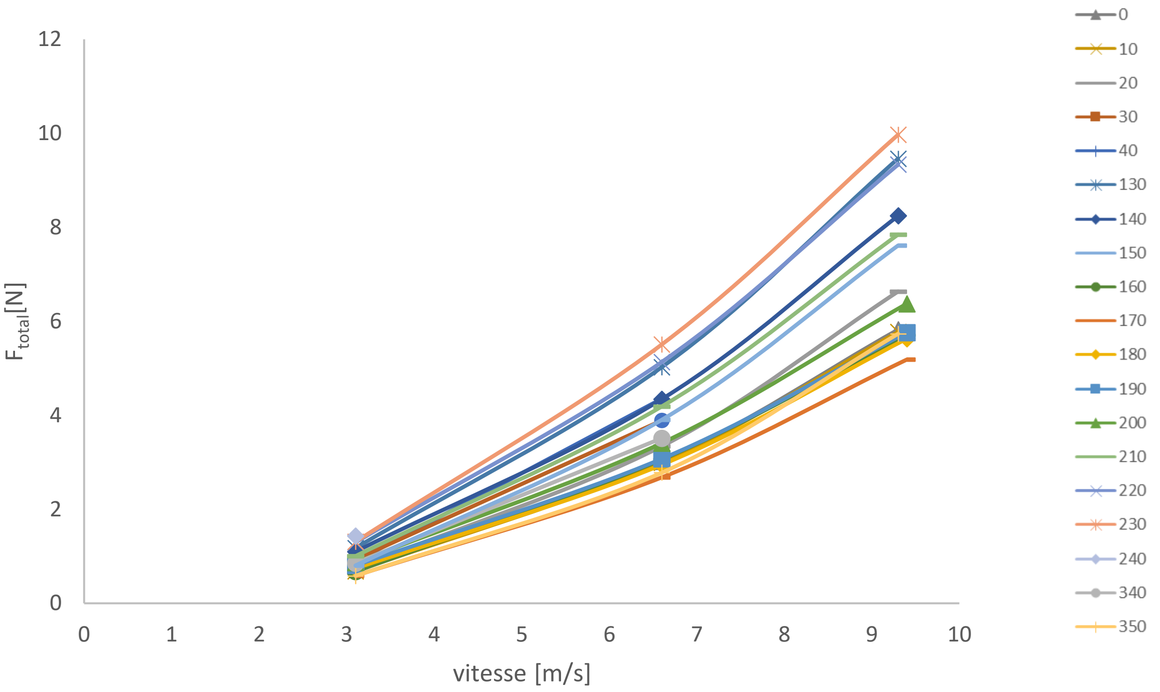

Figure 84 - Force total in function of the speed of the wind for the model in configuration 1, for different angle ϑ (legend)

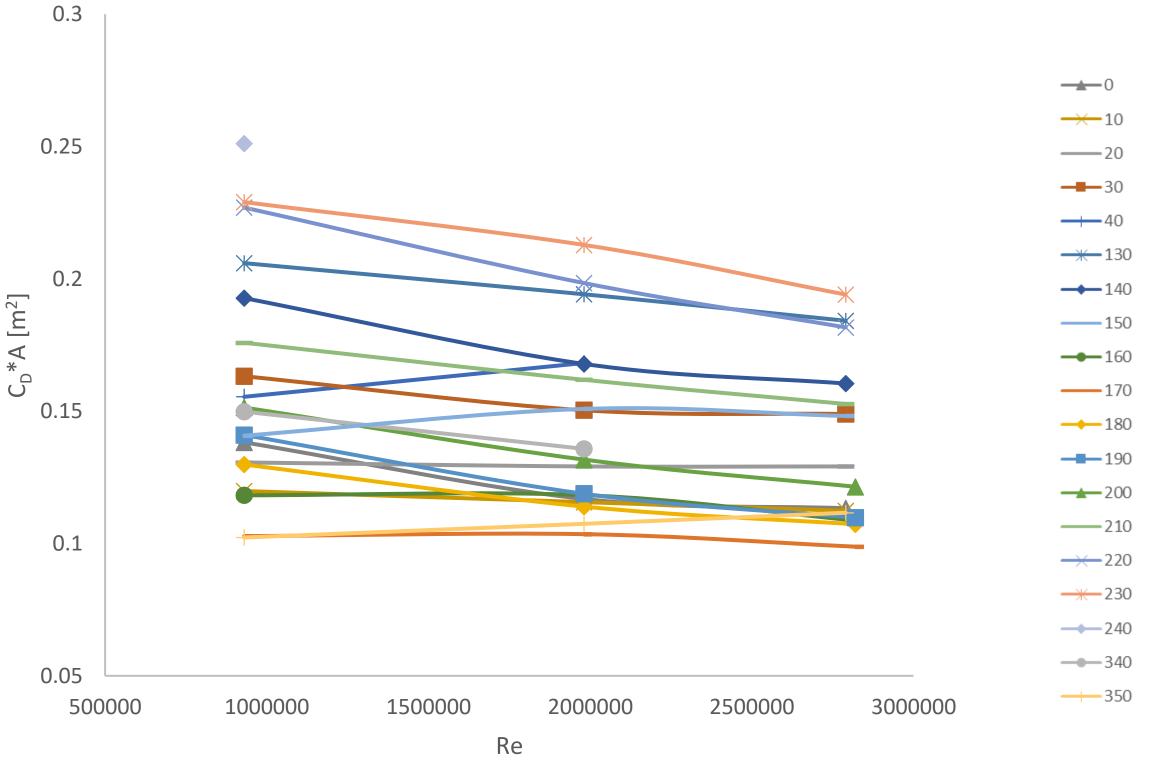

*Figure 85 – C_D*A in function of the Reynolds number for the model in configuration 1, for different angle ϑ (legend)*

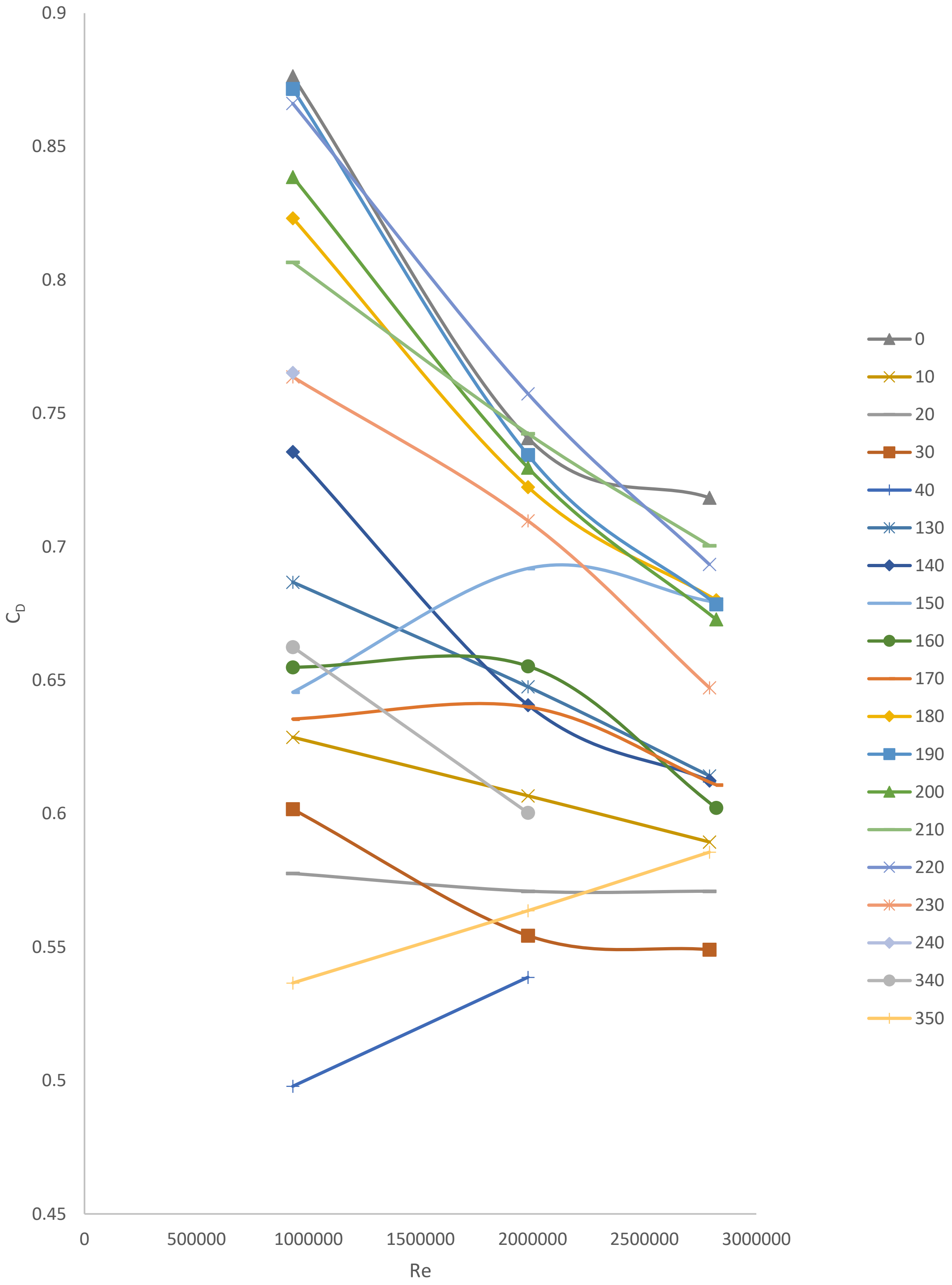

Figure 86 - C_D in function of the Reynolds number for the model in configuration 1, for different angle ϑ (legend)

In Figure 86, the uncertainties for an interval of 95% of the results are realized and are represented by errors bars and available in the Appendix (Figure 123). In order to obtain the uncertainties of the drag coefficient and the Reynolds number, the standard deviation of forces is first calculated using equation (12) and the wind speed (*U*) accurate to one tenths of a m/s. Afterwards, equation (13) gives us the 95% uncertainties for the drag coefficient. For the Reynolds number, only the uncertainties of the wind speed are used. It is important to note that the uncertainties for the drag coefficient do not take into account the uncertainties related to A_p.

$$\sigma = \frac{\sqrt{\frac{\Sigma(F_i-\bar{F})^2}{n-1}}}{\sqrt{n}} \qquad \textit{(n= number of samples)} \tag{12}$$

$$\textit{Uncertainties } C_D = C_D[\left(\frac{2*\sigma_F}{F}\right) + \left(\frac{0.1}{U}\right)] \tag{13}$$

These results of uncertainties (Figure 123) show that the values obtained at low speeds have greater uncertainties than the measurements obtained at higher speed. In general, the uncertainties on the results for the speed of 3.1 m/s are quite significant with, for the drag coefficient, a variation of +/- 7.2 % around the average while for 6.6 m/s, it is of +/- 3.6% and for 9.4 m/s it is of +/- 2.8%.

Figure 87 gives a better view of the previous results, with the force, the drag coefficient without the total area, the total area and the drag coefficient with the total area as a function of the body angle in the wind tunnel. This graph allows a better interpretation and comparison of the results with the literature.

Indeed, it is enough to see at a glance the minimum of the force at different wind speeds which is always at an angle of 170. It can also be seen that the higher the wind speed, the greater the difference between the values at different angles. Indeed, for a wind speed of 3.1 m/s, the force values hardly vary according to the angle, whereas the difference widens considerably for values of 9.3 m/s. The highest values seem to be at 240 degrees, which is consistent because these are the angles where the dummy is exposed to the wind over the largest area, since values of 90 or 270 degrees could not be taken. If such angles are to be calculated, it would therefore be logical that these values would have the highest force values.

The graph of C_D*A as a function of Reynolds number follows the same trend as the graph of C_D*A as a function of velocity, but with values much closer to C_D*A despite the differences in Reynolds number. The largest differences between the three curves are those at 240 degrees simply because for this degree only the value for a Re of $9.3*10^5$ is made. The slight differences in results between the three curves are due to the condition of the clamping screw on which the dummy is held and that did not allow some high-speed results to be taken as for the angle of 240 degrees. The same trend as for the force results is followed with smaller C_D*A values for angle of 170 or 350 degrees, and higher values that would be located at angles of 90 or 270 degrees if these measurements were taken.

The graph according to A_p shows that the above results follow a trend that is a function of their projected area. Indeed, forces and CD*A tend to increase and decrease with Ap. This shows that the results obtained follow a consistent trend.

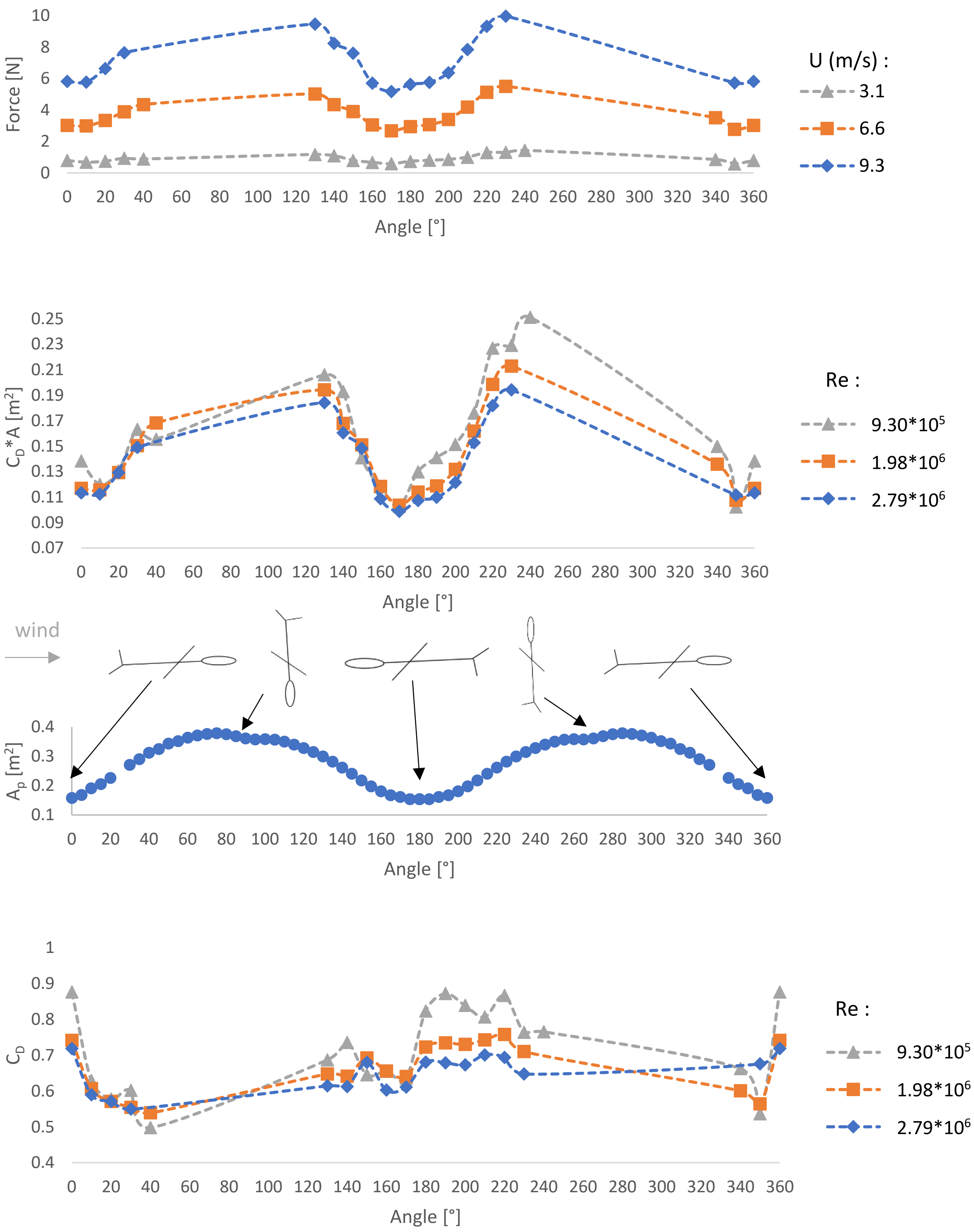

*Figure 87 - The results of F_{total}, C_D*A, A_p and C_D in comparison with the angle of the model for configuration 1, for a wind speed (U) of respectively 3.1, 6.6 and 9.3 m/s and for a Reynolds number (Re) of 930062, 1980132 and 2790186*

However, the graph of the C_D as a function of their Reynolds numbers does not follow the same trend. Indeed, once the total surface is added, the minimum values obtained are those at 40 and 350 degrees whereas the maximum values are rather 0 and 190 degrees. Once again, if the values around 90 and 270 degrees are achieved, they would probably correspond to the minimum drag coefficient. The values for a Reynolds coefficient of $9.3*10^5$ are the ones that show the most variation as a function of the model angle, which would tend to confirm that the values obtained for speeds of 3.1 m/s are not stable and that in future experiments it would be better to work at higher speeds. The drag coefficient curves for Reynolds of $1.98*10^6$ and $2.79*10^6$ seem to follow a more similar pattern, with slightly less consistent values for the 340 and 350 degrees angles, which can be explained by the fact that for these values, the dummy was moved, and therefore, they may not be representative.

Schmitt (1954) does the same kind of experiment on the human body in a wind tunnel. Indeed, one of its positions: the supine position, is more or less the same as the one used to obtain the results in Figure 87. However, he did not work with a single subject and these models vary from 1m62 to 1m88. It can therefore be assumed that the comparison of the dummy should be based on the maximum result of C_D obtained by Schmitt.

Comparing the results of C_D obtained in the wind tunnel with those available in Figure 88, it can be seen that the wind tunnel results are not in the same ranges of C_D. Indeed, the values of C_D obtained by Schmitt (1954) are rather situated between 1.5 and 4 depending on the angle. Our values are between 0.5 and 0.88. They are therefore 3 to 4 times smaller. However, the results obtained by Schmitt are for a speed of 27.49 m/s, which is 3 times higher than the maximum speed used in the wind tunnel. This could explain some of the differences in results, which would be related to insufficient speeds during the wind tunnel tests. Another main difference between this study and the papers of Schmitt (1954), is the fact that rather than using an estimated frontal area for each subject, he used a basic parameter which was vH/S (with v= volume, H= weight and S= surface area of the subjects) instead of Ap. This is the reason why these result curves are much more stable, with a regular trend, than those obtained for our models. And this could explain the difference in values between these results and those obtained in the wind tunnel.

Despite this, the trend seems to be confirmed. Indeed, the minimum values of the drag coefficient of the results in Figure 88 are those for 90 and 270 degrees, which is equivalent to the angle at which one would expect to obtain the smallest C_D in Figure 87. And conversely, the results are highest around 180 degrees.

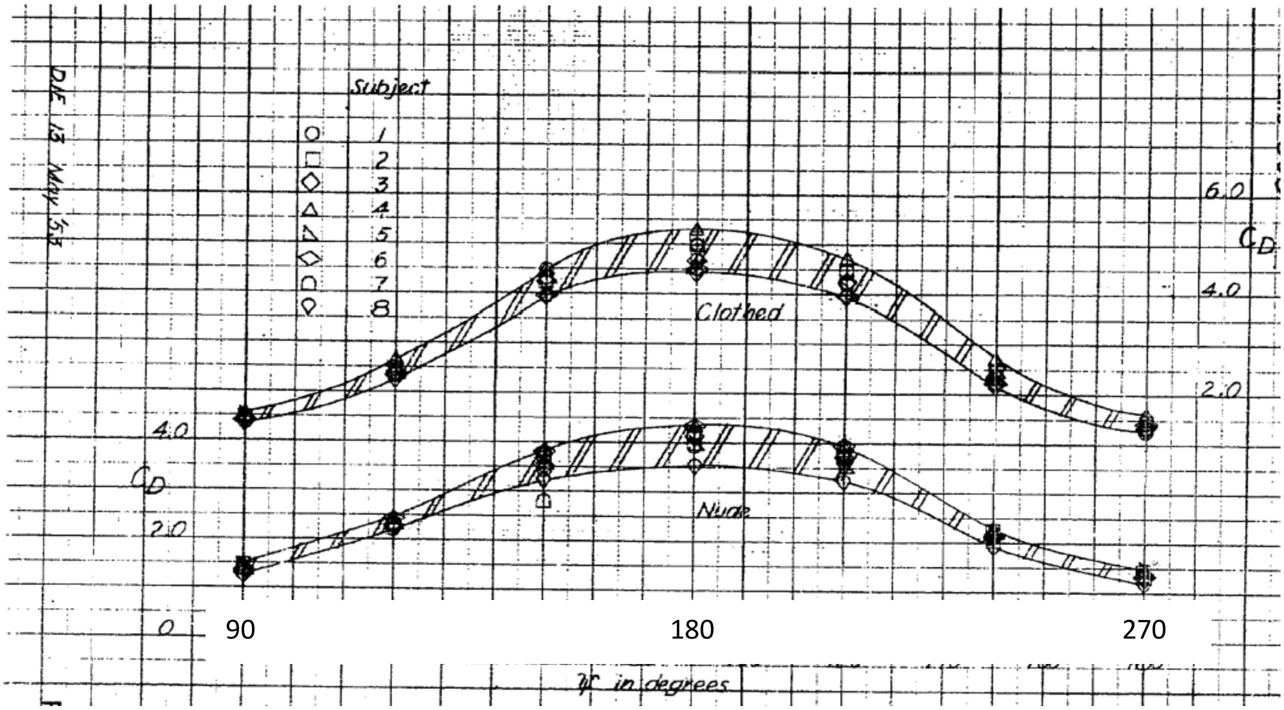

Figure 88 - Supine position, q=9 lb/ft² (Schmitt, 1954)

The C_DA of a model is performed by D'Auteuil et al. (2012) at different wind speeds (Figure 89). The speed of 9.3 m/sec done in the wind tunnel equals 33.48 km/h. The position of the model in this paper is very different from the position realised in the experimental process, so the results should be taken with caution. The range of C_DA for a static position varies from 0.09 to 0.1 (static position) in the article and from 0.09 to 0.25 in Figure 87. These values are therefore closer, with difference in value that can be explained by the fact that the results obtained by D'Auteuil et al. (2012) for the static position are made for a single angle position.

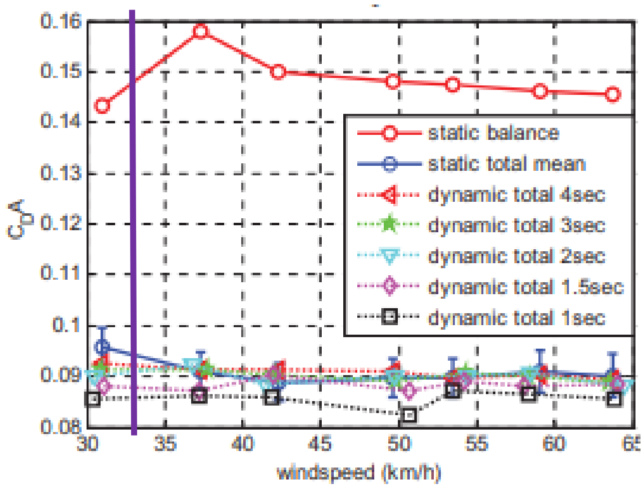

Figure 89 – Drag area coefficient from the integration of surface pressures in laminar flow with the C_DA for 33 km/h in purple (D'Auteuil et al., 2012)

More importantly, the results obtained in the article by D'Auteuil et al. (2012), suggests that speeds above 40 km/h are necessary to obtain more stable drag coefficient values, which could explain the quality of the results obtained in the wind tunnel and add to the total error that could occurred on the results.

If comparing the drag coefficient without the total projected surface area to those obtained in wind tunnel experiments with cyclists' models, the results seem to fit in (Table 11). Indeed, once again, the position of the model, lying down has a lower drag coefficient than the position of a cyclist on a bicycle but despite this, the range of values of the results is quite close to those acquired by different authors, especially for the high drag coefficient obtained.

Table 11 - Comparison of drag areas for several wind tunnel experiments for cyclist model (Defraeye et al., 2010) with the results obtain for the model

Author	Position	Wind speed [m/s]	Drag area (C_DA) [m^2]	Test section size [m^2]	Number of cyclists
Kyle and Burke (1984)	Hill descent	9 – 15.5	0.23	3*2.1	1
Dal Monte et al. et al. (1987)	Time trail	15	0.246 – 0.254	9.6*4.2	1
Broker et al. and Kyle (1995)	Time trail	13.3	0.203	/	5
Zdrakovic et al. (1996)	Time trail	+/- 8.2	0.17 – 0.23	2.2*1.6	2
Gilbertini et al. (2008)	Time trail, dynamics	13.9	0.223	4*3.84	1
Garcia-Lopez et al. et al. (2008)	Time trail	15	0.260	3*2.2	5
Results obtain in the wind tunnel of Liège	Lying down	3.1-9.4	0.09-0.25	2.5*1.8	1 (*not a cyclist !)

The results can also be compared to values coming from a skying techniques comparison from a recent paper (Ainegren et al., 2018). Indeed, in this article, the values of F_D, C_DA and C_D are given as well as their total projected surface (Table 12**Error! Not a valid bookmark self-reference.**). This allows comparison of some of the results obtained which are in the same range of projected surface area even though they are not in the same range of air velocity and if their positions are not similar.

Table 12 - Comparison of drag coefficient for skiing techniques with results obtain for the model in a lying down position (Ainegren et al., 2018) (Ta, Tb, Tc, Td = different downhill positions; available on Figure 11)

Position	Air velocity (m/s)	F_D [N]	C_DA [m^2]	A [m^2]	C_D
Ta	14	21.89	0.20	0.23	0.84
Tb	14	19.79	0.18	0.28	0.63
Tc	14	20.10	0.18	0.31	0.58
Td	14	25.60	0.23	0.37	0.62
30	3.1	0.93	0.16	0.23	0.72
	6.6	3.89	0.15		0.66
	9.3	7.65	0.15		0.69
40	3.1	0.89	0.15	0.27	0.58
	6.6	4.35	0.17		0.63
130	3.1	1.18	0.21	0.30	0.69
	6.6	5.02	0.19		0.65
	9.3	9.46	0.18		0.61
230	3.1	1.31	0.23	0.30	0.76
	6.6	5.51	0.21		0.71
	9.3	9.97	0.19		0.65
240	3.1	1.43	0.25	0.36	0.69

As it can be clearly seen in Figure 90, the results obtained for the different skiing methods show quite similar results in terms of drag coefficient to those obtained in the wind tunnel despite the inaccuracies that have already been discussed above. This comparison seems to confirm that the results obtained in the wind tunnel for a given total projected surface can be quite similar, although these results are obviously not perfectly identical. This can be explained simply by the fact that despite this projected surface, the whole hidden part behind this surface also interacts with the wind and can be very different between the skiing methods and the position of our model position.

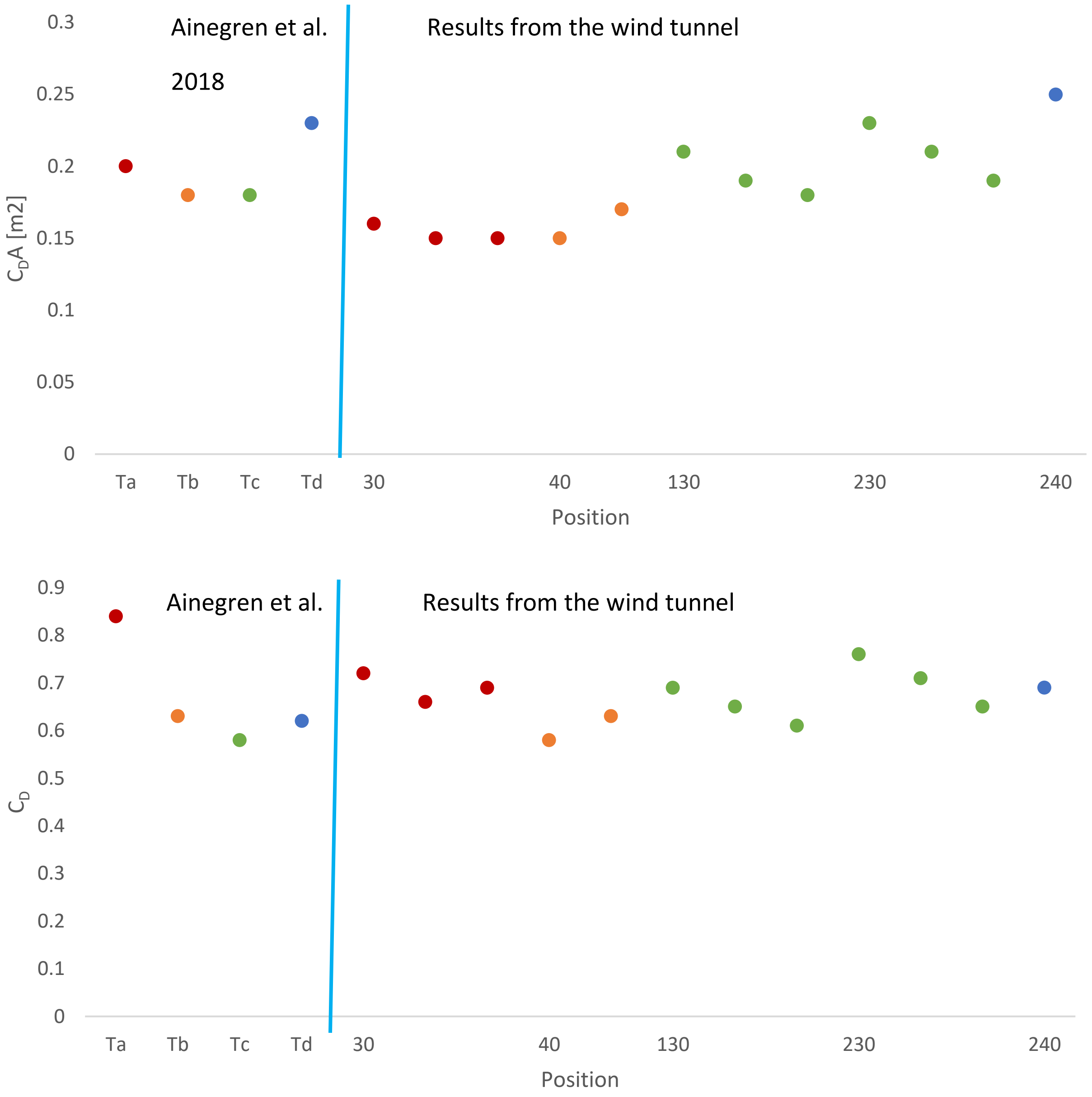

Figure 90 - C_DA and C_D in function of the position

5. Improvements

5.1. Numerical modeling

The numerical modelling of the model is well advanced in this dissertation, but despite this, the exact total surface of the model could never be obtained, even though it is known to be below the threshold of 2.241 m^2. Two methods can be explored in the future to obtain a more accurate result.

The first method is already a little bit discussed in Section 3.2.4 and consist in comparing the model (Ken) with other models where the total surface of the mesh is known (such as the screw). It is best to find a set of models that are rather humanoid shape so that the comparison is as reliable as possible. Given the use of this type of numerical modelling in various domains, including video games, it should be possible to find this type of mesh in database (Figure 91). An accurate percentage error can then be assessed and the total surface area of Ken can be adapted according to these results. However, this method is not ideal as the total surface area is still an approximation and will not be exact.

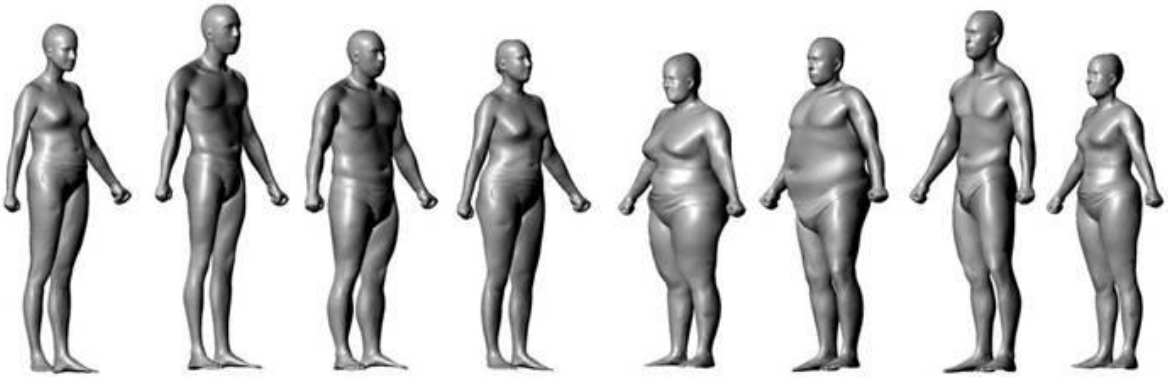

Figure 91 - Human dataset of Caesar data set (Khan, 2018)

The second way to obtain this value, is to obtain a continuous mesh without any holes or overlay on the model. The software used in this dissertation are not enough to achieve this goal but combination of Blender and another software named Metashape, can eventually lead to the desired result. Indeed, the *close holes* parameter of Metashape is quite advanced, allowing for example to close the holes on a particular selected region. Another tool that is available on Metashape and not on Cloud Compare is the *extrapolated* parameter on the *build mesh dialog* that allows to generate the surface already without any holes, leading to a closed mesh.

Another point that can be improved concerns the modeling of the limbs which are not perfectly identical on the right and on the left of the model and which can also be improved by using metashape or another software.

5.2. Experimental modeling

As discussed in Section 4.1.1, the placement of the model in the wind tunnel still needs to be improved. Indeed, the notched piece used to lock the ball joint is easily breakable (Figure 92). The handling of the mannequin then becomes tricky as it requires extreme delicacy and changing the broken parts requires a certain amount of time that cannot be devoted to collecting data. To avoid this inconvenience, the part must either be made of a more resistant material or even redesigned to better withstand the weight of the model.

Another solution is to take or build a 100% rigid model like the one used in the paper by d'Auteuil et al. (2012) and perform the wind tunnel tests with this rigid model. But this limits the configurations in which the mannequin can be placed, unless several rigid models are created.

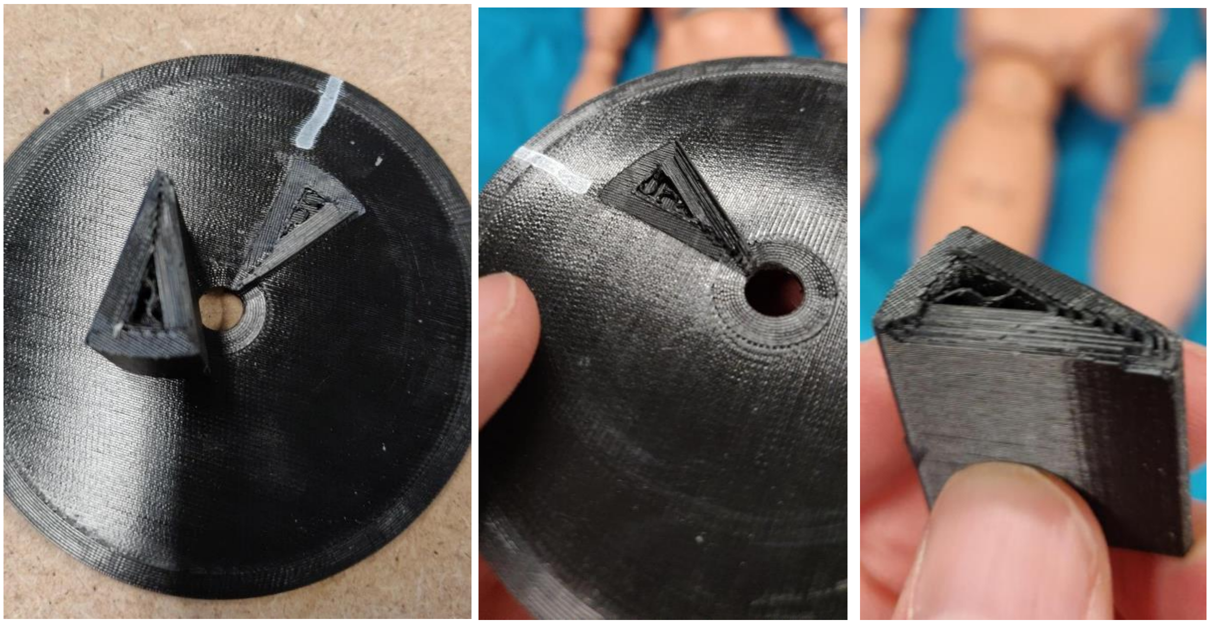

Figure 92 – Break of the notched piece

In order to be able to compare the set-up of the model in the wind tunnel with the literature articles, wind tunnel tests can be carried out with the model in positions similar to those described in Section 4.2.2. The difficulty with this installation is to maintain the model in the desired positions but also to obtain the total projected surface of those positions.

An alternative is to test the set up with more smaller parts of the body model such as the arm or the leg. Indeed, several articles focusing on particular body parts are available such as the paper by Gardano et al. (2006) which focuses on the arm or Pöyhönen et al. (2000) which focuses on the leg and foot. The advantage is that the projected surface for the different body parts is available from the modeling performed on the mannequin. The disadvantage is that the drag coefficient of these results is lower than the whole-body coefficient.

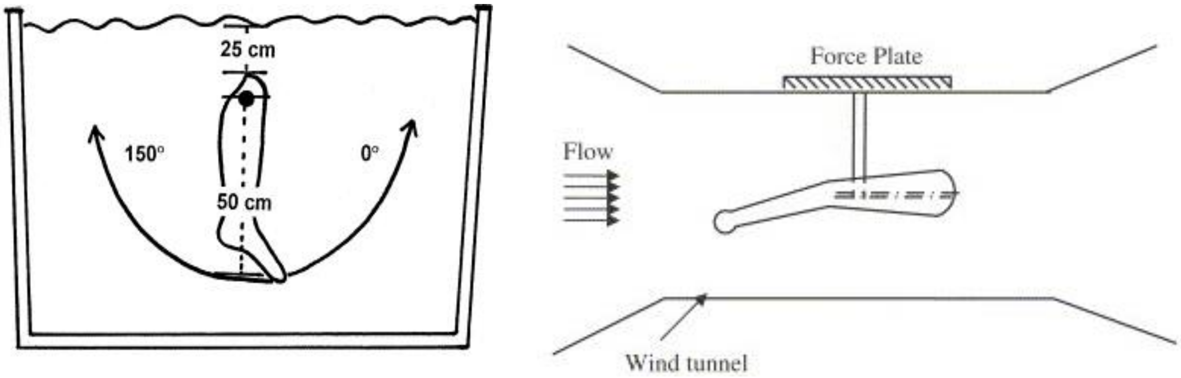

Figure 93 – Illustration of a leg in a water tank (Pöyhönen et al., 2000) on the left and illustration of an arm on a wind tunnel (Gardano, 2006) on the right

The configuration 3 (reference for a drowned body) should fit well to comparisons with articles focusing on the drag coefficient of cyclists and skiers, for certain position. It would be interesting to see if a position closer to that of the papers can be tested before conducting test on configuration 3 to validate the set-up.

In addition to the different positions to be tested in the wind tunnel, it is necessary to test the impact of clothing on the results.

According to the results obtained previously, the wind speed in the wind tunnel should be chosen carefully. Either a higher wind speed improves the quality of the results, or the setup should give a more accurate wind speed in order to obtain lower uncertainties. The acquisition time can also be a little longer, but this does not change the results very much since the moving averages of the force converge for the chosen acquisition time in this configuration.

6. Conclusion

This work is a contribution to the search for victims of drowning in urban area, by the calibration and validation of a full-scale experimental model. The two essential parameters among others for such a model are identified as the projected area and the drag coefficient.

To obtain the projected surface area of the full-scale model, two acquisitions are conducted, using a laser scanning method and photogrammetry. These acquisitions are made on the model in an upright position (named configuration 1). Then, using multiple software's including Cloud Compare, a numerical 3D model of the full-scale model is processed. This model can be adjusted according to the desired configuration of the full-scale model in order to be adaptable to experiments. The resulting mesh allows to obtain projected surface area by using a MATLAB routine, for any x, y, z angles. This permits to establish an initial database.

Then, experiments are conducted in a wind tunnel section of 4.5 m^2, reproducing the condition under which a drowned victim would be. The model is modified so that it can be placed on an aerodynamic balance to measure the forces acting on it and the wind speed is measured by an anemometer. Measurements are conducted for a frequency of 200 Hz.

These experiments give the followings results:

1. The force is higher for higher projected surface area. It is then minimum for an angle of 0 and 180 degrees and maximum for an angle of 90 and 270 degrees.
2. The C_D*A is between the range of 0.09 and 0.25. And the drag coefficient (C_D) is between the range of 0.5 and 0.88 for Reynolds numbers comprised between $0.9*10^5$ and $3*10^6$.
3. For a Reynolds number of $0.9*10^5$, the drag coefficient results are of poor quality, with higher uncertainties than the drag coefficient results for higher Reynolds numbers.
4. The drag coefficient is maximum for an angle of 0 and 180 degrees and minimum for an angle of 90 and 270 degrees, this is the opposite of the trend of forces as a function of the projected surface area.

This wind tunnel experiment provides a first estimation of the drag coefficient values of the full-scale model. These values are compared to other literature results originating from various fields such as cycling, skiing or skating.

This experiment could be improved by adapting the speed of the wind to obtain more stable drag coefficient, and be applied to more different projected area. Different positions of the model that can be compared to literature should also be applied. Once these modifications performed and the setup of the experiment validated, more experiment should be conducted for the configuration of a body in the same position as a drowned victim, with and without clothes.

Bibliography

Ainegren, M., & Jonsson, P. (2018). Drag area, frontal area and drag coefficient in cross-country skiing techniques. *Multidisciplinary Digital Publishing Institute Proceedings*, *2*(6), 313.
Berchon, M., & Luyt, B. (2014). *L'impression 3D*. Editions Eyrolles.

Bixler B, Pease D, Fairhurst F (2007) The accuracy of computational fluid dynamics analysis of the passive drag of a male swimmer. Sports Biomech 6(1): 81–98

Bonamy-Cossard, T. (2021). Évaluation de la surface frontale comme élément d'amélioration de l'aérodynamisme en cyclisme.

Broker, J.P., Kyle, C.R., 1995. Pursuit Aerodynamics, Project 96: wind tunnel test results. USOC Sport Science and Technology Report, Colorado Springs, pp. 1–46 (from Basset et al.., 1999)

Debraux, P., Bertucci, W., Manolova, A. V., Rogier, S., & Lodini, A. (2009). New method to estimate the cycling frontal area. International journal of sports medicine, 30(04), 266-272.

Carniel, S., Umgiesser, G., Sclavo, M., Kantha, L. H., & Monti, S. (2002). Tracking the drift of a human body in the coastal ocean using numerical prediction models of the oceanic, atmospheric and wave conditions. *Science & Justice*, *42*(3), 143-151.

Clarys, J. P. (1979). Human morphology and hydrodynamics. *Swimming III*, *8*, 3-41.

CRED. 2021 Disasters in numbers. Brussels: CRED; 2022 ;
https://cred.be/sites/default/files/2021_EMDAT_report.pdf

CRED. 2022, The International Disaster Database EM-DAT : Disasters of the week, https://www.emdat.be/, accessed on 17 August.

Dal Monte, A., Leonardi, L.M., Menchinelli, C., Marini, C., 1987. A new bicycle design based on biomechanics and advanced technology. International Journal of Sport Biomechanics 3, 287–292

D'Auteuil, A., Larose, G. L., & Zan, S. J. (2012). The effect of motion on wind tunnel drag measurement for athletes. *Procedia Engineering*, *34*, 62-67.

Defraeye, T., Blocken, B., Koninckx, E., Hespel, P., & Carmeliet, J. (2010). Aerodynamic study of different cyclist positions: CFD analysis and full-scale wind-tunnel tests. Journal of biomechanics, 43(7), 1262-1268.

Delhez, C. (2021). Hydrodynamic characterisation of a body-like shape: a contribution to guide the search for victims of drowning in rivers.

Donoghue, E. R., & Minnigerode, S. C. (1977). Human body buoyancy: a study of 98 men. *Journal of Forensic Science*, *22*(3), 573-579.

Ebbesmeyer, C. C., & Haglund, W. D. (1994). Drift trajectories of a floating human body simulated in a hydraulic model of Puget Sound. *Journal of Forensic Science*, *39*(1), 231-240.

Fanger PO. (1970) Thermal comfort. Copenhagen: Danish Technical Press.

Farrugia, A., & Ludes, B. (2011). Diagnostic of Drowning in Forensic Medicine. In (Ed.), Forensic Medicine - From Old Problems to New Challenges. IntechOpen. https://doi.org/10.5772/19234

Gatta, G., Cortesi, M., Fantozzi, S., & Zamparo, P. (2015). Planimetric frontal area in the four swimming strokes: Implications for drag, energetics and speed. *Human movement science*, *39*, 41-54.

Garcia-Lopez, J., Rodriguez-Marroyo, J.A., Juneau, C.E., Peleteiro, J., Martinez, A.C.,Villa, J.G., 2008. Reference values and improvement of aerodynamic drag in professional cyclists. Journal of Sports Sciences 26 (3), 277–286.

Gardano P, Dabnichki P (2006) On hydrodynamics of drag and lift of the human arm. J Biomech 39: 2767–2773.

Ghaffarian, H., Lopez, D., Mignot, E., Piegay, H., and Riviere, N. (2020). Dynamics of floating objects at high particulate reynolds numbers. 5(5):054307.

Gibertini, G., Campanardi, G., Grassi, D., Macchi, C., 2008. Aerodynamics of biker position, Proceedings of the BBAA VI International Colloquium on: Bluff Bodies Aerodynamics and Applications.

Girardeau-Montaut, D. (2015). CloudCompare version 2.6. 1 user manual. *On line at: http://www. danielgm. net/cc/doc/qCC/CloudCompare% 20v2*, *6*, 20.

Heil, D. P. (2002). Body mass scaling of frontal area in competitive cyclists not using aero-handlebars. *European journal of applied physiology*, *87*(6), 520-528.

Huilier D. (2010), Introduction à la viscosité dynamique et cinématique, http://www.daniel-huilier.fr/Enseignement/Notes_Cours/Viscosite/Introduction_Viscosite.pdf

Kazhdan, M., Bolitho, M., & Hoppe, H. (2006, June). Poisson surface reconstruction. In *Proceedings of the fourth Eurographics symposium on Geometry processing* (Vol. 7).

Keys A, Fidanza F, Karvonen MJ, Kimura N, Taylor HL. Indices of relative weight and obesity. J Chronic Dis. 1972 Jul 1;25(6):329–343

Kyle, C.R., Burke, E.R., 1984. Improving the racing bicycle. Mechanical Engineering 106 (9), 34–45.

Leïca Geosystems AG (2018). Manuel de l'utilisateur Leica BLK 360, version 2.0, https://shop.leica-geosystems.com/sites/default/files/2019-04/866562_leica_blk360_um_v2.0.0_fr.pdf

Lukes, R. A., Chin, S. B., & Haake, S. J. (2005). The understanding and development of cycling aerodynamics. *Sports engineering*, *8*(2), 59-74.

Lunetta, P., Ebbesmeyer, C., & Molenaar, J. (2014). Behaviour of dead bodies in water. In *Drowning* (pp. 1149-1152). Springer, Berlin, Heidelberg.

Marinho DA, Reis VM, Alves FB, Vilas-Boas JP, Machado L, Silva AJ, Rouboa AI (2009a) The hydrodynamic drag during gliding in swimming. J Appl Biomech 25(3): 253-257.

Marinho DA, Reis VM, Alves FB, Vilas-Boas JP, Machado L, Rouboa AI, Silva AJ (2009b) The use of Computational Fluid Dynamics in swimming research. Int J Comput Vis Biomech (in press)

Marinho, D. A., Barbosa, T. M., Kjendlie, P. L., Vilas-Boas, J. P., Alves, F. B., Rouboa, A. I., & Silva, A. J. (2009c). Swimming simulation: a new tool for swimming research and practical applications. In *Computational fluid dynamics for sport simulation* (pp. 33-61). Springer, Berlin, Heidelberg.

Marrone, M., Ferorelli, D., Stellacci, A., & Vinci, F. (2021). A fatal drowning filmed in a private pool: Analysis of the sequences of submersion. *Forensic science international: reports*, *3*, 100189.

Mateus M. and Vieira V., « Study on the postmortem submersion interval and accumulated degree days for a multiple drowning accident », Forensic Science International, may 2014, vol. 238, pp. e15-e19

Mikhail, E. M., Bethel, J. S., & McGlone, J. C. (2001). *Introduction to modern photogrammetry*. John Wiley & Sons.

Mollendorf, J. C., Termin, A. C., Oppenheim, E. R. I. C., & Pendergast, D. R. (2004). Effect of swim suit design on passive drag. *Medicine and science in sports and exercise*, *36*(6), 1029-1035.

Morais, J. E., Sanders, R. H., Papic, C., Barbosa, T. M., & Marinho, D. A. (2020). The influence of the frontal surface area and swim velocity variation in front crawl active drag. *Medicine & Science in Sports & Exercise*, *52*(11), 2357-2364.

Nabi, R. M., Azad, R., Saeed, S., & Nabi, R. M. (2017). Optimization Algorithm's Problems: Comparison Study. *Kurdistan Journal of Applied Research*, *2*(3), 25-31.

Nenad T., Novakovic P., Hornak M. (2017). Virtual reconstruction and computer visualizations in archaeological practice, vol IV, (pp. 90-91)

North, R. (2002). The pathophysiology of drowning.

Nucara, A., Pietrafesa, M., Rizzo, G., & Scaccianoce, G. (2012). An anthropometric analysis of seated and standing people. In *Handbook of Anthropometry* (pp. 91-114). Springer, New York, NY.

Olds, T. S., Norton, K. I., Lowe, E. L., Olive, S., Reay, F., & Ly, S. (1995). Modeling road-cycling performance. *Journal of applied physiology*, *78*(4), 1596-1611.

Persi, E., Petaccia, G., Sibilla, S., Brufau, P., and García-Navarro, P. (2019). Calibration of a dynamic eulerian-lagrangian model for the computation of wood cylinders transport in shallow water flow. Journal of Hydroinformatics, 21(1):164–179. Copyright - Copyright IWA Publishing Jan 2019; Dernière mise à jour - 2020-09-11

Pöyhönen, T., Keskinen, K. L., Hautala, A., & Mälkiä, E. (2000). Determination of hydrodynamic drag forces and drag coefficients on human leg/foot model during knee exercise. *Clinical biomechanics*, *15*(4), 256-260.

Robinette, K. M., Daanen, H., & Paquet, E. (1999, October). The CAESAR project: a 3-D surface anthropometry survey. In *Second international conference on 3-D digital imaging and modeling (cat. No. PR00062)* (pp. 380-386). IEEE.

Sampson, B., Hammers, J., & Stram, M. (2022). Forensic aspects of cardiovascular pathology. In *Cardiovascular Pathology* (pp. 911-940). Content Repository Only!.

Schmitt, T. J. (1954). *Wind-tunnel investigation of air loads on human beings*. DAVID TAYLOR MODEL BASIN WASHINGTON DC.

Stylianidis, E. (2020). Measurements: Introduction to Photogrammetry. In *Photogrammetric Survey for the Recording and Documentation of Historic Buildings* (pp. 139-195). Springer, Cham.

Tanabe, S. I., Narita, C., Ozeki, Y., & Konishi, M. (2000). Effective radiation area of human body calculated by a numerical simulation. Energy and buildings, 32(2), 205-215.

Tayeb G. (2013) Comptage dex pixels de couleur identique sur une image. Application à la mesure de surfaces complexes, https://tayeb.fr/misc/calcul_surfaces/index.htm#principe, dernière mise à jour 2021

Thermexcel (2001), masse volumique de l'air humide,
https://www.thermexcel.com/french/tables/massair.htm, accessed on August 2022

Tikuisis, P., Meunier, P., and Jubenville, C. (2001). Human body surface area: Measurement and prediction using three-dimensional body scans. 85:264–71.

Tokkari, N., Verdaasdonk, R. M., Liberton, N., Wolff, J., Den Heijer, M., Van Der Veen, A., & Klaessens, J. H. (2017, February). Comparison and use of 3D scanners to improve the quantification of medical images (surface structures and volumes) during follow up of clinical (surgical) procedures. In *Advanced Biomedical and Clinical Diagnostic and Surgical Guidance Systems XV* (Vol. 10054, p. 100540Z). International Society for Optics and Photonics.

Tomia and Liftarn (2007) Wind tunnel,
https://upload.wikimedia.org/wikipedia/commons/0/0f/Windtunnel3-en.svg, accessed on 1st August 2022

Virtanen, J. P., Hyyppä, H., Kurkela, M., Vaaja, M., Alho, P., & Hyyppä, J. (2014). Rapid prototyping—A tool for presenting 3-dimensional digital models produced by terrestrial laser scanning. ISPRS International Journal of Geo-Information, 3(3), 871-890.

Winkler, S., & Min, D. (2011, December). Stereoscopic image quality compendium. In *2011 8th International Conference on Information, Communications & Signal Processing* (pp. 1-5). IEEE.

World Health Organization. The World Health Report, 2002: Reducing risks, promoting healthy life, Geneva, World Health Organization, 2002.

Zaidi H, Taiar R, Fohanno S, Polidori G (2008) Analysis of the effect of swimmer's head position on swimming performance using computational fluid dynamics. J Biomech 41: 1350–1358.

Zdravkovic, M.M., Ashcroft, M.W., Chisholm, S.J., Hicks, N., 1996. Effect of cyclist's posture and vicinity of another cyclist on aerodynamic drag. In: Haake, S.J.(Ed.), The Engineering of Sport. Balkema, Rotterdam 21-28.

Appendix

Numerical appendix

Table 13 - Projected surfaces for configuration 1 with variation along the x-axis for main positions

configuration 1				m^2					
x	z	y	Numbers of pixels	Total surface	torso	Left leg	Right leg	Left arm	Right arm
-90	0	-180	179118	0.36194	0.14413	0.11506	0.02607	0.07668	0.00000
-90	0	-135	269148	0.54387	0.19585	0.11910	0.09909	0.07318	0.05665
-90	0	-90	299210	0.60461	0.25179	0.10720	0.10430	0.07094	0.07039
-90	0	-45	291252	0.58767	0.22139	0.10527	0.11170	0.06376	0.08556
-90	0	0	177689	0.35906	0.12214	0.02249	0.10258	0.01428	0.09757
-90	0	45	270105	0.54580	0.20184	0.10487	0.11942	0.02987	0.08980
-90	0	90	298857	0.60390	0.24795	0.10774	0.10605	0.07504	0.06712
-90	0	135	289679	0.58492	0.23086	0.10546	0.11350	0.07391	0.06119
-90	0	180	179117	0.36194	0.14413	0.11506	0.02607	0.07668	0.00000

Table 14 - Projected surfaces for configuration 1 with variation along the x-axis for different positions

configuration 1				m^2					
x	z	y	Numbers of pixels	Total surface	torso	Left leg	Right leg	Left arm	Right arm
-90	0	-165	165831	0.33515	0.12622	0.10379	0.01599	0.07956	0.00959
-90	0	-150	59797	0.45156	0.15178	0.10715	0.07008	0.08206	0.04232
-90	0	-120	79928	0.60357	0.23431	0.12242	0.11234	0.07234	0.06217
-90	0	-105	301483	0.60931	0.24642	0.11372	0.11037	0.07291	0.06588
-90	0	-75	293197	0.59256	0.24790	0.10008	0.10488	0.06756	0.07214
-90	0	-60	79560	0.59859	0.24173	0.10199	0.11040	0.06594	0.07853
-90	0	-30	74342	0.55934	0.19208	0.09785	0.11777	0.05958	0.09205
-90	0	-15	230710	0.46627	0.14563	0.06814	0.10859	0.04722	0.09670
-90	0	15	172386	0.34840	0.12377	0.01524	0.11296	0	0.09643
-90	0	30	61007	0.45901	0.16863	0.07093	0.12338	0.00297	0.09426
-90	0	60	80228	0.60362	0.23064	0.11742	0.11918	0.05245	0.08394
-90	0	75	300527	0.60737	0.24130	0.11321	0.11344	0.06240	0.07703
-90	0	105	293965	0.59411	0.24762	0.10350	0.10644	0.06552	0.07104
-90	0	120	79467	0.59789	0.24558	0.10464	0.10978	0.06922	0.06868
-90	0	150	73793	0.55520	0.21993	0.11564	0.10305	0.07376	0.04283
-90	0	165	232748	0.47039	0.19122	0.12008	0.07837	0.07246	0.00826

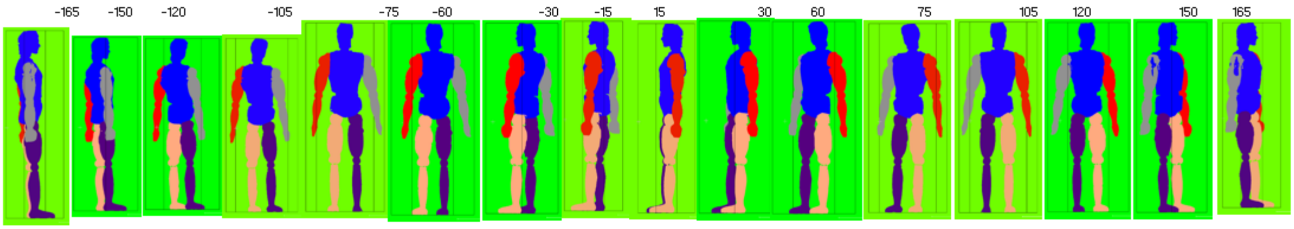

Figure 94 - Position of the model for configuration 1, with rotation along the x-axis

Table 15 - Projected surfaces for configuration 1 with variation along the x-axis for main positions

configuration 1				m²					
x	z	y	Numbers of pixels	Total surface	torso	Left leg	Right leg	Left arm	Right arm
180	0	0	76320	0.15422	0.04090	0.03491	0.03494	0.02158	0.02189
135	0	0	139639	0.28217	0.10193	0.09415	0.04256	0.04353	0.00000
90	0	0	178783	0.36127	0.14404	0.11501	0.02593	0.07628	0.00000
45	0	0	160912	0.32516	0.13853	0.08718	0.03163	0.06781	0.00000
0	0	0	78055	0.15773	0.08800	0.01310	0.01121	0.02157	0.02384
-45	0	0	141162	0.28525	0.11778	0.01635	0.06816	0.00187	0.08295
-90	0	0	177689	0.35906	0.12214	0.02259	0.10248	0.01428	0.09757
-135	0	0	159327	0.32195	0.09000	0.04832	0.10111	0.02147	0.06105
-180	0	0	76314	0.15422	0.04090	0.03491	0.03494	0.02158	0.02189

Table 16 - Projected surfaces for configuration 1 with variation along the x-axis for different positions

configuration 1				m²					
x	z	y	Numbers of pixels	Total surface	torso	Left leg	Right leg	Left arm	Right arm
-175	0	0	83235	0.16819	0.04477	0.04381	0.03919	0.02167	0.01875
-170	0	0	25121	0.18901	0.05112	0.04884	0.04793	0.02161	0.01951
-160	0	0	29650	0.22308	0.06247	0.04980	0.06151	0.02090	0.02839
-155	0	0	118834	0.24012	0.06624	0.04962	0.06882	0.02070	0.03474
-145	0	0	140274	0.28344	0.07688	0.05004	0.08632	0.02194	0.04827
-140	0	0	40264	0.30294	0.08312	0.04951	0.09523	0.02031	0.05478
-130	0	0	44979	0.33841	0.09798	0.04794	0.10492	0.02065	0.06693
-125	0	0	173864	0.35132	0.10512	0.04601	0.10697	0.02068	0.07254
-115	0	0	183117	0.37002	0.11585	0.04347	0.10846	0.01952	0.08272
-110	0	0	49757	0.37436	0.11874	0.04067	0.10979	0.01794	0.08721
-100	0	0	49044	0.36900	0.12178	0.03230	0.10533	0.01578	0.09381
-95	0	0	180228	0.36418	0.12194	0.02715	0.10379	0.01538	0.09591
-85	0	0	176378	0.35640	0.12143	0.02245	0.10092	0.01288	0.09873
-80	0	0	47236	0.35539	0.12223	0.02299	0.09996	0.01073	0.09949
-70	0	0	46276	0.34817	0.12535	0.02417	0.09366	0.00672	0.09828
-65	0	0	168201	0.33988	0.12504	0.02393	0.08959	0.00515	0.09616

-55	0	0	157676	0.31861	0.12458	0.02042	0.07898	0.00370	0.09093
-50	0	0	40398	0.30395	0.12189	0.01818	0.07358	0.00274	0.08756
-40	0	0	35416	0.26744	0.11469	0.01325	0.06080	0	0.07869
-35	0	0	121099	0.24470	0.10707	0.01115	0.05389	0	0.07259
-25	0	0	102111	0.20633	0.09604	0.00836	0.03877	0.00400	0.05916
-20	0	0	24998	0.18808	0.09206	0.00727	0.03067	0.00549	0.05259
-10	0	0	21961	0.16523	0.08819	0.00684	0.02107	0.01056	0.03856
-5	0	0	78238	0.15809	0.08576	0.00884	0.01784	0.01472	0.03093
5	0	0	83136	0.16799	0.08829	0.02192	0.01246	0.02719	0.01813
10	0	0	25333	0.19060	0.09494	0.03277	0.01454	0.03299	0.01537
20	0	0	30059	0.22616	0.10089	0.05226	0.01771	0.04592	0.00937
25	0	0	68137	0.13768	0.05912	0.05112	0.00397	0.02143	0.00204
35	0	0	143587	0.29014	0.12571	0.07565	0.02772	0.06106	
40	0	0	41347	0.31223	0.13434	0.08331	0.02918	0.06540	
50	0	0	45440	0.34314	0.14581	0.09349	0.03225	0.07087	0.00072
55	0	0	174310	0.35222	0.14693	0.09687	0.03420	0.07292	0.00130
65	0	0	183536	0.37086	0.14855	0.10493	0.03592	0.07722	0.00424
70	0	0	50063	0.37666	0.14900	0.10921	0.03617	0.07833	0.00395
80	0	0	49852	0.37508	0.14869	0.11380	0.03213	0.07840	0.00205
85	0	0	182364	0.36849	0.14607	0.11412	0.02956	0.07753	0.00122
95	0	0	176978	0.35761	0.14056	0.11437	0.02823	0.07445	
100	0	0	47688	0.35880	0.13749	0.11750	0.03173	0.07208	
110	0	0	46591	0.35054	0.13012	0.11508	0.03937	0.06598	
115	0	0	168124	0.33972	0.12497	0.11165	0.04078	0.06231	
125	0	0	155971	0.31516	0.11526	0.10520	0.04099	0.05371	
130	0	0	39856	0.29987	0.10952	0.10030	0.04094	0.04910	
140	0	0	34823	0.26200	0.09292	0.08819	0.04298	0.03792	
145	0	0	119020	0.24050	0.08356	0.08081	0.04329	0.03283	
155	0	0	97844	0.19771	0.06656	0.06614	0.04121	0.02165	0.00215
160	0	0	23992	0.18051	0.06126	0.05994	0.03974	0.01713	0.00244
170	0	0	21500	0.16176	0.04356	0.04590	0.04586	0.01458	0.01187
175	0	0	76058	0.15369	0.04087	0.03583	0.04162	0.01582	0.01956

Table 17 - Projected surfaces for configuration 1 with variation along the x-axis for different positions

configuration 1				m^2					
x	z	y	Numbers of pixels	Total surface	torso	Left leg	Right leg	Left arm	Right arm
-165	0	0	100902	0.20393	0.05783	0.04894	0.05436	0.02106	0.02174
-150	0	0	34871	0.26236	0.07096	0.05080	0.07767	0.02153	0.04140
-120	0	0	48186	0.36254	0.11144	0.04476	0.10865	0.01977	0.07792
-105	0	0	185171	0.37424	0.12023	0.03827	0.10779	0.01745	0.09050
-75	0	0	174944	0.35357	0.12315	0.02531	0.09671	0.00953	0.09888
-60	0	0	43895	0.33026	0.12589	0.02122	0.08492	0.00403	0.09419

-30	0	0	30189	0.22714	0.10241	0.00939	0.04675	0.00201	0.06658
-15	0	0	84933	0.17165	0.08670	0.00761	0.02344	0.00814	0.04576
15	0	0	101686	0.20551	0.09511	0.04233	0.01637	0.03973	0.01197
30	0	0	36053	0.27126	0.12049	0.06897	0.02433	0.05690	0.00056
60	0	0	48383	0.36402	0.14932	0.10202	0.03460	0.07575	0.00234
75	0	0	187357	0.37865	0.14827	0.11065	0.03505	0.07786	0.00341
105	0	0	174629	0.35703	0.13433	0.11500	0.03764	0.07006	0
120	0	0	43618	0.32817	0.12114	0.10961	0.04012	0.05731	0
150	0	0	28979	0.21803	0.07500	0.07349	0.04226	0.02729	0
165	0	0	82821	0.16738	0.05484	0.05257	0.04190	0.01401	0.00407

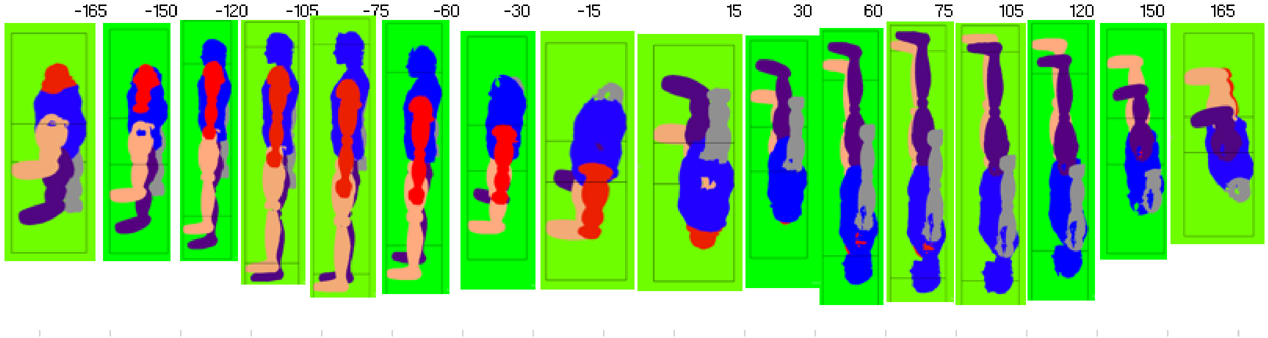

Figure 95 - Position of the model for configuration 1, with rotation along the x-axis

Table 18 - Projected surfaces for configuration 2 with variation along the x-axis for main positions

configuration 2				m^2					
x	z	y	Numbers of pixels	Total surface	torso	Left leg	Right leg	Left arm	Right arm
-90	0	180	47625	0.35443	0.17411	0.12589	0.02666	0.02776	0.00000
-90	0	135	78998	0.58791	0.24935	0.11116	0.11572	0.05718	0.05451
-90	0	90	83742	0.62321	0.25765	0.11096	0.10877	0.07049	0.07534
-90	0	45	76906	0.57234	0.22988	0.10644	0.12566	0.04593	0.06443
-90	0	0	47771	0.35551	0.16051	0.02248	0.12970	0.00097	0.04185
-90	0	-45	78141	0.58153	0.24370	0.10680	0.11531	0.05238	0.06333
-90	0	-90	83603	0.62218	0.26090	0.11114	0.10584	0.07063	0.07367
-90	0	-135	76669	0.57057	0.23669	0.12811	0.10070	0.05581	0.04927
-90	0	-180	47938	0.35676	0.16055	0.02311	0.13022	0.00092	0.04195

Table 19 - Projected surfaces for configuration 2 with variation along the x-axis for different positions

configuration 2				m^2					
x	z	y	Numbers of pixels	Total surface	torso	Left leg	Right leg	Left arm	Right arm
-90	0	-165	231600	0.46276	0.19735	0.06906	0.12590	0.02298	0.04747
-90	0	-150	72405	0.54878	0.22825	0.10204	0.12419	0.03997	0.05433
-90	0	-120	83043	0.62026	0.25532	0.12381	0.11393	0.06473	0.06246
-90	0	-105	312356	0.62412	0.25877	0.11520	0.11092	0.06975	0.06949
-90	0	-75	300197	0.61004	0.25829	0.10343	0.10799	0.06796	0.07238
-90	0	-60	80595	0.60197	0.25511	0.10375	0.11223	0.06180	0.06908
-90	0	-30	73168	0.54452	0.22953	0.09946	0.12040	0.03897	0.05616
-90	0	-15	232639	0.47275	0.20191	0.07138	0.12793	0.02330	0.04824
-90	0	15	183567	0.37303	0.17484	0.01575	0.13003	0.00629	0.04612
-90	0	30	64839	0.48253	0.20170	0.07177	0.12490	0.02894	0.05522
-90	0	60	83145	0.61877	0.24735	0.11950	0.12099	0.05974	0.07118
-90	0	75	313651	0.63738	0.25761	0.11687	0.11724	0.06976	0.07591
-90	0	105	302108	0.61392	0.25688	0.10675	0.10989	0.06891	0.07148
-90	0	120	80720	0.60072	0.25449	0.10604	0.11147	0.06385	0.06486
-90	0	150	73092	0.54395	0.23339	0.11764	0.10494	0.04783	0.04015
-90	0	165	234048	0.47562	0.21349	0.12392	0.08100	0.03589	0.02132

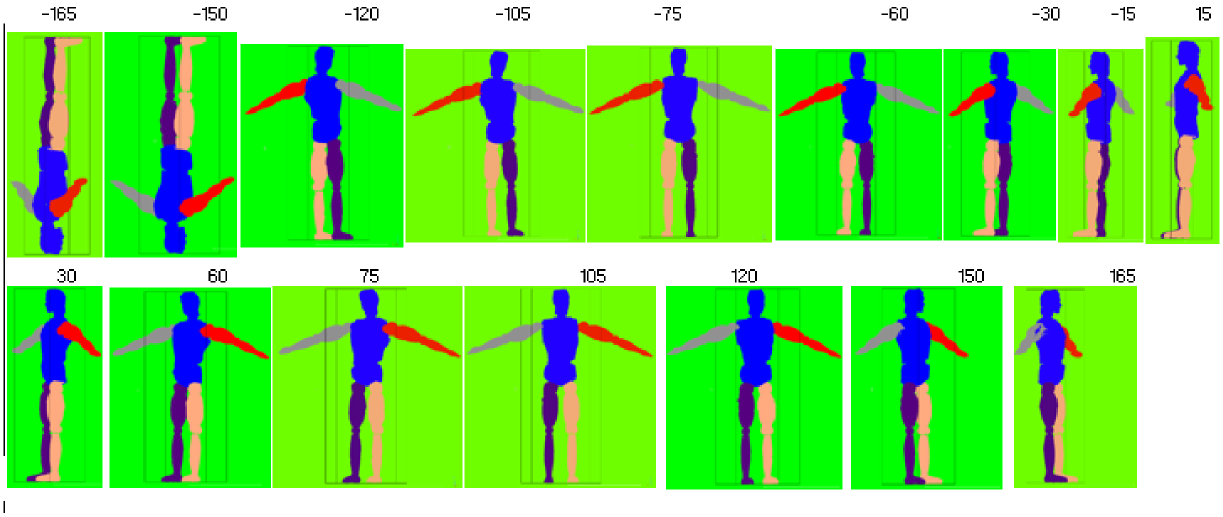

Figure 96 - Position of the model for configuration 2, with rotation along the x-axis

Table 20 - Projected surfaces for configuration 2 with variation along the x-axis for many different position

Configuration 2				m^2					
x	z	y	Numbers of pixels	Total surface	torso	left leg	right leg	left arm	right arm
-180	0	0	37657	0.28024	0.04196	0.03588	0.03595	0.07615	0.09032
-165	0	0	42348	0.31516	0.06511	0.05043	0.05541	0.06146	0.08275
-150	0	0	45926	0.34178	0.09946	0.05148	0.07912	0.04397	0.06775
-135	0	0	47647	0.35459	0.12645	0.05017	0.10420	0.02654	0.04723
-105	0	0	185425	0.36910	0.17742	0.03801	0.12659	0.00506	0.02203
-90	0	0	47803	0.35704	0.16108	0.12942	0.02448	0.04207	0.00000
-75	0	0	176078	0.35182	0.13555	0.02604	0.12835	0.00000	0.06188
-60	0	0	45180	0.33745	0.13482	0.02224	0.09860	0.00240	0.07939
-45	0	0	42148	0.31367	0.12215	0.01508	0.06015	0.02428	0.09201
-30	0	0	39605	0.29581	0.10264	0.00922	0.03412	0.00000	0.09965
-15	0	0	143950	0.28763	0.08768	0.00786	0.02525	0.06849	0.09833
0	0	0	38161	0.28297	0.09001	0.01338	0.01118	0.07653	0.09187
15	0	0	156409	0.31252	0.09631	0.04227	0.01689	0.07923	0.07782
30	0	0	46086	0.34297	0.12485	0.06686	0.02487	0.07650	0.04988
45	0	0	47807	0.35578	0.14617	0.08980	0.03217	0.06949	0.01816
60	0	0	48586	0.36158	0.15638	0.11098	0.03592	0.05830	0.00000
75	0	0	184117	0.36650	0.15968	0.12448	0.03542	0.04394	0.00297
90	0	0	47658	0.35467	0.17398	0.12697	0.02635	0.02737	0.00000
105	0	0	177047	0.35376	0.17829	0.12338	0.03781	0.01428	0.00000
120	0	0	45583	0.33923	0.16111	0.11357	0.04171	0.02285	0.00000
135	0	0	42573	0.31683	0.13602	0.09573	0.04354	0.04153	0.00000
150	0	0	38879	0.28934	0.09970	0.07475	0.04301	0.05826	0.01362
165	0	0	141885	0.28243	0.06176	0.05318	0.04244	0.06947	0.05559
180	0	0	37657	0.28024	0.04196	0.03588	0.03595	0.07615	0.09032

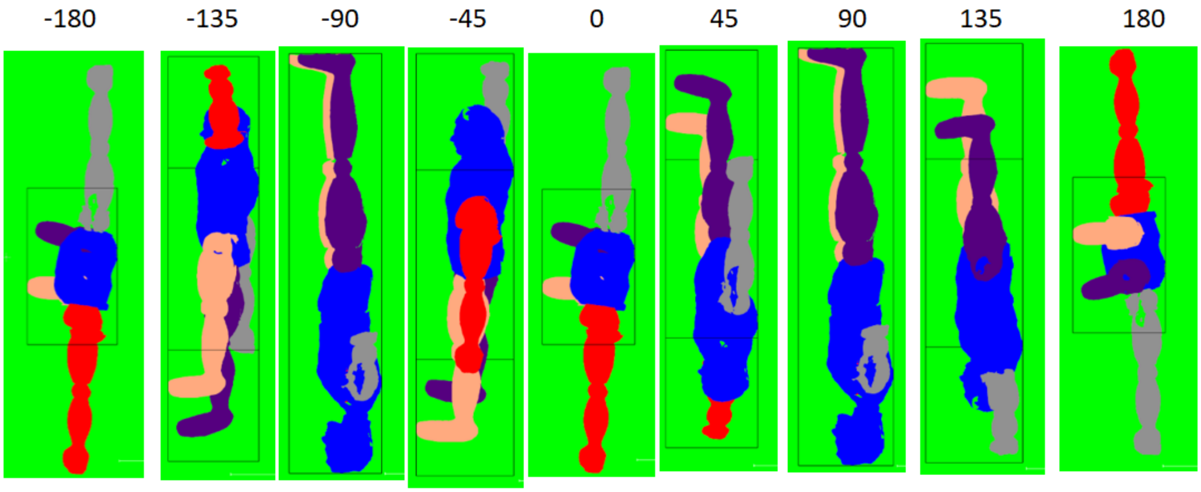

Figure 97 - Position of the model for configuration 2, with rotation along the x-axis

Table 21 - Projected surfaces for configuration 3 with variation along the x-axis for different positions (negative angle)

Configuration 3				m^2					
x	z	y	Numbers of pixels	Total surface	torso	left leg	right leg	left arm	right arm
-90	0	-180	237719	0.49560	0.23548	0.15984	0.00294	0.09734	0.00000
-90	0	-179	238670	0.49758	0.23564	0.15940	0.00397	0.09636	0.00166
-90	0	-178	242957	0.50652	0.23573	0.16002	0.00715	0.09595	0.00766
-90	0	-177	248143	0.51733	0.23564	0.16007	0.01132	0.09584	0.01445
-90	0	-176	253206	0.52789	0.23583	0.15956	0.01591	0.09578	0.02081
-90	0	-175	258950	0.53986	0.23581	0.16080	0.02077	0.09532	0.02717
-90	0	-165	296718	0.61860	0.23382	0.16180	0.06914	0.09311	0.06074
-90	0	-150	315630	0.65803	0.20944	0.16544	0.12682	0.09003	0.06628
-90	0	-135	310136	0.64658	0.16826	0.16584	0.14986	0.09169	0.07093
-90	0	-125	285152	0.59449	0.13973	0.16148	0.15615	0.09415	0.04298
-90	0	-124	278445	0.58051	0.13687	0.16098	0.15571	0.09408	0.03286
-90	0	-123	272008	0.56709	0.13343	0.16010	0.15635	0.09400	0.02320
-90	0	-122	266599	0.55581	0.13059	0.16015	0.15644	0.09400	0.01463
-90	0	-121	261559	0.54530	0.12818	0.15956	0.15560	0.09421	0.00775
-90	0	-120	258580	0.53909	0.12600	0.15940	0.15598	0.09445	0.00000
-90	0	-119	257151	0.53611	0.12390	0.15881	0.15556	0.09453	0.00331
-90	0	-118	257171	0.53615	0.12213	0.15797	0.15535	0.09463	0.00606
-90	0	-117	257973	0.53783	0.11983	0.15708	0.15504	0.09462	0.01125
-90	0	-116	259706	0.54144	0.11713	0.15618	0.15458	0.09479	0.01876
-90	0	-115	261649	0.54549	0.11534	0.15533	0.15319	0.09479	0.02684
-90	0	-110	266207	0.55499	0.10322	0.15196	0.15060	0.09467	0.05454
-90	0	-109	263192	0.54871	0.10079	0.15130	0.15001	0.09471	0.05191
-90	0	-108	258799	0.53955	0.09830	0.15052	0.14939	0.09458	0.04676
-90	0	-107	254126	0.52981	0.09579	0.14984	0.14871	0.09447	0.04099
-90	0	-106	249449	0.52005	0.09331	0.14902	0.14802	0.09430	0.03541
-90	0	-105	245312	0.51143	0.09086	0.14861	0.14729	0.09408	0.03058
-90	0	-104	241599	0.50369	0.08845	0.14783	0.14672	0.09399	0.02670
-90	0	-103	238943	0.49619	0.08686	0.14657	0.14531	0.09349	0.02397
-90	0	-102	236691	0.49152	0.08494	0.14596	0.14475	0.09341	0.02245
-90	0	-101	235726	0.48951	0.08321	0.14533	0.14419	0.09316	0.02363
-90	0	-100	236064	0.49215	0.08101	0.14529	0.14399	0.09401	0.02785
-90	0	-99	238099	0.49639	0.07890	0.14511	0.14324	0.09337	0.03577
-90	0	-98	241738	0.50200	0.07611	0.14404	0.14193	0.09289	0.04703
-90	0	-97	245903	0.51266	0.07449	0.14394	0.14155	0.09296	0.05972
-90	0	-90	264323	0.55106	0.06639	0.14079	0.13846	0.08318	0.12224
-90	0	-84	244369	0.50946	0.07539	0.13802	0.13757	0.03390	0.12458
-90	0	-83	240499	0.50140	0.07783	0.13755	0.13710	0.02451	0.12440
-90	0	-82	238042	0.49627	0.07999	0.13796	0.13760	0.01622	0.12451
-90	0	-81	235995	0.49201	0.08250	0.13744	0.13745	0.00993	0.12468
-90	0	-80	234528	0.48895	0.08402	0.13671	0.13786	0.00598	0.12438

-90	0	-79	235042	0.49002	0.08653	0.13639	0.13759	0.00501	0.12449
-90	0	-78	237447	0.49503	0.08843	0.13619	0.13781	0.00823	0.12437
-90	0	-77	241827	0.50416	0.09116	0.13535	0.13837	0.01489	0.12439
-90	0	-76	246665	0.51425	0.09340	0.13503	0.13850	0.02305	0.12426
-90	0	-75	251737	0.52482	0.09514	0.13534	0.13833	0.03174	0.12428
-90	0	-67	265332	0.55317	0.11212	0.13521	0.14136	0.04106	0.12341
-90	0	-66	262287	0.54682	0.11425	0.13583	0.14256	0.03102	0.12316
-90	0	-65	259728	0.54148	0.11626	0.13633	0.14245	0.02338	0.12307
-90	0	-64	257826	0.53752	0.11812	0.13634	0.14279	0.01734	0.12294
-90	0	-63	255890	0.53348	0.11982	0.13430	0.14337	0.01134	0.12267
-90	0	-62	254870	0.53136	0.12162	0.13670	0.14399	0.00659	0.12246
-90	0	-61	255003	0.53163	0.12300	0.13474	0.14452	0.00481	0.12229
-90	0	-60	257256	0.53633	0.12441	0.13732	0.14516	0.00741	0.12203
-90	0	-59	261540	0.54526	0.12585	0.13805	0.14556	0.01403	0.12178
-90	0	-58	266535	0.55568	0.12734	0.13786	0.14607	0.02310	0.12131
-90	0	-57	272417	0.56794	0.12893	0.13816	0.14647	0.03328	0.12110
-90	0	-45	309237	0.64470	0.16078	0.13605	0.15203	0.07815	0.11770
-90	0	-30	315031	0.65678	0.19868	0.11508	0.15789	0.07394	0.11119
-90	0	-15	294145	0.61324	0.22369	0.05700	0.16175	0.06776	0.10304
-90	0	-7	265784	0.55411	0.22918	0.01991	0.16279	0.04218	0.10004
-90	0	-6	260551	0.54320	0.22972	0.01549	0.16254	0.03590	0.09955
-90	0	-5	255493	0.53266	0.22984	0.01126	0.16263	0.02954	0.09938
-90	0	-4	250260	0.52175	0.22995	0.00729	0.16262	0.02307	0.09882
-90	0	-3	245172	0.51114	0.22977	0.00365	0.16284	0.01652	0.09836
-90	0	-2	240871	0.50217	0.22982	0.00083	0.16311	0.01021	0.09820
-90	0	-1	237411	0.49496	0.22988	0.00000	0.16268	0.00454	0.09786

Table 22 - Projected surfaces for configuration 3 with variation along the y-axis for different positions (positive angle)

Configuration 3				m^2					
x	z	y	Numbers of pixels	Total surface	torso	left leg	right leg	left arm	right arm
-90	0	180	237654	0.49546	0.23552	0.15977	0.00295	0.09722	0.00000
-90	0	179	237449	0.49504	0.23490	0.15917	0.00285	0.09725	0.00086
-90	0	178	239597	0.49951	0.23457	0.15829	0.00339	0.09732	0.00595
-90	0	177	244046	0.50879	0.23416	0.15892	0.00601	0.09689	0.01280
-90	0	175	207609	0.43283	0.23304	0.15863	0.01295	0.00000	0.02821
-90	0	165	293105	0.61107	0.22575	0.15410	0.05544	0.09884	0.07694
-90	0	150	312486	0.65147	0.21297	0.14703	0.10575	0.10381	0.08193
-90	0	135	307812	0.64173	0.19590	0.13746	0.12042	0.10702	0.08093
-90	0	123	270136	0.56097	0.16699	0.12974	0.07481	0.10404	0.08539
-90	0	122	264140	0.55068	0.16470	0.12925	0.06494	0.10422	0.08757
-90	0	121	259028	0.54002	0.16193	0.12829	0.05558	0.10428	0.08994
-90	0	120	254771	0.53115	0.15890	0.12830	0.04846	0.10333	0.09216

-90	0	119	251951	0.52527	0.15634	0.12706	0.04422	0.10327	0.09439
-90	0	118	250898	0.52308	0.15361	0.12684	0.04379	0.10228	0.09656
-90	0	117	251772	0.52490	0.15070	0.12572	0.04763	0.10224	0.09860
-90	0	116	253677	0.52887	0.14803	0.12561	0.05323	0.10128	0.10073
-90	0	115	255714	0.53312	0.14533	0.12359	0.06033	0.10122	0.10265
-90	0	105	246379	0.51365	0.11655	0.06862	0.11326	0.09762	0.11761
-90	0	104	241347	0.50316	0.11472	0.05957	0.11417	0.09705	0.11765
-90	0	103	231974	0.48941	0.11440	0.04203	0.11542	0.09761	0.11996
-90	0	102	231974	0.48941	0.11395	0.04203	0.11542	0.09761	0.11996
-90	0	101	229728	0.47894	0.11264	0.03761	0.11356	0.09601	0.11911
-90	0	100	229107	0.47577	0.11324	0.03629	0.11182	0.09546	0.11897
-90	0	99	230260	0.48005	0.11503	0.03777	0.11091	0.09558	0.11968
-90	0	98	233541	0.48689	0.11530	0.04397	0.11149	0.09575	0.12038
-90	0	97	236914	0.49984	0.11634	0.05251	0.11209	0.09673	0.12217
-90	0	90	262311	0.54687	0.11137	0.10622	0.11144	0.09439	0.12345
-90	0	83	244813	0.51039	0.11129	0.11539	0.06482	0.09276	0.12613
-90	0	81	237386	0.49491	0.11029	0.11646	0.04847	0.09331	0.12638
-90	0	80	235413	0.49079	0.11010	0.11737	0.04337	0.09349	0.12646
-90	0	79	234457	0.48880	0.11017	0.11760	0.04106	0.09337	0.12660
-90	0	78	235579	0.49114	0.10995	0.11796	0.04275	0.09386	0.12661
-90	0	77	237623	0.49540	0.10965	0.11790	0.04739	0.09372	0.12673
-90	0	76	241162	0.50278	0.10985	0.11845	0.05430	0.09350	0.12668
-90	0	75	244872	0.51051	0.10907	0.11933	0.06225	0.09335	0.12651
-90	0	74	249781	0.52075	0.10902	0.12009	0.07143	0.09370	0.12651
-90	0	65	260513	0.54312	0.11148	0.07747	0.13953	0.09049	0.12415
-90	0	64	257904	0.53557	0.11357	0.06782	0.14200	0.08899	0.12320
-90	0	63	254953	0.53153	0.11717	0.05909	0.14295	0.08757	0.12356
-90	0	62	252900	0.52725	0.12027	0.05290	0.14515	0.08591	0.12301
-90	0	61	252625	0.52668	0.12456	0.04983	0.14554	0.08433	0.12242
-90	0	60	254785	0.53118	0.12844	0.05119	0.14653	0.08288	0.12214
-90	0	59	259032	0.54003	0.13250	0.05691	0.14752	0.08161	0.12149
-90	0	58	264521	0.55148	0.13579	0.06608	0.14802	0.08079	0.12080
-90	0	57	270943	0.56487	0.13914	0.07609	0.14901	0.08022	0.12041
-90	0	45	308269	0.64268	0.17531	0.12393	0.15640	0.07264	0.11440
-90	0	30	313878	0.65438	0.20565	0.10853	0.16223	0.07201	0.10595
-90	0	15	296112	0.61734	0.22313	0.05948	0.16326	0.07377	0.09769
-90	0	5	259121	0.54022	0.22969	0.01570	0.16357	0.03578	0.09547
-90	0	4	253786	0.52910	0.22958	0.01180	0.16298	0.02890	0.09583
-90	0	3	248687	0.51847	0.22949	0.00786	0.16274	0.02203	0.09635
-90	0	2	243890	0.49767	0.22502	0.00420	0.15961	0.01418	0.09465
-90	0	1	238890	0.49804	0.22995	0.00097	0.16296	0.00723	0.09693
-90	0	0	236428	0.49291	0.22993	0.00043	0.16342	0.00177	0.09735

-180

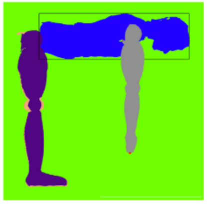

-179

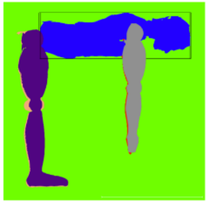

-178

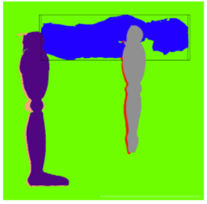

-177

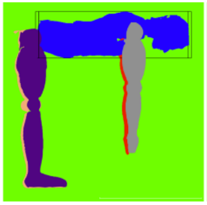

-176

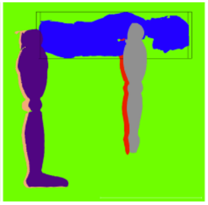

-175

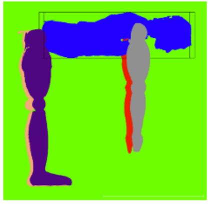

-165

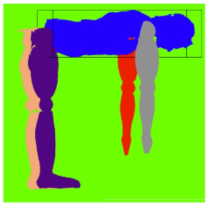

-150

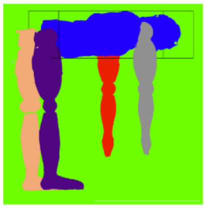

-135

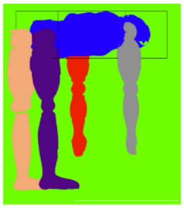

-125

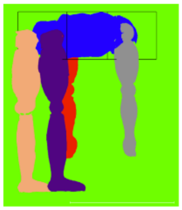

-124

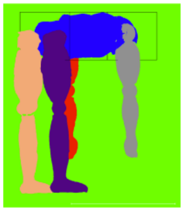

-123

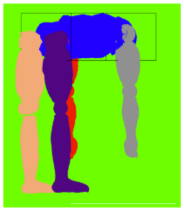

-122

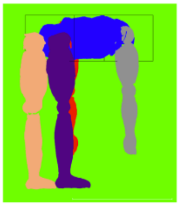

-121

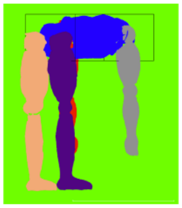

-120

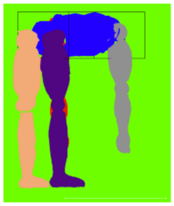

-119

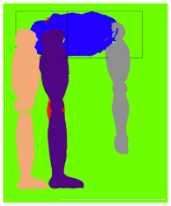

-118

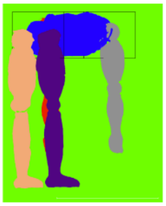

-117

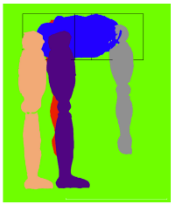

-116

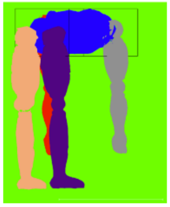

-115

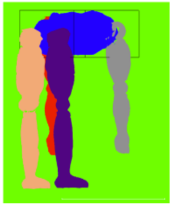

-110

-109

-108

-107

-106

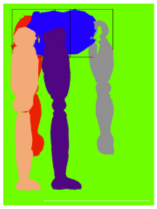

-105

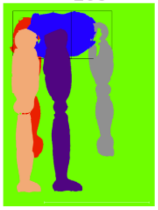

-104

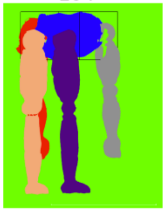

-103

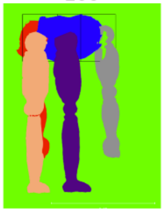

-102

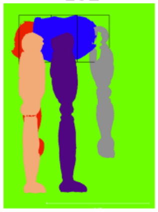

-101

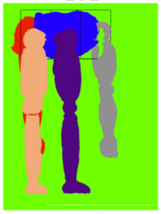

-100

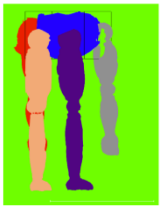

-99

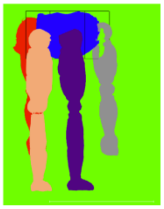

-98

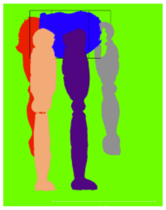

-97

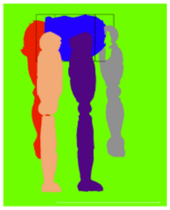

-90

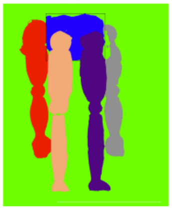

-83

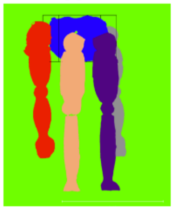

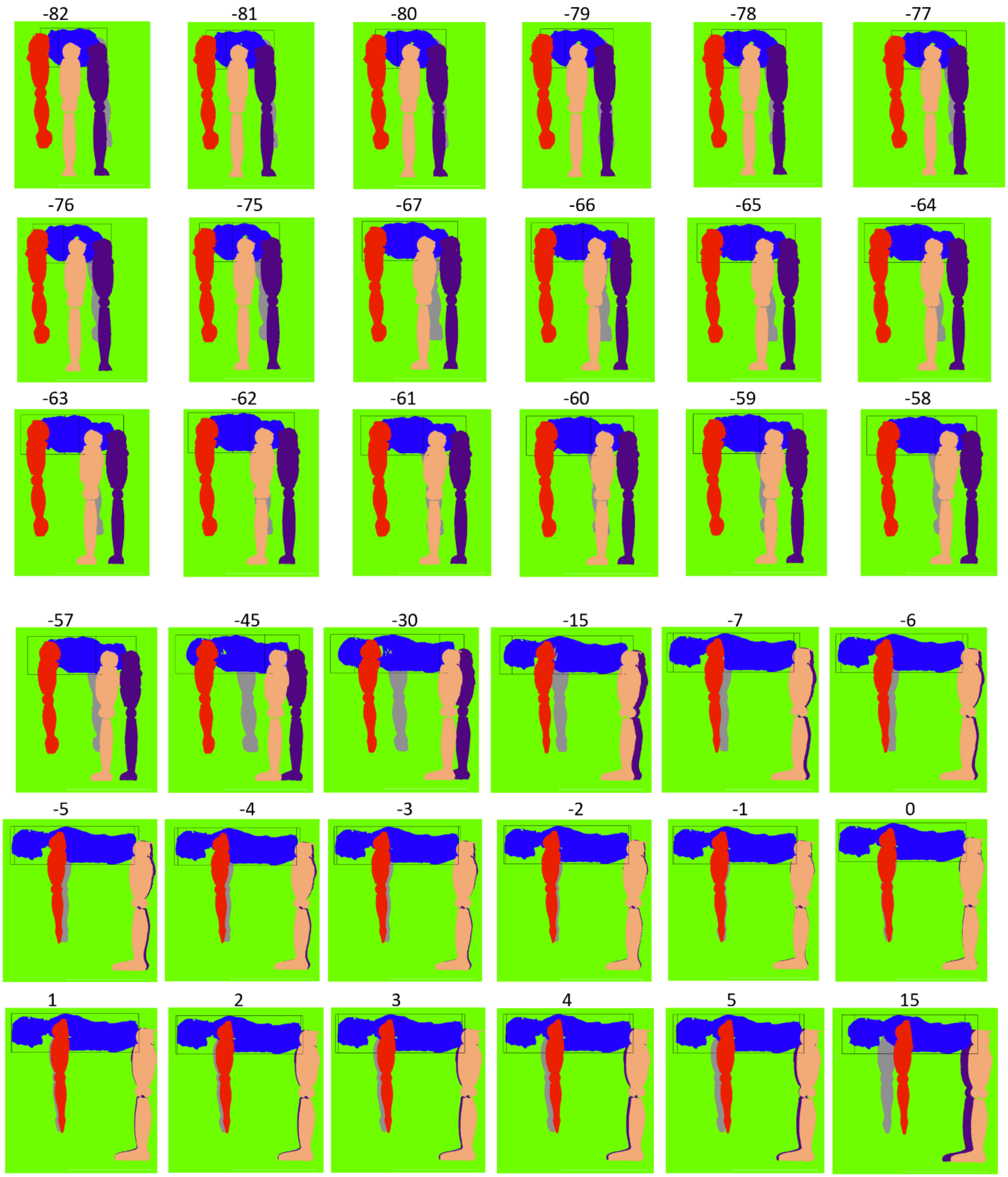
-82
-81
-80
-79
-78
-77
-76
-75
-67
-66
-65
-64
-63
-62
-61
-60
-59
-58
-57
-45
-30
-15
-7
-6
-5
-4
-3
-2
-1
0
1
2
3
4
5
15

30

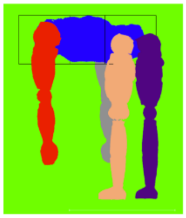

45

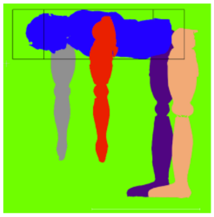

57

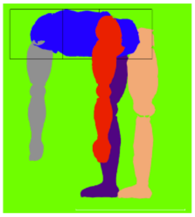

58

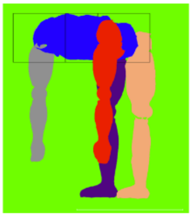

59

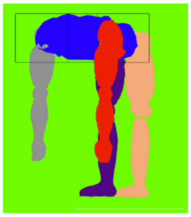

60

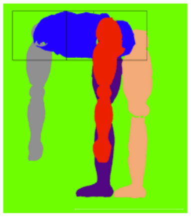

61

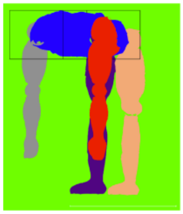

62

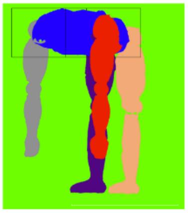

63

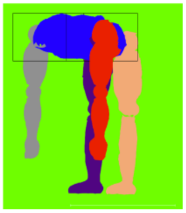

64

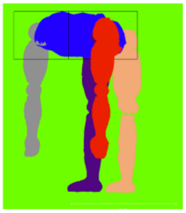

65

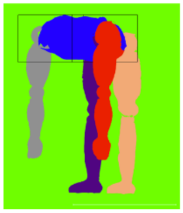

74

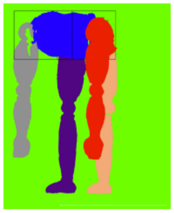

75

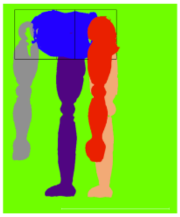

76

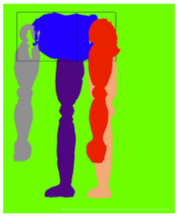

77

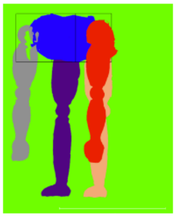

78

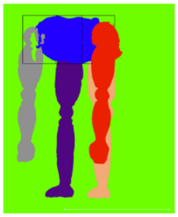

79

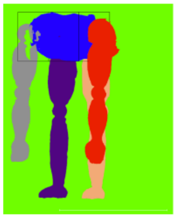

80

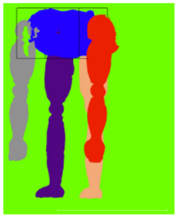

81

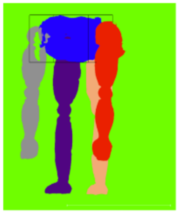

83

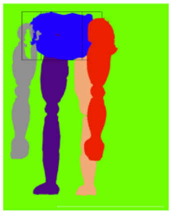

84

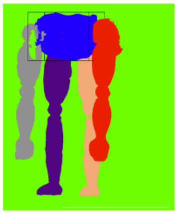

90

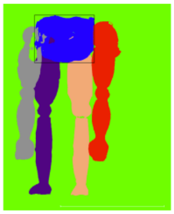

97

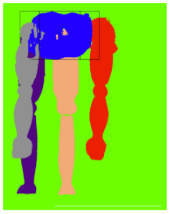

98

99

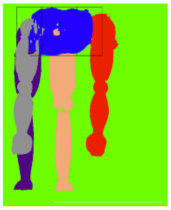

100

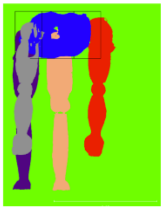

101

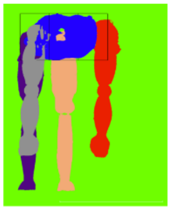

102

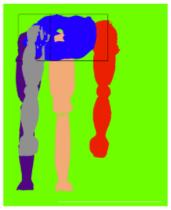

103

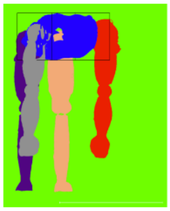

104

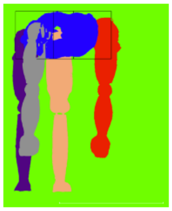

105

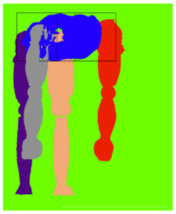

115

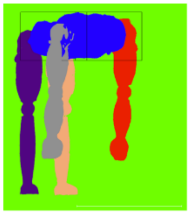

116

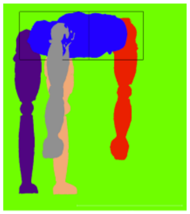

117

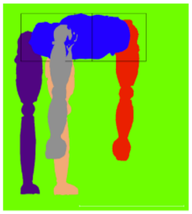

118

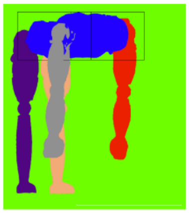

119

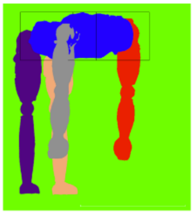

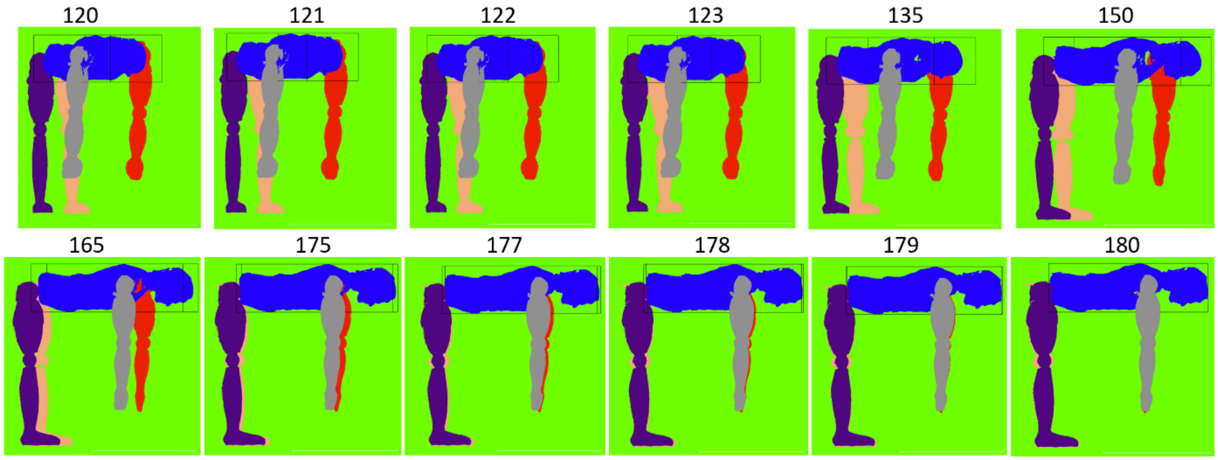

Figure 98 - Position of the model for configuration 3, along the x-axis

Experimental appendix for first slots of results

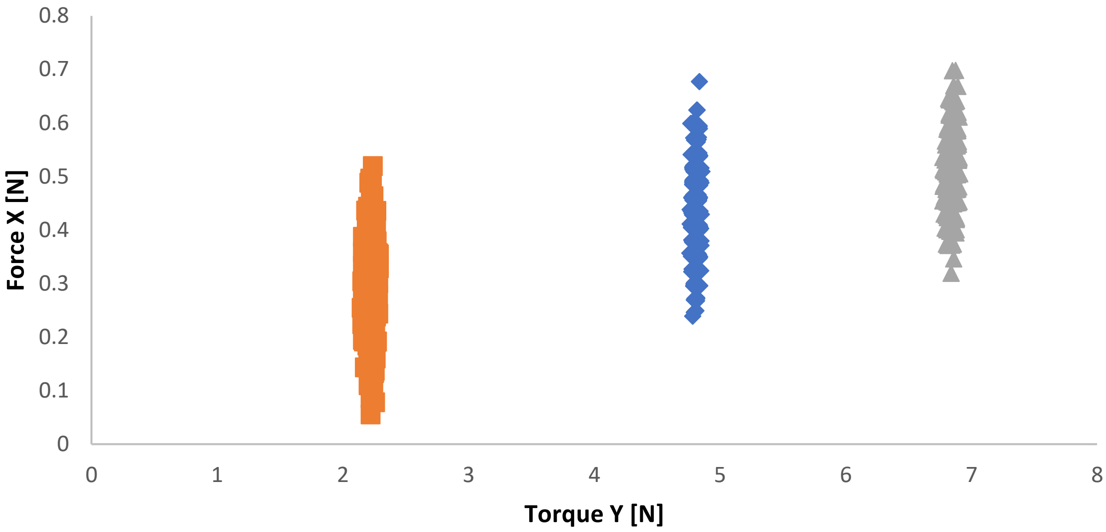

Figure 99 – Calibration of the aerodynamics balance along x-axis

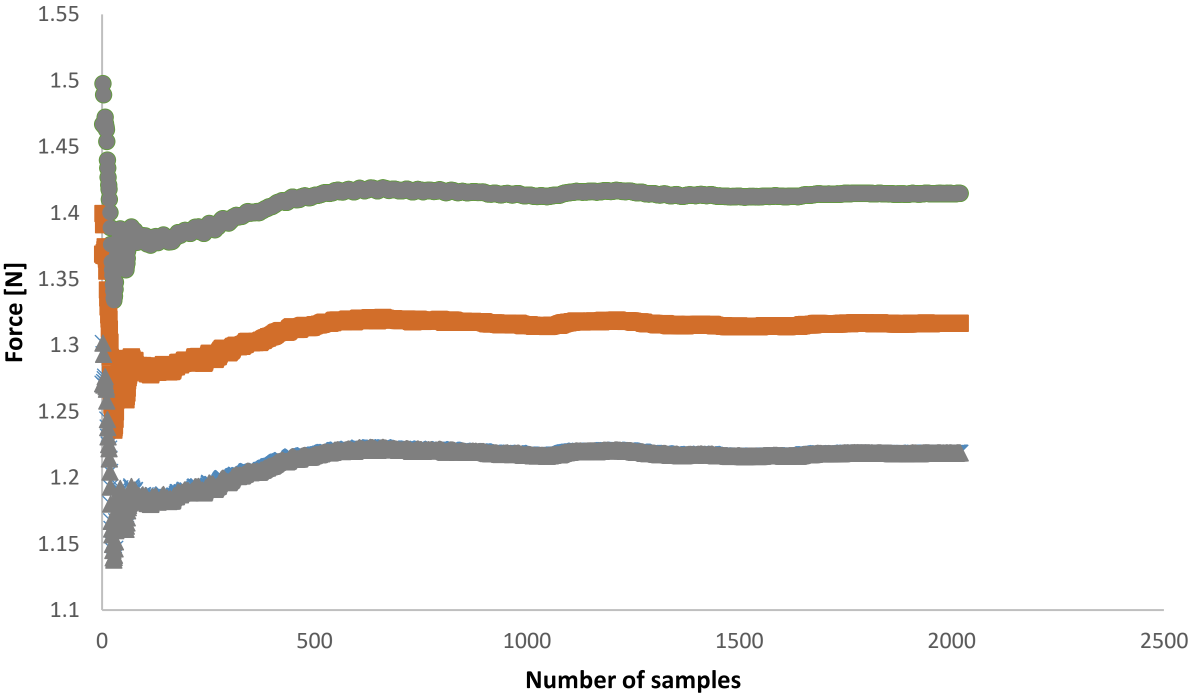

Figure 100 - Moving average of force (orange) for the naked model at 0 degrees with wind at 3.4 m/s and its standard deviation (grey)

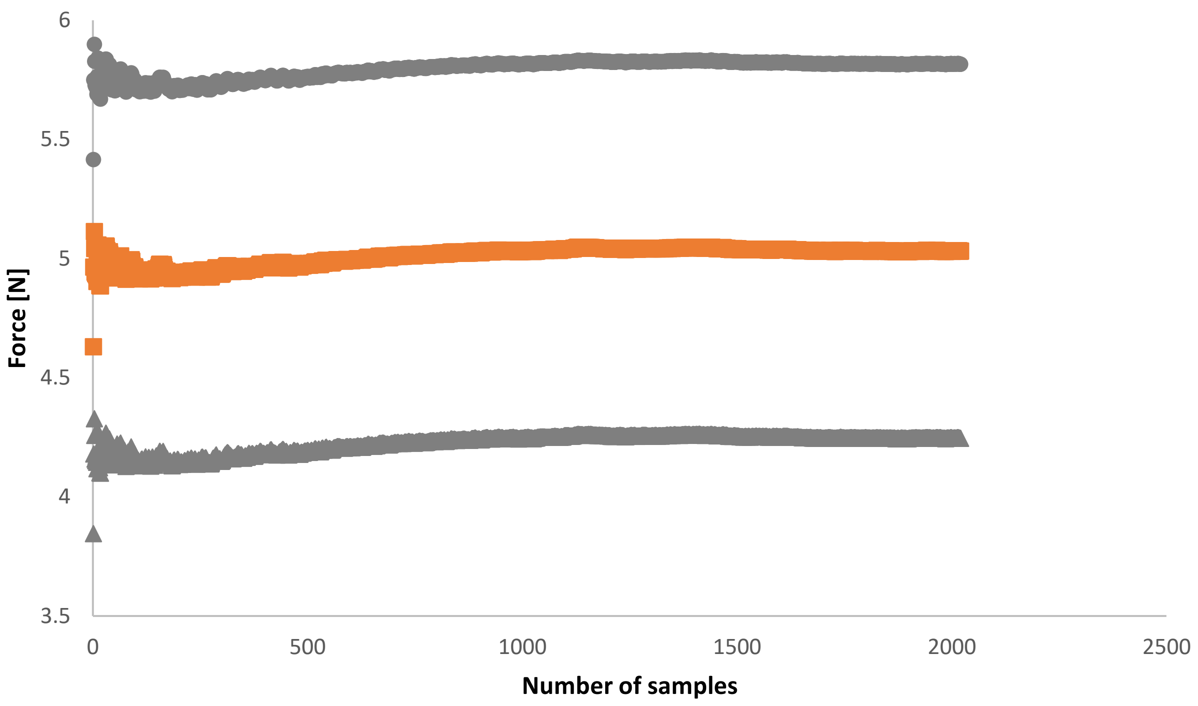

Figure 101 – Moving average of force (orange) for the naked model at 0 degrees with wind at 7.6 m/s and its standard deviation (grey)

Experimental appendix for second slots of results

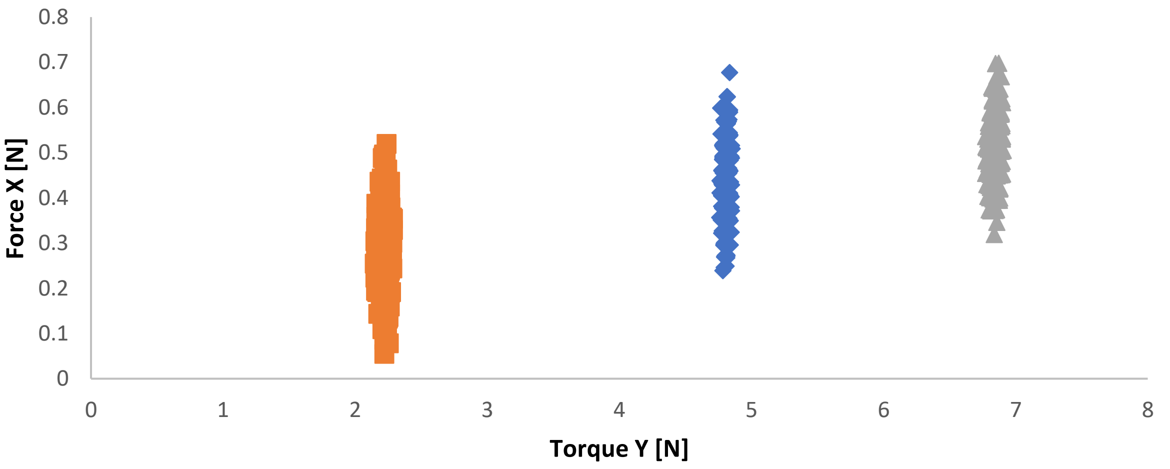

Figure 102 - Calibration of the aerodynamics balance along x-axis

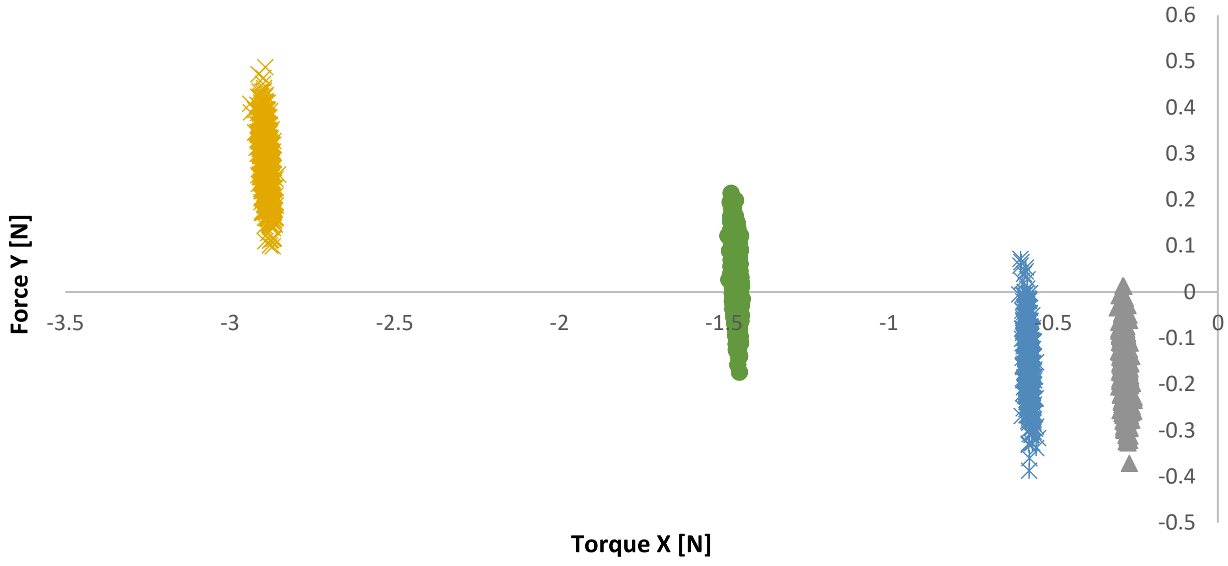

Figure 103 - Calibration of the aerodynamics balance along y-axis

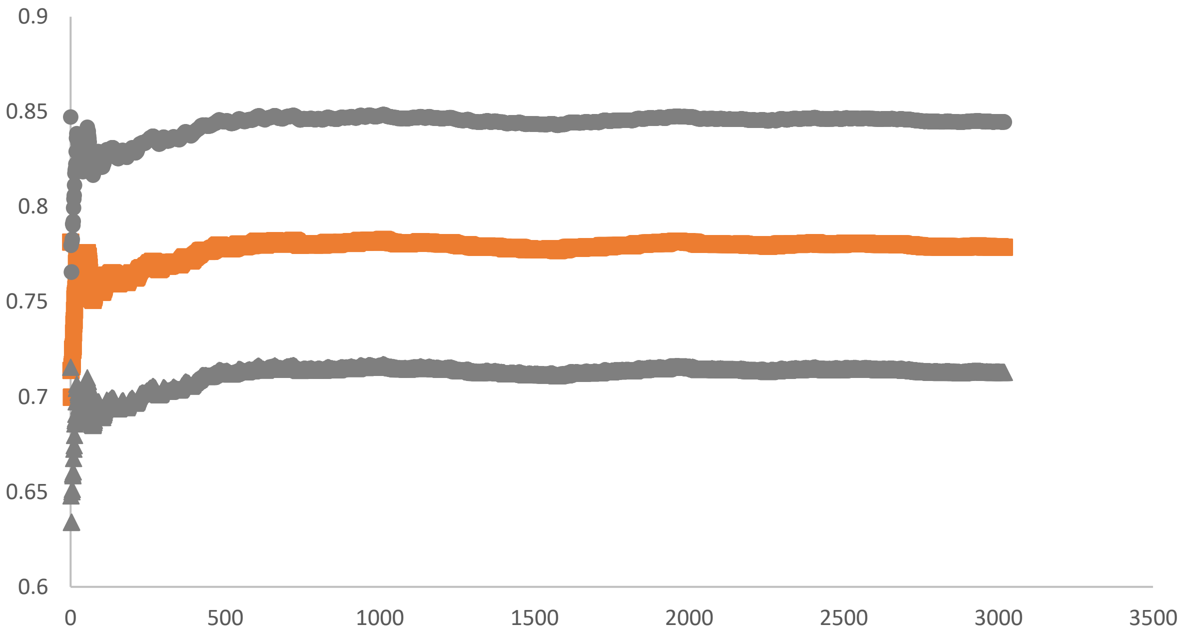

Figure 104 - Moving average of force (orange) for the model at 0 degrees with wind at 3.1 m/s and its standard deviation (grey)

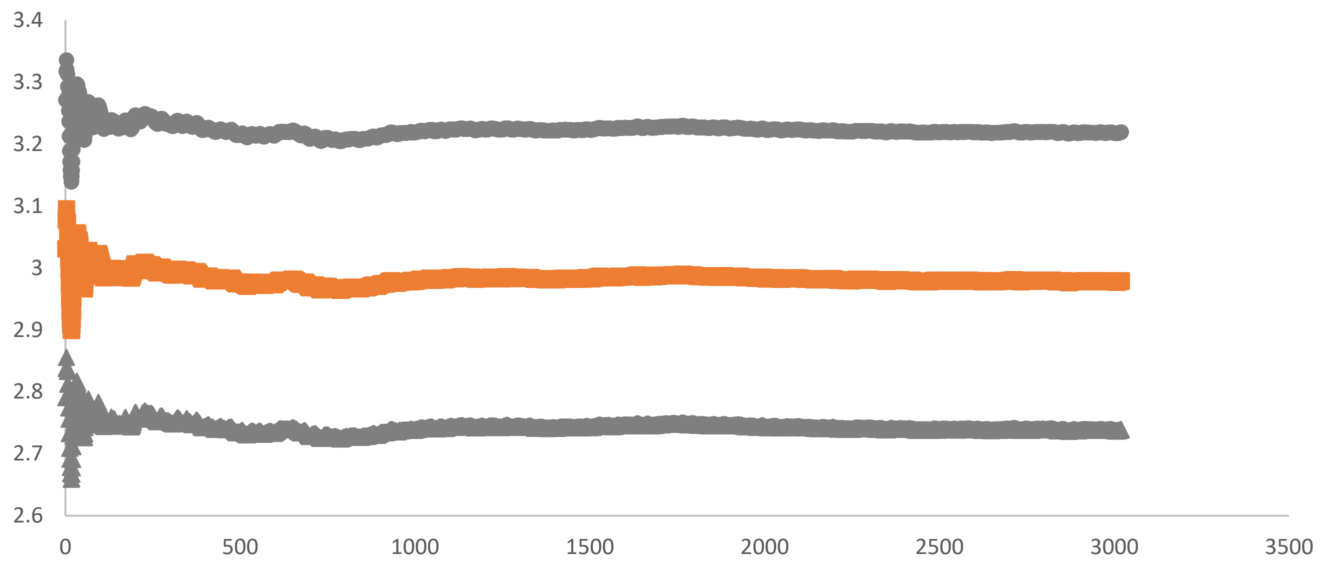

Figure 105 - Moving average of force (orange) for the model at 0 degrees (orange) with wind at 6.6 m/s and its standard deviation (grey)

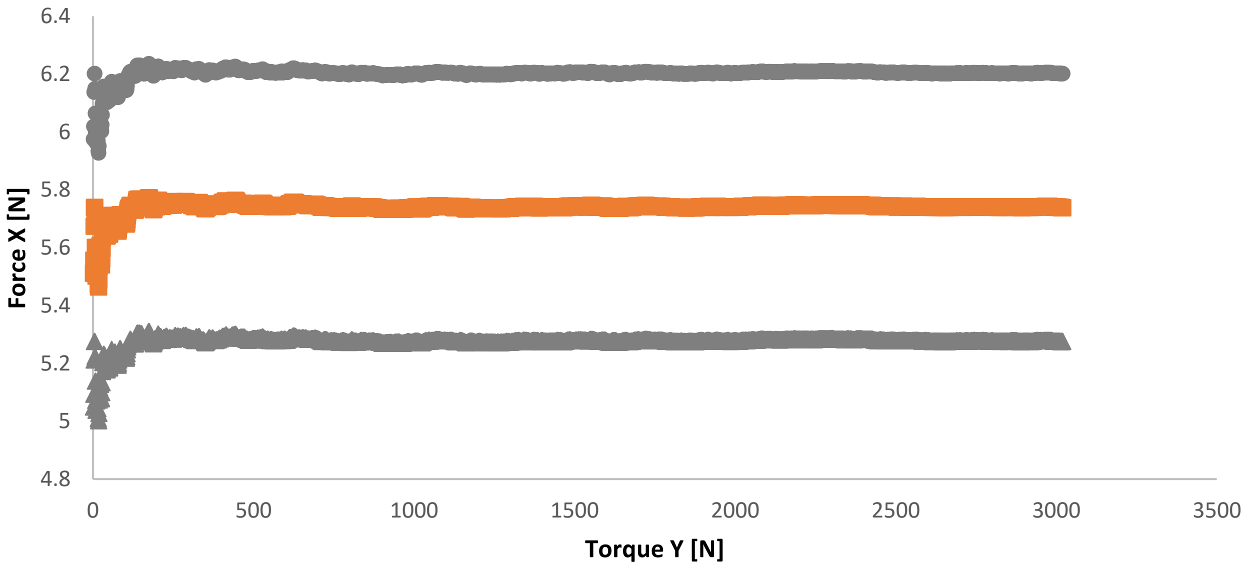

Figure 106 - Moving average of force (orange) for the model at 0 degrees with wind at 9.3 m/s and its standard deviation (grey)

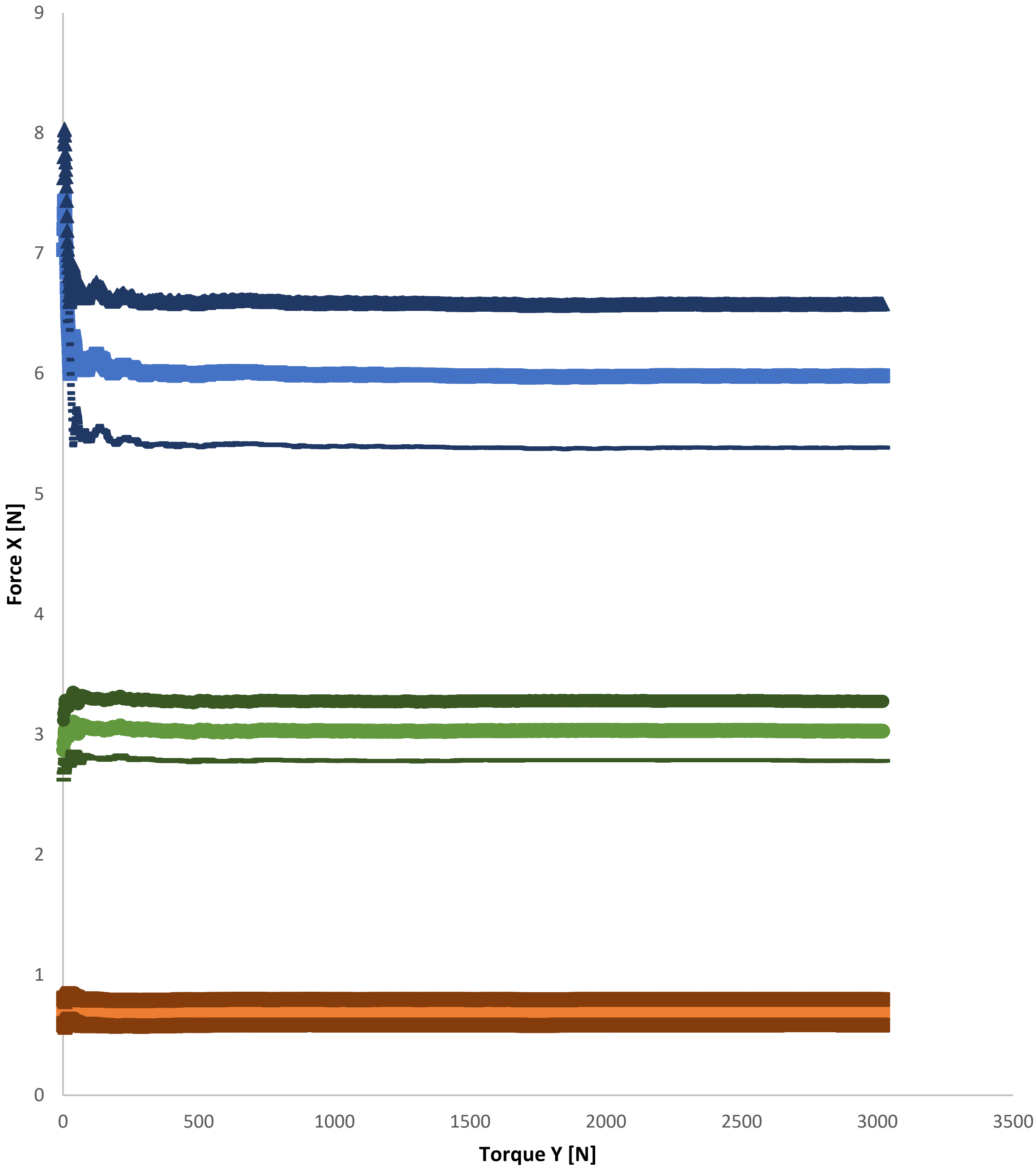

Figure 107 - Moving average of force (light colors) for the model at -20 degrees with wind at 3.1 m/s (in orange), at 6.6 m/s (in green) and at 9.3 m/s (in blue) and its standard deviation (dark colors)

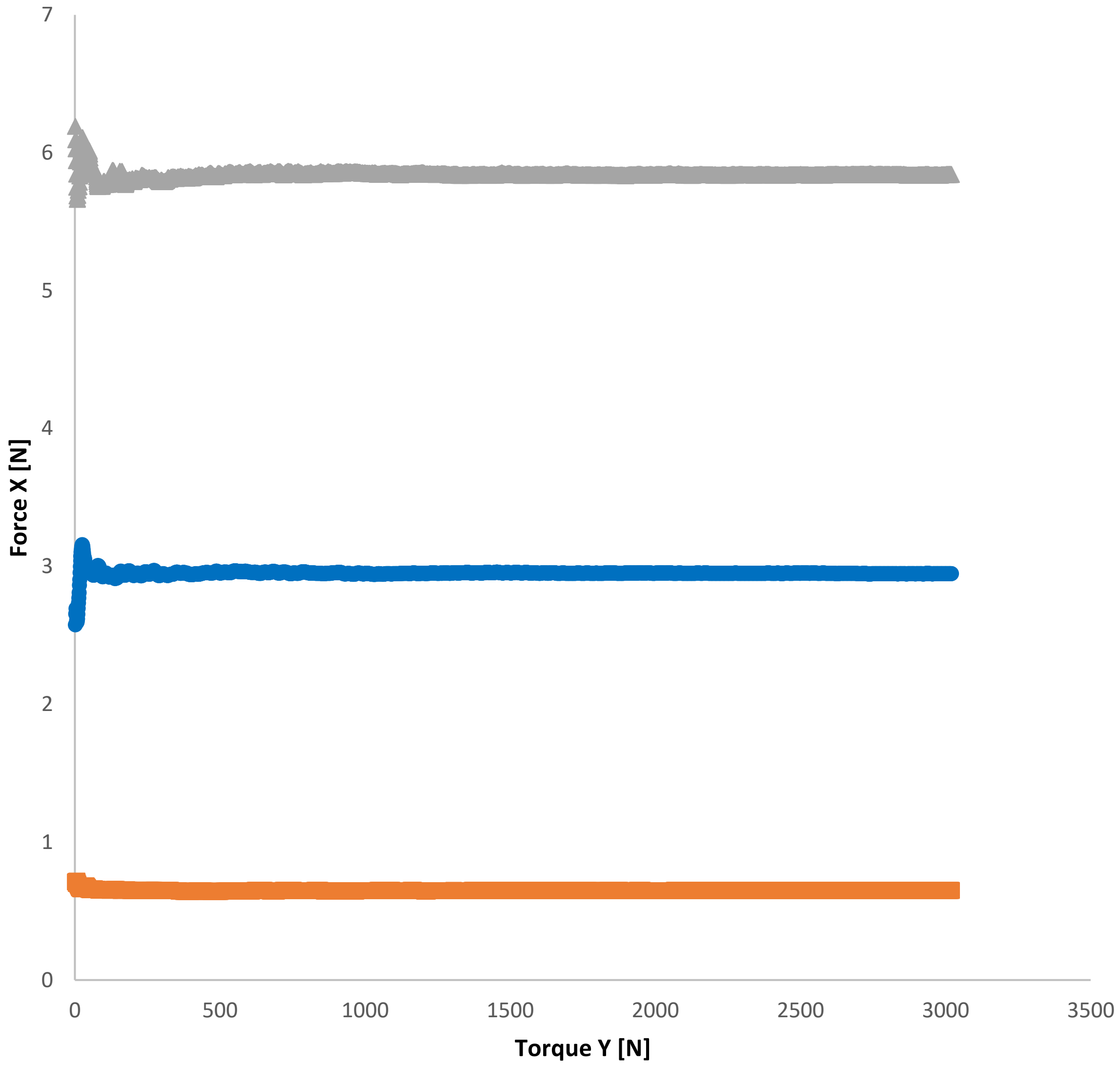

Figure 108 - Moving average of force for the model at 30 degrees with wind at 3.1 m/s, at 6.6 m/s and at 9.3 m/s

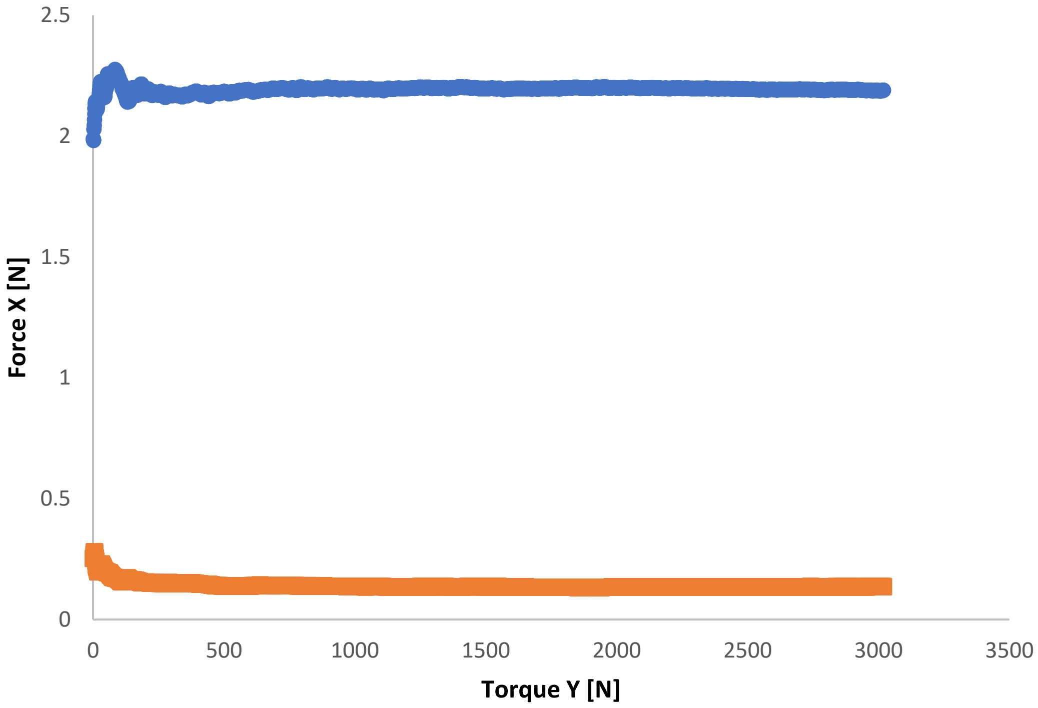

Figure 109 - Moving average of force for the model at 40 degrees with wind at 3.1 m/s and at 6.6 m/s

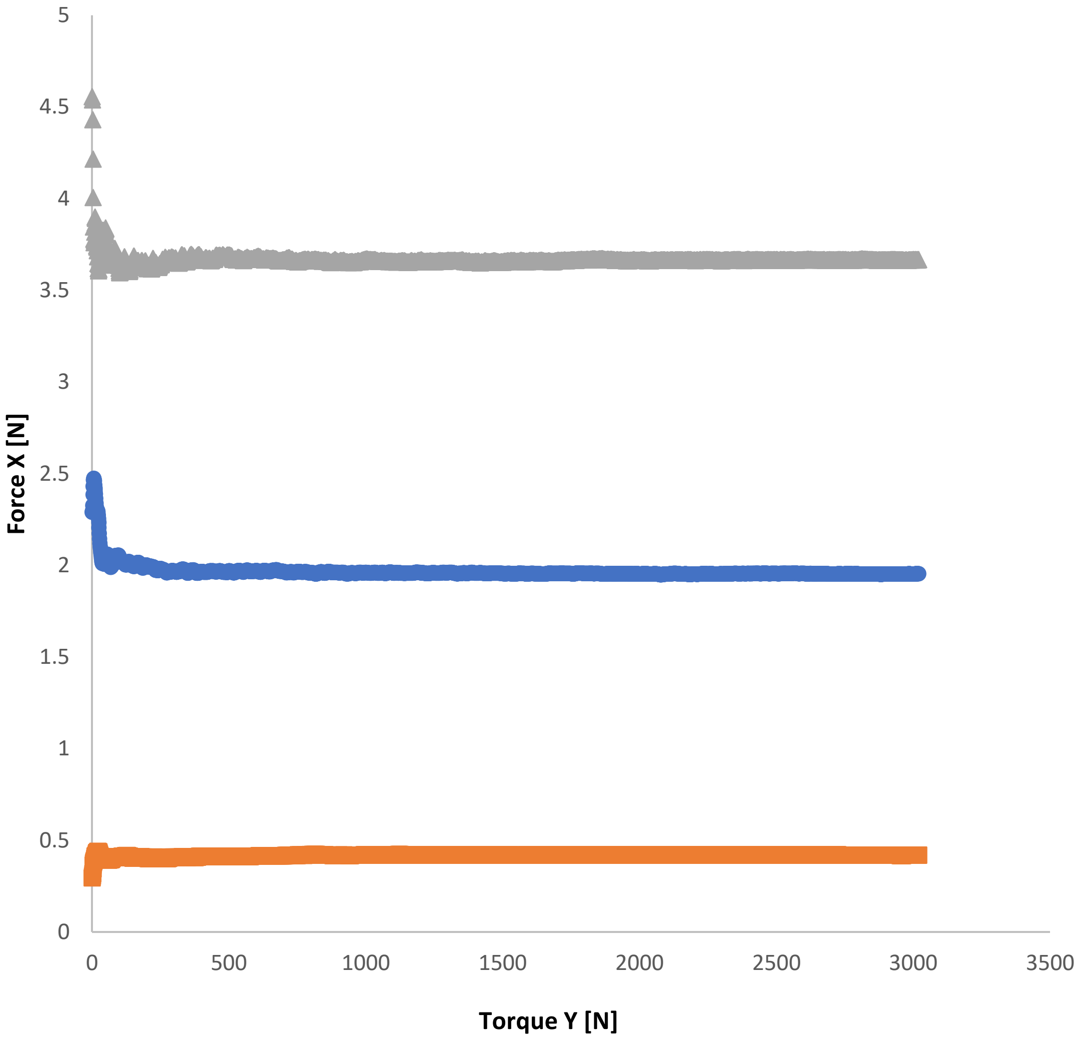

Figure 110 - Moving average of force for the model at 130 degrees with wind at 3.1 m/s, at 6.6 m/s and at 9.3 m/s

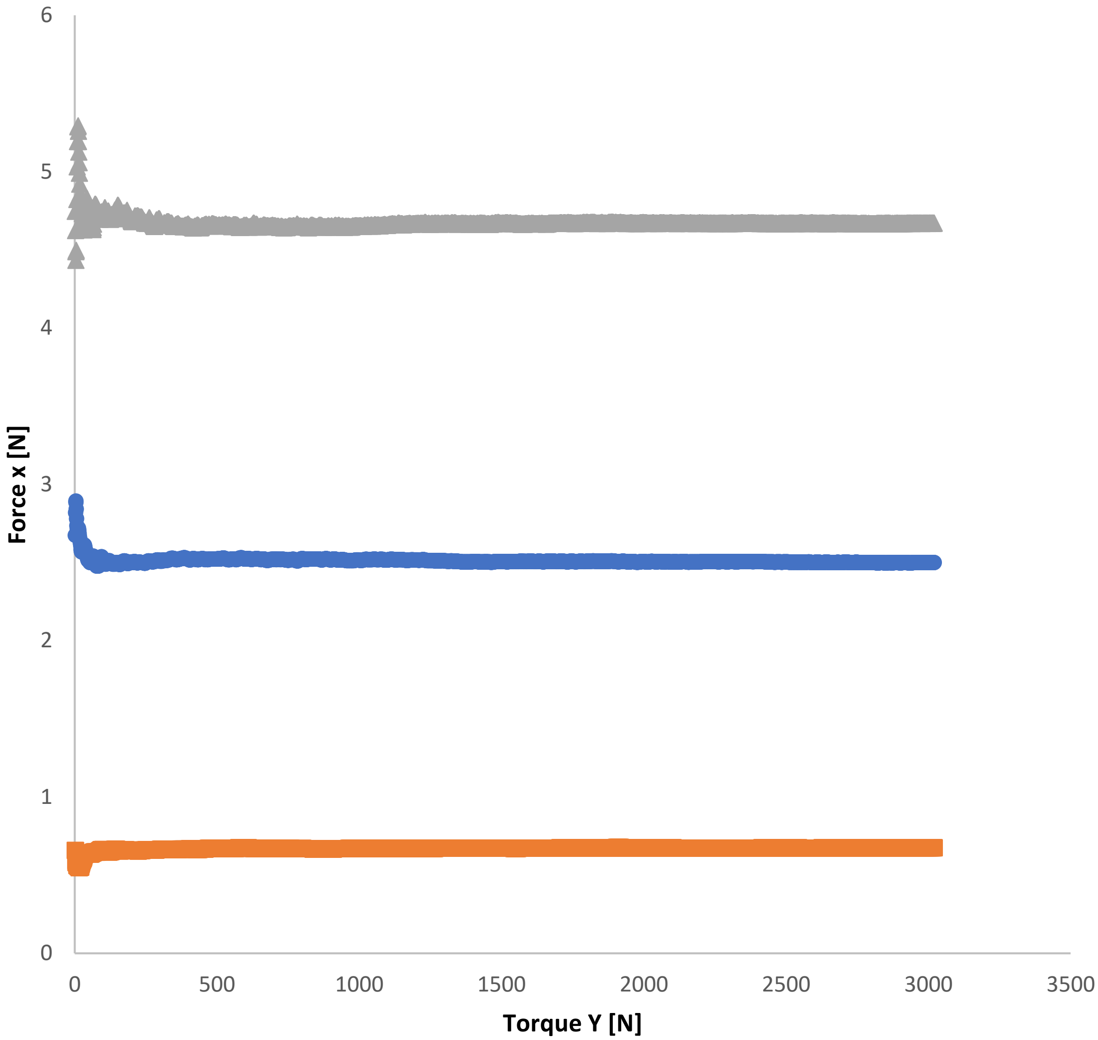

Figure 111 - Moving average of force for the model at 140 degrees with wind at 3.1 m/s, at 6.6 m/s and at 9.3 m/s

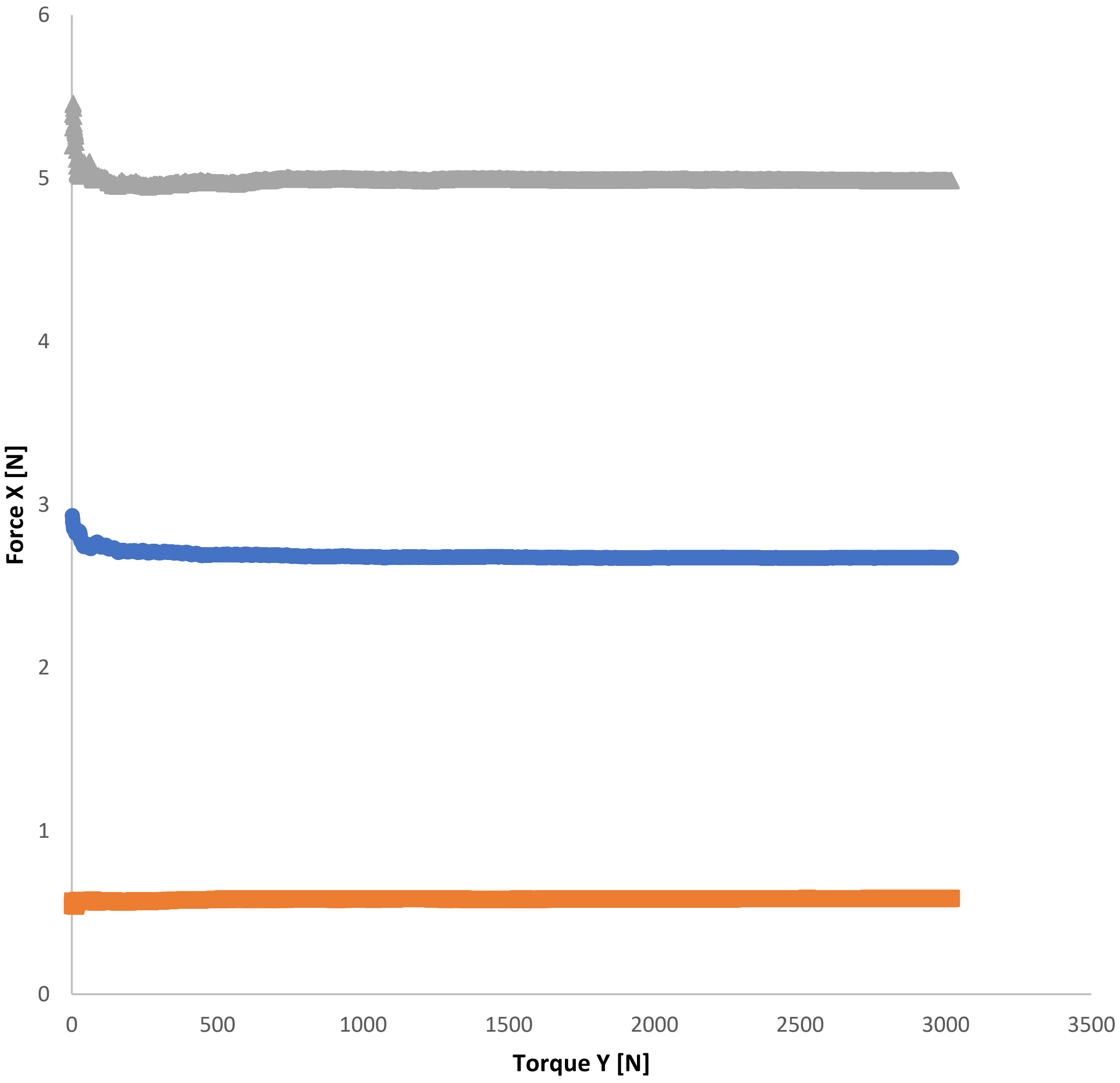

Figure 112 - Moving average of force for the model at 160 degrees with wind at 3.1 m/s, at 6.6 m/s and at 9.4 m/s

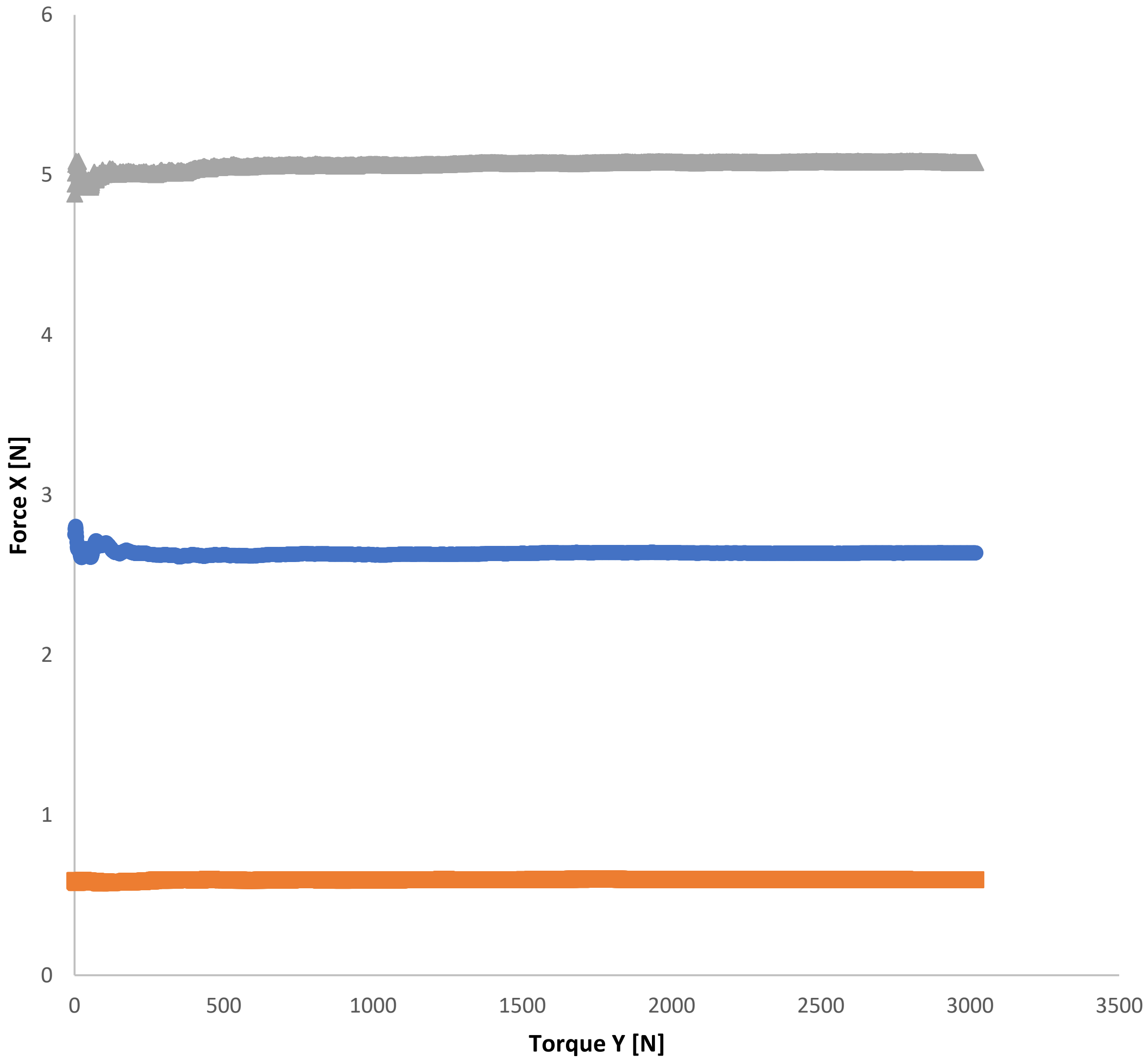

Figure 113 - Moving average of force for the model at 170 degrees with wind at 3.1 m/s, at 6.6 m/s and at 9.4 m/s

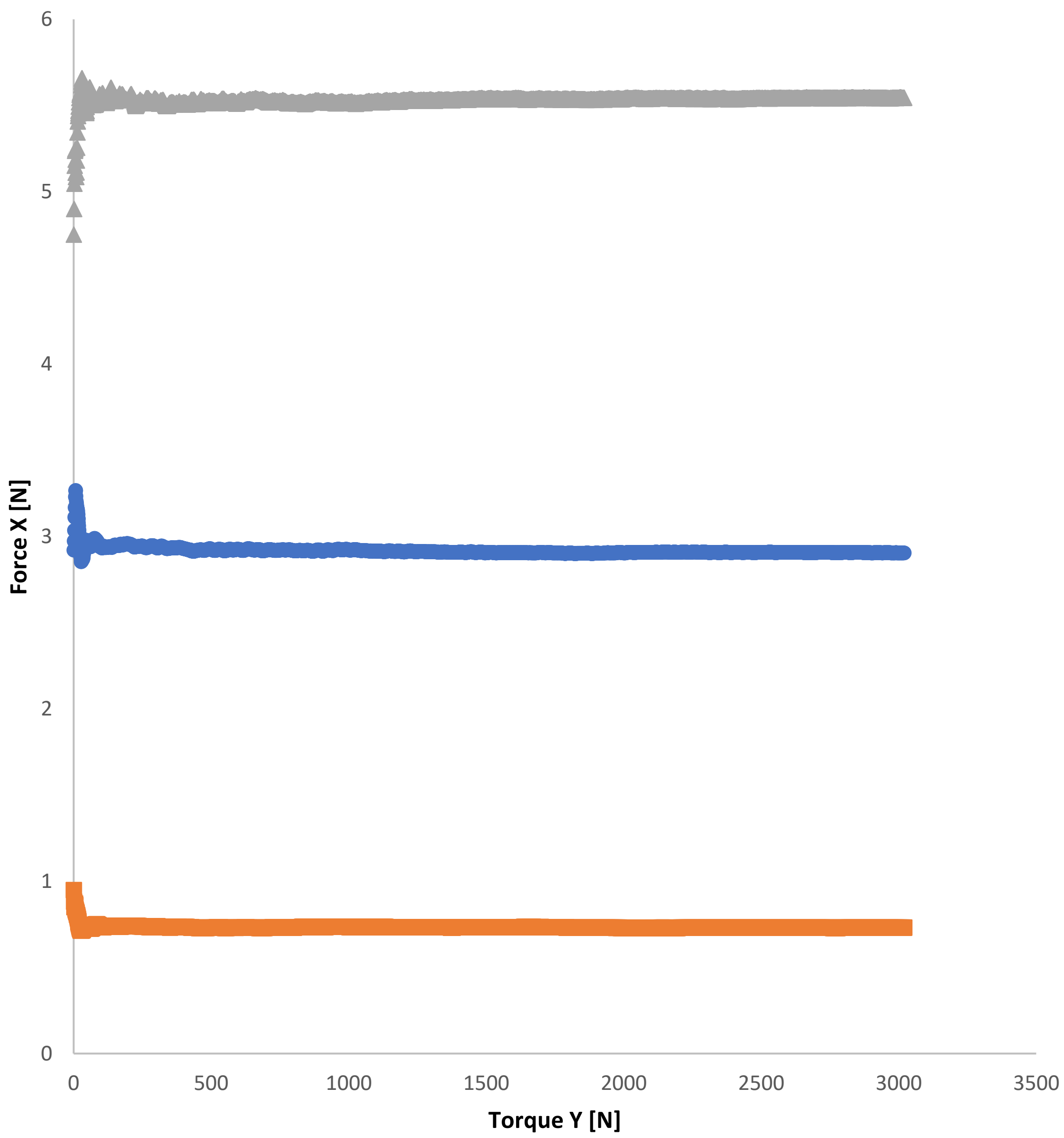

Figure 114 - Moving average of force for the model at 180 degrees with wind at 3.1 m/s, at 6.6 m/s and at 9.4 m/s

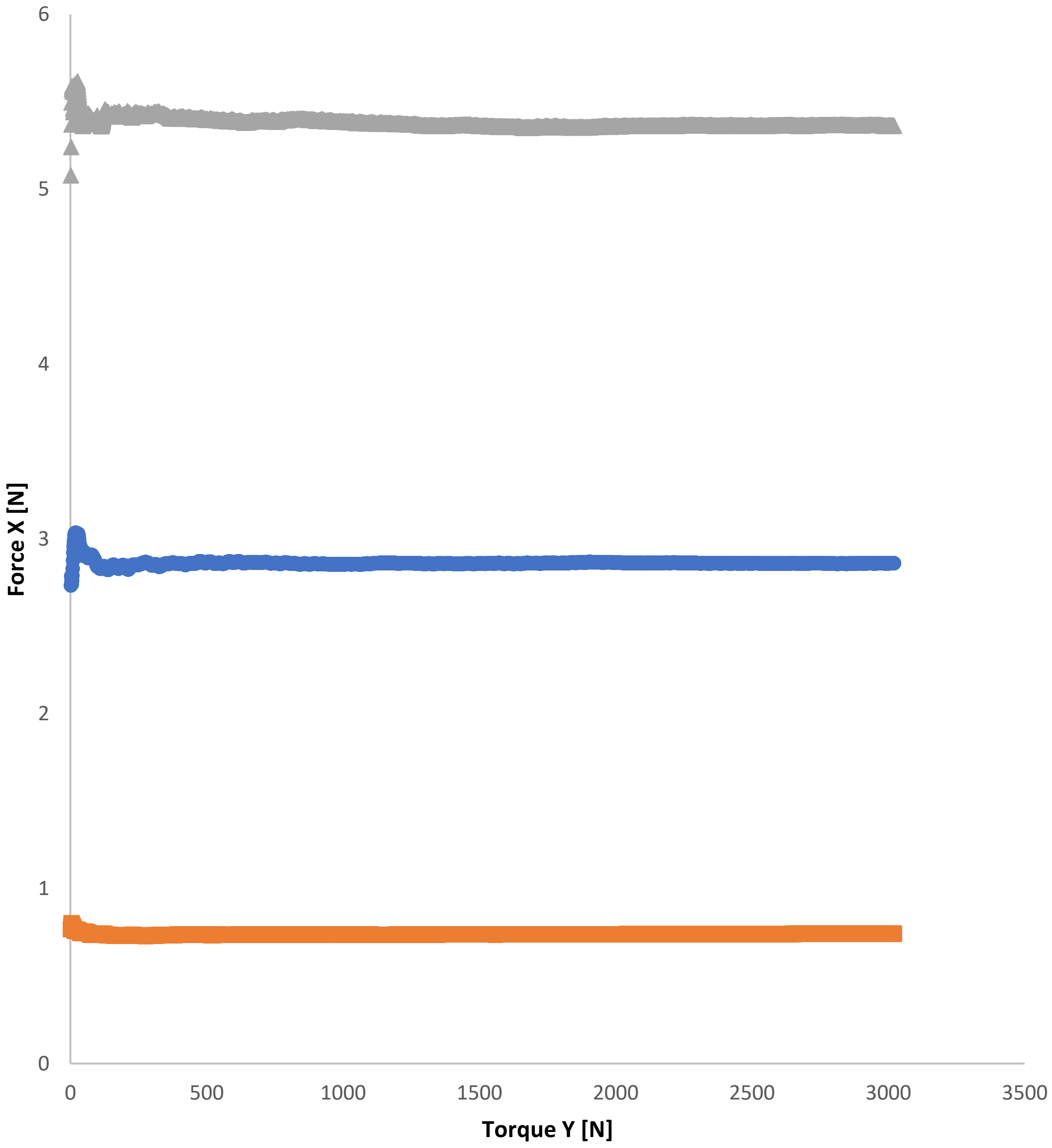

Figure 115 - Moving average of force for the model at 190 degrees with wind at 3.1 m/s, at 6.6 m/s and at 9.4 m/s

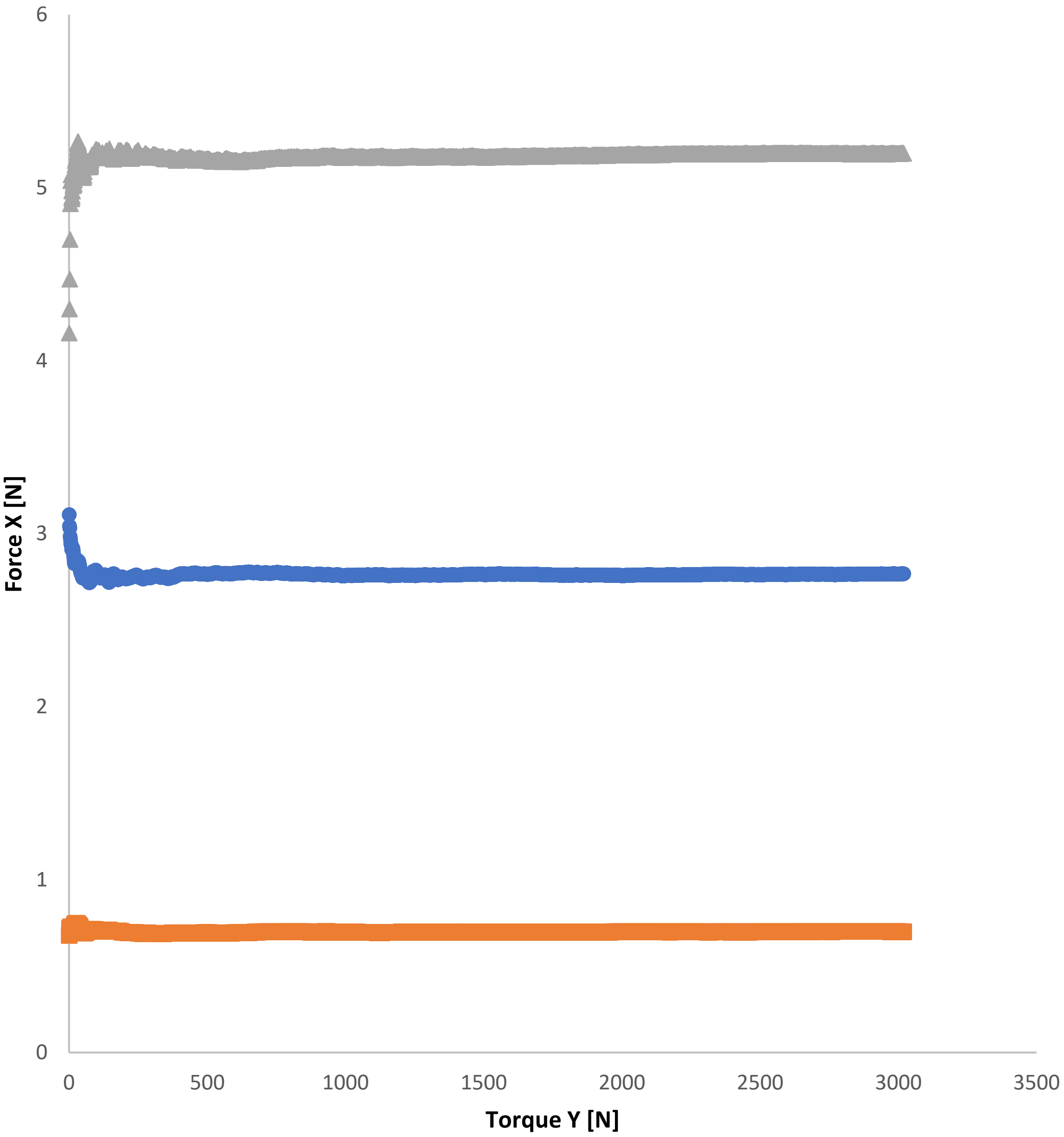

Figure 116 - Moving average of force for the model at 200 degrees with wind at 3.1 m/s, at 6.6 m/s and at 9.4 m/s

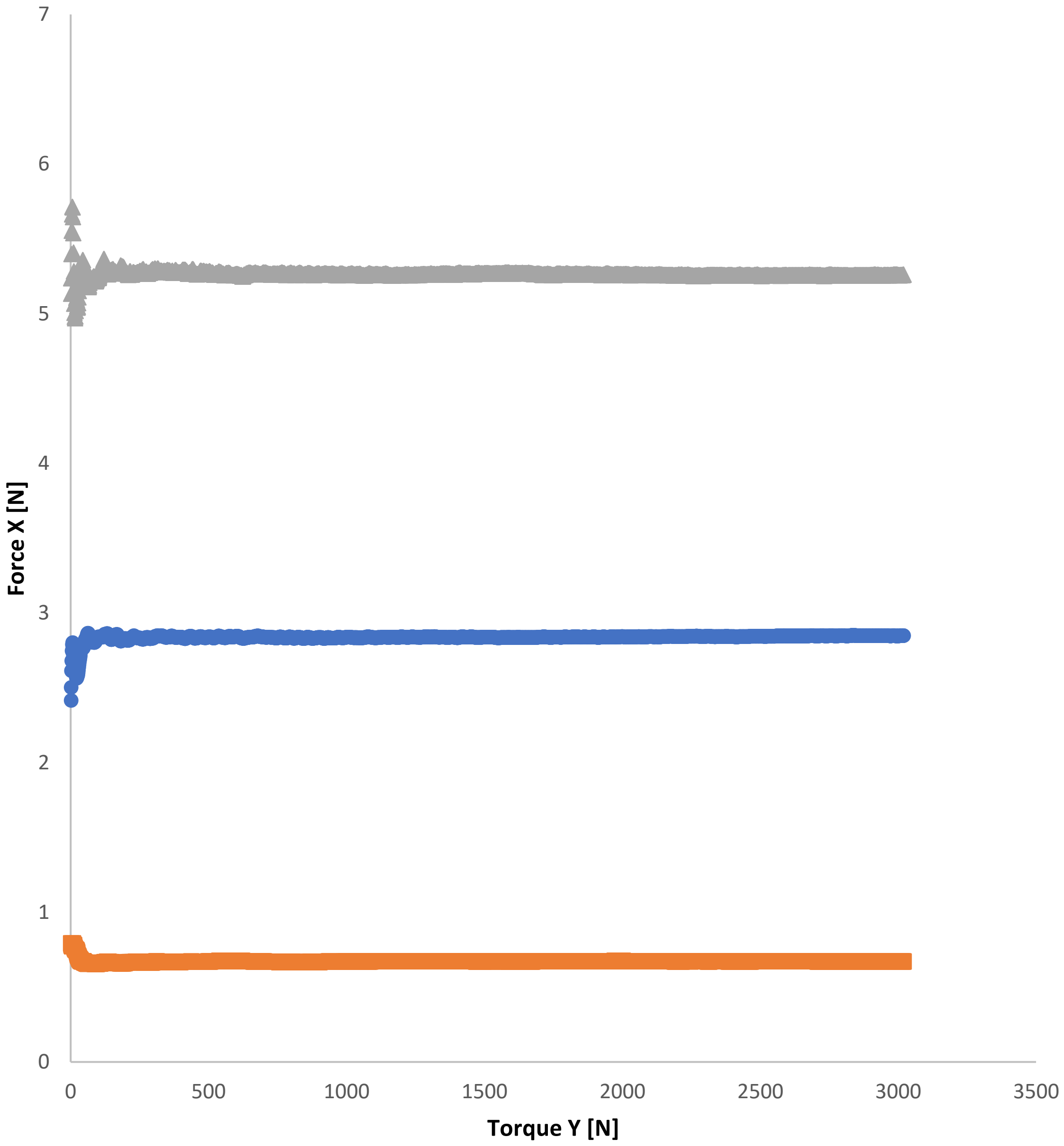

Figure 117 - Moving average of force for the model at 210 degrees with wind at 3.1 m/s, at 6.6 m/s and at 9.3 m/s

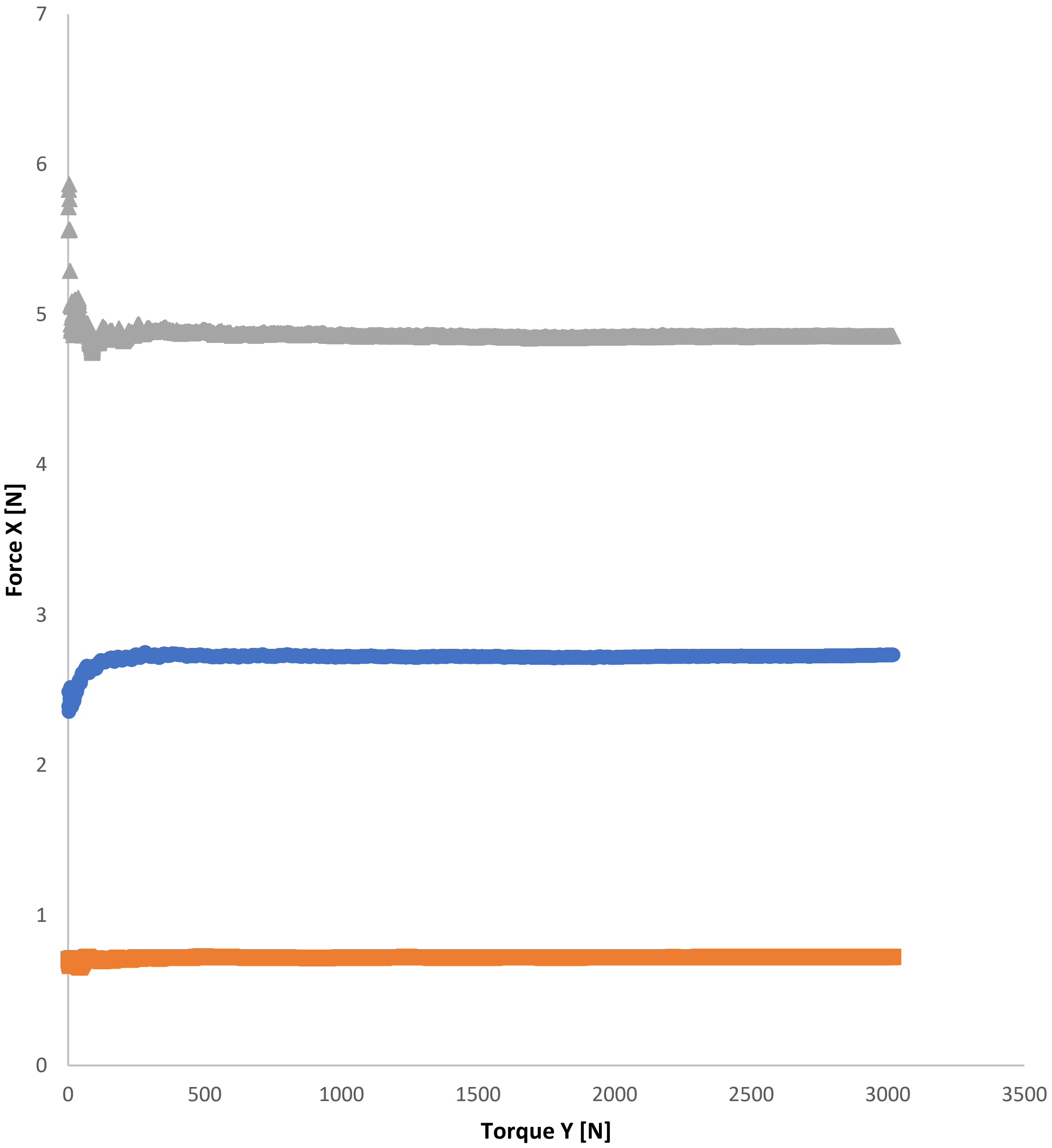

Figure 118 - Moving average of force for the model at 220 degrees with wind at 3.1 m/s, at 6.6 m/s and at 9.3 m/s

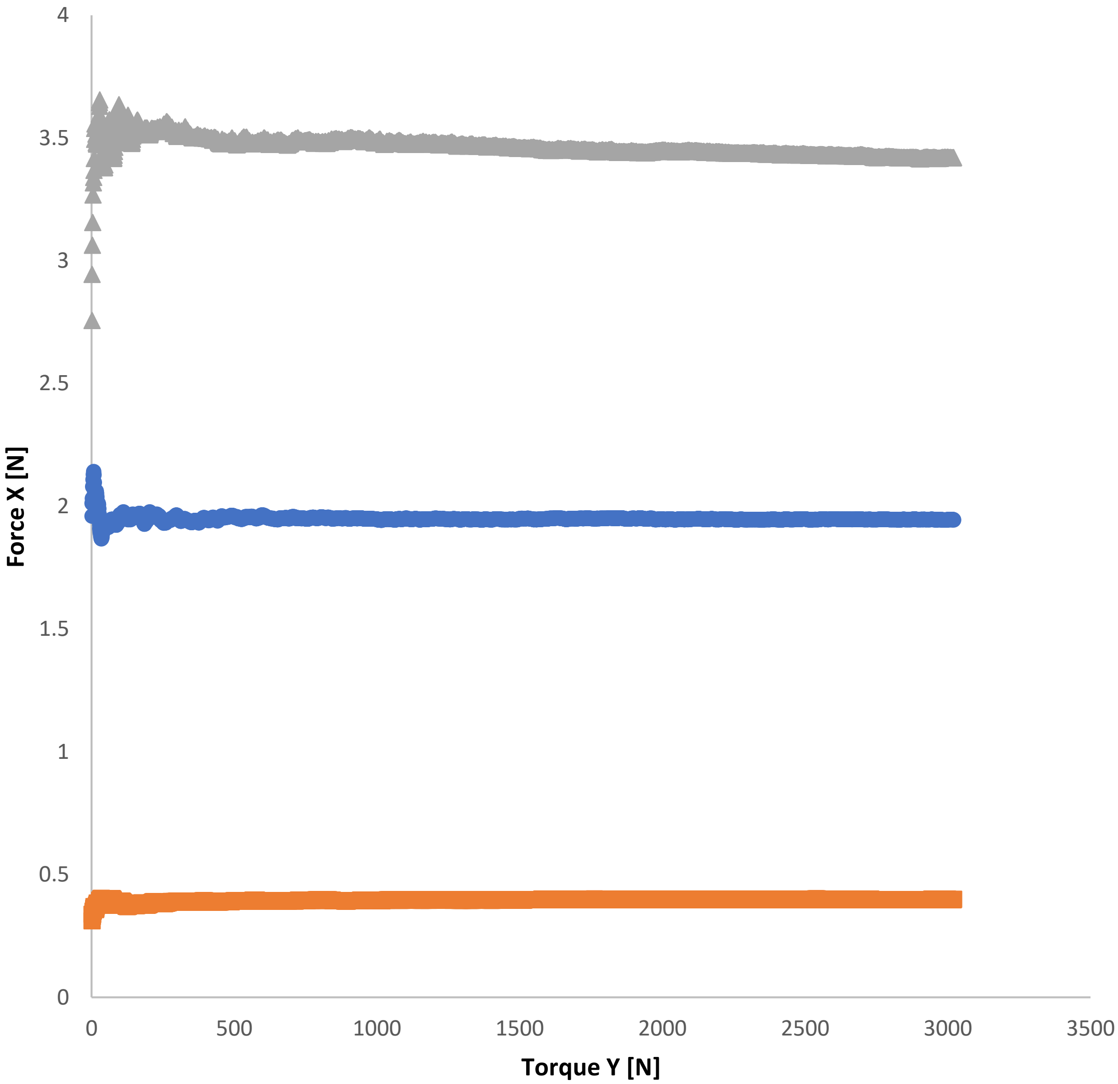

Figure 119 - Moving average of force for the model at 230 degrees with wind at 3.1 m/s, at 6.6 m/s and at 9.3 m/s

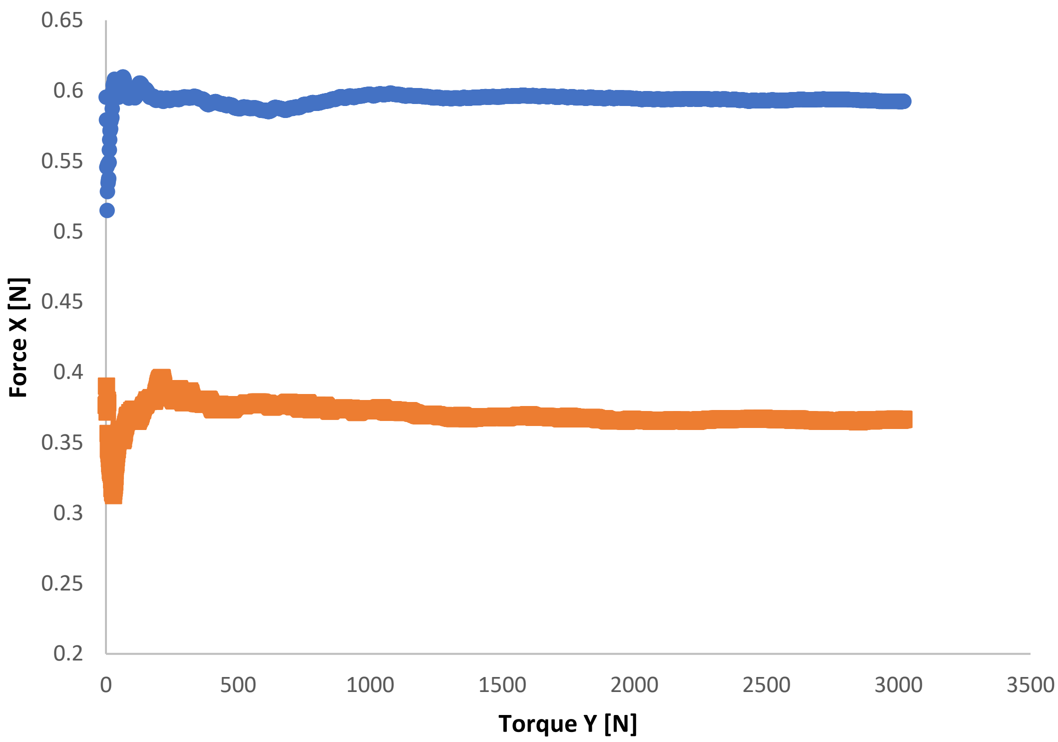

Figure 120 - Moving average of force for the model at 240 degrees with wind at 3.1 m/s, at 6.6 m/s and at 9.3 m/s

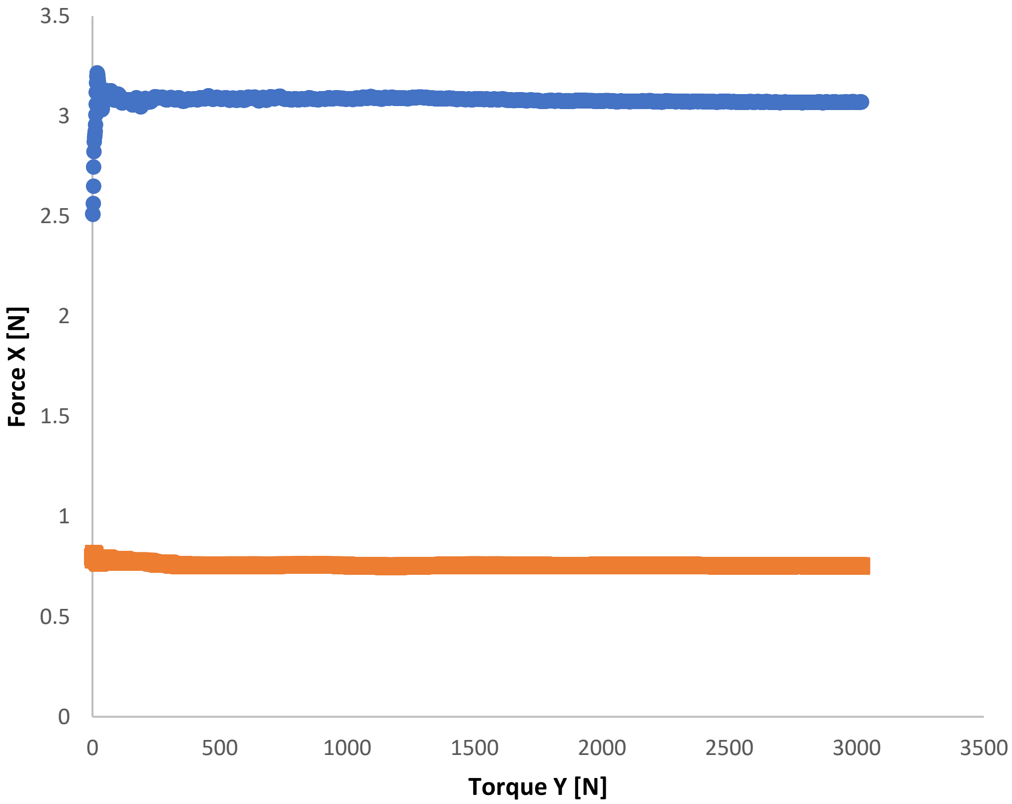

Figure 121 - Moving average of force for the model at 340 degrees with wind at 3.1 m/s, at 6.6 m/s and at 9.3 m/s

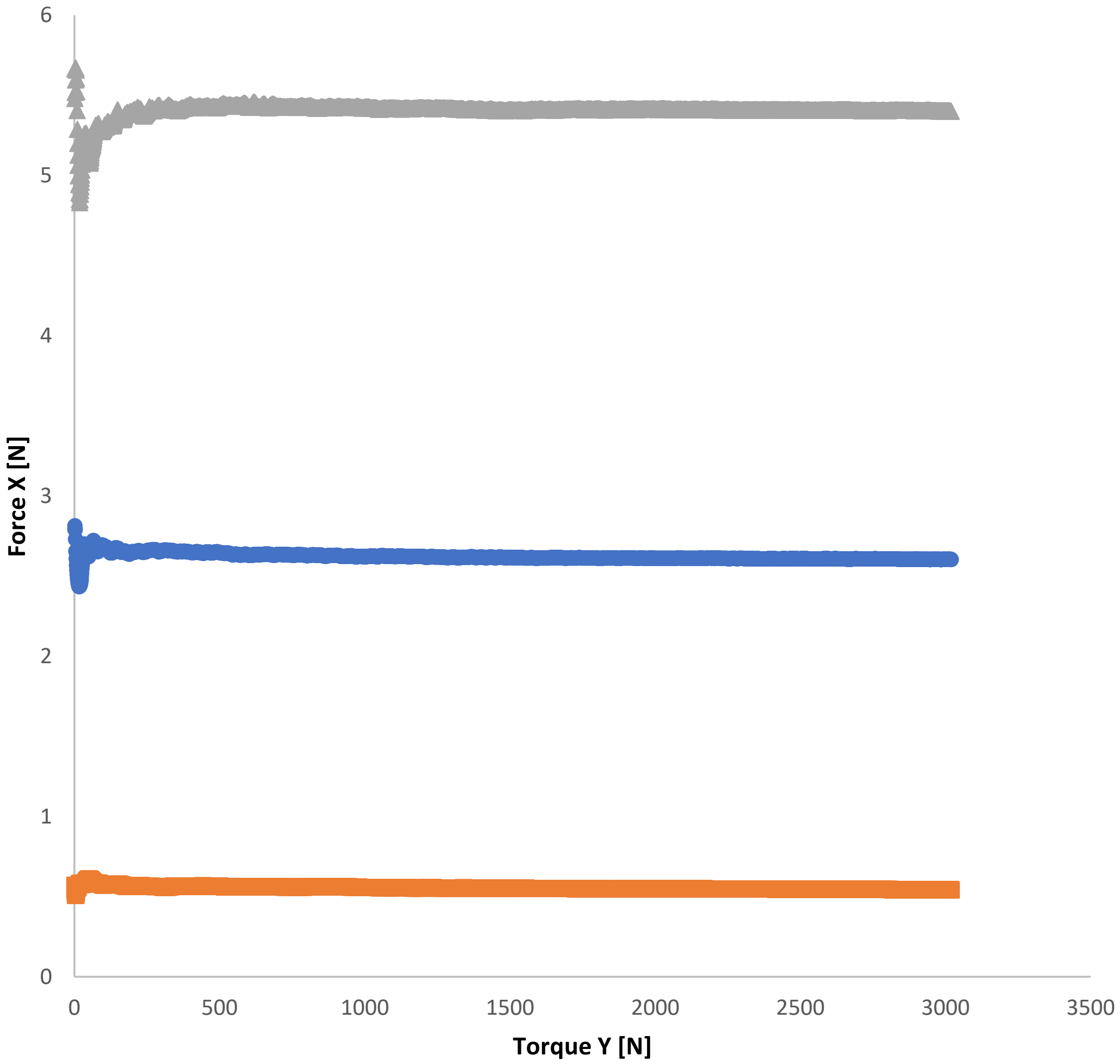

Figure 122 - Moving average of force for the model at 350 degrees with wind at 3.1 m/s, at 6.6 m/s and at 9.3 m/s

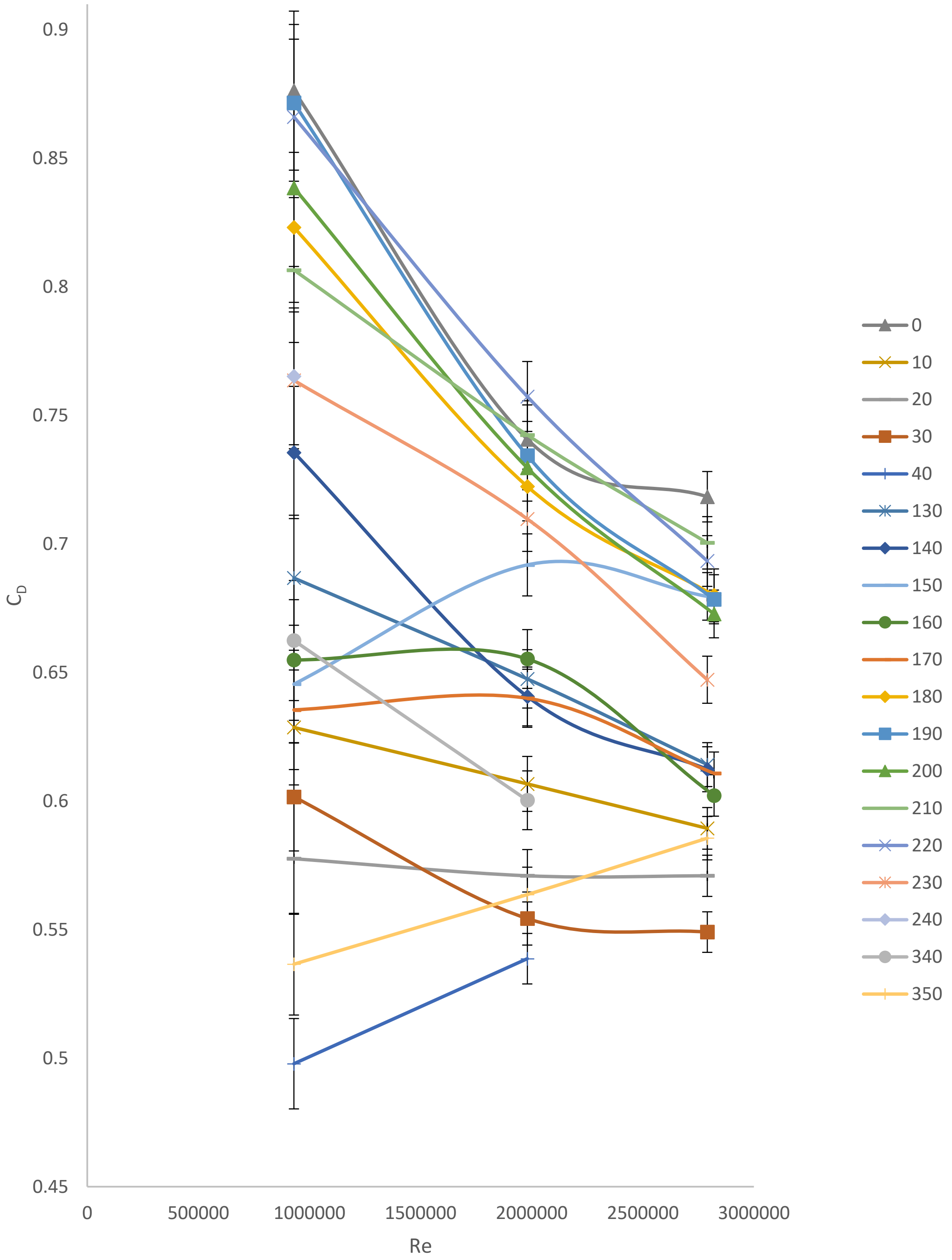

Figure 123 - C_D in function of the speed of the wind for the model in configuration 1, for different angle ϑ (legend) and its uncertainties